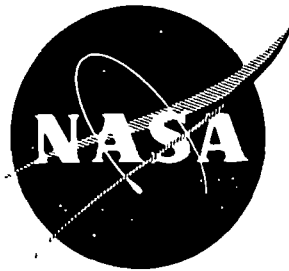


NASA CR-135124
PWA-5448



**CIRCUMFERENTIAL DISTORTION MODELING
OF THE TF30-P-3 COMPRESSION SYSTEM**

by R. S. Mazzawy and G. A. Banks

United Technologies Corporation
Pratt & Whitney Aircraft Group
Commercial Products Corporation
East Hartford, Connecticut 06108

January 1977

prepared for

NATIONAL AERONAUTICS AND SPACE ADMINISTRATION

NASA Lewis Research Center
Contract NAS3-18535

1 Report No NASA CR-18535	2 Government Accession No	3 Recipient's Catalog No	
4 Title and Subtitle CIRCUMFERENTIAL DISTORTION MODELING OF THE TF30-P-3 COMPRESSION SYSTEM		5 Report Date	
		6 Performing Organization Code	
7 Author(s) R S Mazzawy G A Banks		8 Performing Organization Report No PWA-5448	
		10 Work Unit No	
9 Performing Organization Name and Address UNITED TECHNOLOGIES CORPORATION Pratt & Whitney Aircraft Group Commercial Products Division East Hartford, Connecticut 06108		11 Contract or Grant No NAS3-18535	
		13 Type of Report and Period Covered Contractor Report	
12 Sponsoring Agency Name and Address National Aeronautics and Space Administration Washington, D C 20546		14 Sponsoring Agency Code	
15 Supplementary Notes Project Manager, David G Evans, Engine Research Branch, Air-Breathing Engine Division, NASA-Lewis Research Center, Cleveland, Ohio			
16 Abstract Circumferential inlet pressure and temperature distortion testing of the TF30 P-3 turbofan engine was conducted at NASA-Lewis Research Center Pratt & Whitney Aircraft has modelled the compressor system at the test conditions run using its multiple segment parallel compressor model Various aspects of engine operation and distortion configuration were modelled These include the effects of compressor bleeds, relative pressure-temperature distortion alignment and circumferential distortion extent Model predictions for limiting distortion amplitudes and flow distributions within the compression system were compared with test results in order to evaluate predicted trends Relatively good agreement was obtained The model also identified the low pressure compressor as the stall-initiating component, which was in agreement with the data.			
17 Key Words (Suggested by Author(s)) Turbofan Inlet Flow Distortion Compressor Stall Compressor Modeling		18 Distribution Statement Unclassified - Unlimited	
19 Security Classif (of this report) Unclassified	20 Security Classif (of this page) Unclassified	21 No of Pages	22 Price*

* For sale by the National Technical Information Service Springfield, Virginia 22151

PAGE MISSING FROM AVAILABLE VERSION

FOREWORD

This report was prepared for the National Aeronautics and Space Administration, Lewis Research Center, under Contract NAS3-18535 to present the results of the analysis of circumferential inlet distortion data for the TF30-P-3 afterburning turbofan engine. Mr. D. G. Evans was the NASA Project Manager for this effort, assisted by Dr. A. Kurkov and Mr. W. M. Braithwaite, and Mr. R. S. Mazzawy was the P&WA Program Manager. This report was prepared by R. S. Mazzawy and G. A. Banks, with assistance from R. J. Heckman and other P&WA contributors.

TABLE OF CONTENTS

	Page
FOREWORD	iii
SUMMARY	1
INTRODUCTION	3
NASA LERC ENGINE DATA	4
P&WA MULTIPLE SEGMENT MODEL	4
Non-Steady Rotor Loss	4
Critical Inlet Distortion Level	6
Blade Row Performance Characteristics	7
Model Accuracy	8
DATA ANALYSIS	9
180° Circumferential Pressure Distortion	9
Circumferential Distortion Extent	12
180° Circumferential Temperature Distortion	13
Combined Pressure and Temperature Distortion	14
Influence of Relative Distortion Orientation	15
Influence of Compressor Bleeds	16
Stall Sites	18
CONCLUSIONS AND RECOMMENDATIONS	18
SYMBOLS	20
REFERENCES	21
APPENDIX A - Performance Maps	79

SUMMARY

This report documents the results of modeling the TF30-P-3 compression system operating with circumferential inlet pressure and temperature distortions with the P&WA developed multiple-segment parallel compressor model. The model predictions of limiting distortion amplitudes and flow distributions within the compression system are compared with the experimental results obtained from distortion testing the engine at the NASA-Lewis Research Center. Included are the various 180° extent pressure and temperature distortions run separately and in several combinations of alignment, reduced extents of pressure distortion, and various combinations of the compressor bleed system activated. In addition, several hypothetical inlet distortions were modeled to investigate trends and to provide further insight into the distortion tolerance of the TF30-P-3 engine.

The multiple segment parallel compressor model provides a detailed blade row by blade row description of the distorted flow field for the TF30-P-3 compression system. The required pressure and temperature rise characteristics for each blade row were derived from P&WA compressor rig testing, and have been verified by a previous comparison with NASA uniform inlet engine test data for a low rotor speed range of 7300 to 8700 RPM (approx 76 to 90% of design). The engine operating conditions over this range of low rotor speeds were determined from a previous analysis of NASA engine data.

The relative influence of the different features of the model describing the distorted flow field phenomena were explored in some detail. It was determined that circumferential cross-flow and unsteady rotor loss effects were the principle modifiers of the classic parallel compressor concept. The predicted effects of circumferential extents of inlet pressure distortion of less than 180° were verified with P&WA and NASA engine data. The influence of compressor overboard bleed was also predicted and verified with limited P&WA data.

The P&WA model predictions agreed reasonably well with the experimentally observed trends. Small differences for individual points were attributable to uncertainty in engine operating condition, and extrapolation of blade row performance characteristics. The low pressure compressor was predicted to be the component which initialized the stalls, which was in agreement with the data.

PAGE MISSING FROM AVAILABLE VERSION

INTRODUCTION

NASA Lewis Research Center (NASA LeRC) testing of the P&WA TF30-P-3 afterburning turbofan engine has provided measurements of the circumferential distortion attenuation and tolerance of the compressor system. Pratt & Whitney Aircraft has modeled these data at the conditions tested using its multiple segment parallel compressor model and its extensive background of information on this engine. The model predictions are compared to the experimental results. P&WA has also predicted the response to various extents and combinations of inlet circumferential pressure and temperature distortion for which little or no data exists.

The initial effort under this contract has been reported in reference 1 which provides details of the testing procedure and describes the multiple segment distortion model. It also detailed the results of modeling 180° pressure distortion attenuation data using the multiple segment model, the limiting distortion levels predicted by the classic parallel compressor theory, the stalling criteria used, and comparisons of the model predicted results with the data.

In this report the distortion tolerance to 180° pressure distortion has been predicted and compared with data at four low rotor speeds (7300, 7800, 8200 and 8700 RPM) using an expanded multiple segment model which includes unsteady rotor losses. Additional calculations were done at 8200 RPM to demonstrate the relative influence of the individual distorted flow field phenomena accounted for in the model. These flow phenomena include 1) inertial effects, 2) fluid particle circumferential displacement, 3) inlet flow angle variation, 4) circumferential crossflow, and 5) unsteady rotor losses. Additionally, the effect of bleeding air from the low pressure and/or high pressure compressor on distortion tolerance were predicted at 8200 RPM.

The extent of the distortion was varied to include 60° and 120° defects in inlet total pressure. Sensitivity calculations were compared with data at 7400 and 8200 RPM for the 120° distortion. The 60° distortion calculation was performed for a rotor speed of 8200 RPM. No NASA LeRC data were available to check this latter calculation, but a general trend was established for circumferential distortion extent.

Circumferential temperature distortion was modeled at 7680 and 7740 RPM. At 7740 RPM a distortion level less than critical was used to evaluate distortion attenuation and compare it with limited data. At 7680 RPM the critical distortion intensity was predicted and compared with NASA LeRC data. Critical levels of pressure distortion in combination with temperature distortion were also evaluated and compared with data at 7800 RPM with two relative alignments differing by 180° . A general evaluation of combined pressure and temperature distortion sensitivity was performed at 8600 RPM for a series of alignments each differing by 90° . These results provide an insight into the manner in which pressure and temperature distortions interact to affect engine stability.

Detailed performance maps for each component of the compression system are shown in Appendix A. These maps show the average operating condition of each component used for the model predictions of distortion sensitivity.

The work reported herein was done using the U. S. Customary system of units. The information in this report is provided in those units as well as the International System of Units (SI).

NASA LeRC ENGINE DATA

The Pratt & Whitney Aircraft TF30-P-3 turbofan engine was tested with circumferential distortion in an altitude test chamber at an inlet Reynolds Index of 0.5. An engine cross-section with the instrumentation station locations is shown in Figure 1. Two engine builds were run. Engine Build A (ref. 2) were tested with 180° and 120° circumferential pressure distortion. Engine Build B was tested with 180° circumferential temperature distortion (ref. 3) using a gaseous hydrogen fueled burner upstream of the engine to produce the temperature distortions. Build B was also tested with 180° combined temperature and pressure distortion. The pressure and combined pressure and temperature distortions were generated using the NASA-developed air-jet device (ref. 4). The combined pressure and temperature distortions were generated by using primary air temperatures to the engine that were above or below the temperature of the air supplied to the air jet.

With the exception of one 180° temperature distortion case, all distortions were at the critical level required to stall the engine. For the less than critical temperature distortion, data were recorded with steady state instrumentation and engine bleeds closed. For the critical distortion cases, the distortion amplitude was increased at constant low rotor speed until an engine stall was recorded using high response instrumentation. The engine was then decelerated with the distortion generating device held in its pre-surge position. The high pressure compressor 12th stage overboard bleeds were then held open and the engine was accelerated back to the original low rotor speed. Steady state data were then recorded to document the distortion level, distortion attenuation within the compression system, and engine operating condition.

P&WA MULTIPLE SEGMENT MODEL

The distortion modeling was done using an expanded form of Pratt & Whitney Aircraft's multiple segment parallel compressor model used in Ref. 1. The model, described in reference 1 Appendix, incorporates the options of simple parallel compressor theory, fluid inertial acceleration, fluid particle swirl, inlet flow angle variation, and circumferential cross flow through cavities shown in Figure 2. It provides an individual blade row by blade row description of the TF30-P-3 compression system. Two additional features of the model not included in Ref. 1 or previously exercised in the TF30 analysis, concern the addition of rotor blade losses in a non-steady flow field and the method of determining critical distortion amplitude. They are described as follows.

Non-Steady Rotor Loss

Incorporation of this feature into the multiple segment model is simply recognizing the fact that rotor blade boundary layers do not separate or re-attach instantaneously as they move into or out of a circumferential flow distortion. A finite time, consistent with fluid velocity, is required as is evident from Figure 3. This figure shows rotor blade losses measured on a single stage low speed P&WA compressor rig using high response instrumentation. The measurements were made both with a steady uniform inlet and a 180° circumferential distortion screen. The uniform inlet data was obtained by measuring the rotor blade wakes at different values of rotor inlet angle. The air angle was reduced (incidence angle increased) by throttling the compressor discharge until the compressor stalled. The circumferential distortion data

was obtained at one throttle position by measuring the inlet air angles and rotor blade wakes at different positions around the circumference. In this way, one full cycle of rotor blade loss for a single revolution was obtained. Starting at a high inlet air angle (away from the distortion screen) the rotor moves behind the screen (in direction of arrows) and inlet air angle is reduced. The measured blade loss, however, lags behind the uniform inlet data. Before emerging from behind the screen, the rotor blade experiences air angles lower than the values at the uniform inlet stall point, but does not stall. The rotor finally emerges from behind the screen, again lagging behind the uniform inlet loss until the cycle has been completed.

This experimental evidence makes it clear that a time unsteady flow analysis which relies on the quasi-steady blade row performance is necessarily limited in the accuracy of its results. The complexity of the non-steady separation process is not amenable to purely analytical treatment. Consequently, it is necessary to correlate the non-steady loss and turning through a combined experimental/analytical procedure.

On the basis of the experimental observations of the boundary layer separation process, a simple model (ref. 5) was proposed which related the non-steady blade loss to quasi-steady blade loss in the following manner:

$$\frac{d \text{ Loss}}{dt} = \frac{1}{\tau} (\text{Loss } Q \text{ S} - \text{Loss}) \quad (1)$$

This relation, stated simply, says that the rate at which loss changes with time is governed by how much it lags the quasi-steady counterpart (for the same value of inlet air angle). The term τ is an empirical time constant which is to be evaluated on the basis of blade row cascade geometry and pertinent flow variables. The experimental evidence suggests that

$$\tau = K (b/U) \quad (2)$$

The application of this model to the data using a proportionality constant ($K = 1.0$) yields a reasonably good approximation as shown in Figure 3. In addition, a number of compressor configurations were investigated with the multiple segment model to evaluate the general validity of this calculation (ref. 6). It was determined that the proportionality constant of unity repeatedly gave good agreement with test data for a wide range of compressor blade designs. Consequently this value has been used in the TF30-P-3 distortion analysis.

A significant point to note from Figure 3 is that the blade loss does reach the quasi-steady loss curve (or an extension of it) before the rotor leaves the low flow (low air angle) region. The loss level is above that which can be associated with a stall instability with uniform inlet flow. Since the blade experiences high losses over only a portion of its circumferential path, it apparently can sustain stable flow at this high loss condition. Eventually the loss level becomes excessive (e.g. for a higher inlet distortion) or, alternately the circumferential extent of the region which exceeds the uniform stall loss level increases, and the compressor becomes unstable.

If either of these above conditions occurs, the relative loss in stall margin will depend in part on the average compressor mass flow rate. The mass flow rate in each segment depends upon the boundary conditions and segment performance as discussed in the following section. If blade losses are low in a particular segment, the boundary conditions can be satisfied at a higher mass flow rate than if the blade losses are high. The time required for stall or separation to occur is dependent (Equation 1) on flow velocity. Initially, this velocity is high, Figure 3, while the flow velocity at the start of unstalling or reattachment is low. Hence, it is to be expected that the separation period during which losses are farthest below normal levels will be shorter than the reattachment period with the largest higher-than-normal losses. This will bias a greater extent of the circumference toward lower flow. Furthermore, the non-linearity of the quasi-steady blade loss curve, Figure 3, results in a greater departure from the uniform inlet loss level during the reattachment process. Consequently, the unsteady rotor loss enables the engine to run at a lower average mass flow rate at a given distorted stall condition. More importantly, in terms of engine operation at a given average mass flow rate (e.g. on the normal operating line), the unsteady rotor loss effect enables the engine to operate with a higher inlet distortion level before stall than if this effect were not included.

Critical Inlet Distortion Level

In reference 1, predictions of critical distortion level were based upon classic parallel compressor theory. The stalling distortion was determined to be that which had the low velocity region coincident with the uniform inlet stall line. No attempt was made to use the multiple segment model since it was realized that the unsteady rotor loss effects were important for an accurate evaluation of near stall performance. With the improved modeling capability for unsteady rotor loss effects comes an improved stall criterion.

The procedure used was to determine the distortion level required to stall the NASA TF30-P-3 engine on its experimentally determined operating line. In order to do this the critical distortion amplitude was assumed and the model was run with increased levels of compressor exit static pressure up to the stall limit. This limit, simply stated, is a predicted maximum exit static pressure at which the compressor can operate at the given rotor speed and distortion level. The maximum exit static pressure is determined in the following manner. The inlet mass flow is distributed about the circumference to the various segments consistent with the segment performance and boundary conditions. In general, segments with high inlet total pressure (or low inlet total temperature) have high inlet mass flows while segments with low inlet total pressure (or high inlet temperature) have low mass flows. The crux of the problem is that, while there are normally only two levels of inlet total pressure (or temperature), there must be a continuous distribution of mass flow from the high to the low level. The higher the exit static pressure is for a given level of inlet distortion, the greater will be the difference between the high and the low mass flow level. At some point, the transition between the high and the low level cannot be made with a continuous distribution of mass flow. This is illustrated in Figure 4 for a distorted sector located circumferentially between 90 and 270 degrees.

The exit static pressure for the discontinuous solution in this figure is only 0.1% higher than the continuous solution. The stall point performance is calculated to be the numerical average of the pressure ratio and mass flow of the individual segments for the continuous solution.

The average total pressure ratio and airflow rate at the peak exit static pressure point were then compared to the experimentally determined operating line values for each compressor component. If the operating point was above or below the operating line, the distortion amplitude was increased or decreased, respectively, until the predicted operating point at stall coincided with the NASA operating line.

An example of this procedure is illustrated in Figure 5. The average compressor performance at 8200 RPM is shown for two levels of inlet total pressure distortion. For a distortion amplitude $(P_{TMAX}-P_{TMIN})/P_{TAVG}$ of 0.13, the peak exit pressure point is above the NASA operating line. When the distortion amplitude is raised to 0.16, however, the peak pressure point is nearly coincident with the operating line. Hence 0.16 would be the predicted critical distortion amplitude. Note that the low pressure compressor performance map is shown in this figure. In all cases the low pressure compressor was found to initiate stall in the TF30-P-3. Since this result was suspected from previous work (ref. 1), the inlet distortion amplitude required to stall the low pressure compressor (station 2.0 to 3.0) on the NASA operating line was determined first. This same distortion amplitude was then input into the fan (station 2.0 to 2.6F). The pressure and temperature distortion exiting the low pressure compressor at this condition was also input into the high pressure compressor (station 3.0 to 4.). For each component, the exit static pressure (station 3.0, 2.6F and 4.0) were assumed to be uniform. This assumption was consistent with NASA test data as well as data from numerous TF30 engine distortion tests conducted by P&WA.

At the LPC critical distortion level the fan was on its operating line and exhibited an exit static pressure below its maximum exit static pressure. Similarly, the pressure distortions exiting the low pressure compressor were insufficient to "stall" the high pressure compressor. Furthermore, high response pressure measurements made by NASA LeRC verified the low pressure compressor as the initiator of the stall event for all cases but one. In this instance, the number of operational high response pressure transducers was inadequate for isolating the location of the stall. It is unlikely, however, that stall was initiated anywhere but in the low pressure compressor.

In the above predictions, it was necessary to introduce a Reynolds number correction to the model predictions because the predictions were based on blade row performance characteristics obtained at a Reynolds number index of 1.0 whereas a value of 0.5 was used during the NASA LeRC tests. A history of independent engine measurements of pressure distortion sensitivity made by P&WA (ref. 1) and NASA Lewis (ref. 3) at different Reynolds numbers provided the correction necessary to adjust the predicted critical distortion amplitudes to the NASA Reynolds number index before making a comparison with data.

Blade Row Performance Characteristics

In the previous section, the calculated exit static pressure was determined primarily from the blade row performance characteristics on the basis of local flow velocity, and secondarily, from non-steady flow effects on the basis of local flow velocity gradients and rotational speed. At the predicted stall conditions, it was found that the minimum local flow velocity is significantly lower than the flow velocity at stall with a uniform inlet because non-steady flow effects in the rotor allow the compressor to operate at local flow rates below the uniform

inlet stall point. Because the blade performance characteristics were derived from uniform test results, they were necessarily extrapolated below the data range for this application. Correlations based on extensive P&WA two-dimensional cascade testing were used to make these extrapolations. Further, the predicted distorted mass flow at stall is sensitive to the extrapolations because the curve of overall pressure ratio with flow rate has a shallow slope in the extrapolated region, as shown in Figure 5. Therefore, the absolute maximum exit static pressure is subject to this extrapolation.

Model Accuracy

The accuracy of the critical distortion amplitude prediction is dependent on how well the model describes the various phenomena associated with the distorted flow field. Other significant sources of error include the model tolerances for determining the maximum exit static pressure, errors in the determination of the engine operating conditions, and extrapolations of the blade row performance characteristics. Model tolerances have been set to assure that predicted critical distortion levels are known to within 0.1 on a max-min/avg basis for either pressure or temperature distortion.

In order to minimize errors associated with engine match point, a set of engine operating parameter relations were utilized which were functions of low rotor corrected speed. These relations were derived from a detailed analysis of 180° pressure distortion stall point data. The variables of primary importance were total corrected airflow, bypass ratio, and high rotor corrected speed. These parameters are shown in Figures 6 through 8, respectively, as functions of low rotor corrected speed. Although they were derived for NASA LeRC engine Build A, the same relations have been applied to engine Build B. Separate measurements made by NASA have shown that total airflow was within 1%, and the ratio between high and low rotor speed was the same for the two engine builds. Bypass ratio, however, is a calculated rather than a measured parameter. No comparison in the calculated values between the two engine builds was possible due to an error in the station 7 probes during Build B testing.

DATA ANALYSIS

180° Circumferential Pressure Distortion

As reported in reference 1, the classic (two segment) parallel compressor calculation predicted a critical distortion level which was .02 to .04 lower (on a max-min/avg basis) than the measured data. The multiple segment model predictions made in the present work use the same data at low rotor corrected speeds of 7300, 7900, 8200 and 8700 RPM. A comparison of the present results with the data is shown on Figure 9. Very good agreement has been obtained at the lowest rotor speed with progressively increasing differences at higher speeds. These differences were attributed to uncertainty in the engine match and to the extrapolations of the blade row performance characteristics noted previously. The predicted distorted stall airflow is sensitive to the extrapolations because the overall pressure ratio vs. flow rate curve has a shallow slope in the extrapolated region. This is to be expected because the absolute maximum exit static pressure for the limiting solution corresponds to a zero slope condition. Consequently, a small error in the extrapolation for pressure rise can result in a significant error in mass flow at stall. No attempt was made to alter the extrapolations to improve stall point predictions when differences were found between the model and data. Such an attempt was precluded by the large number of blade rows in the TF30 compression system and the realization that "arbitrary" changes to extrapolations provided no firm basis for accurate modeling of the distortion problem. It was therefore assumed that any error in the extrapolations based upon cascade data were systematic in nature. The model predictions could thus be evaluated on the basis of the points which could be checked with NASA leRC data.

The distorted flow field phenomena (model options) mentioned previously account for the differences between the classic 2 segment parallel compressor, which is based only on uniform flow performance in each segment, and the multiple segment parallel compressor predictions. It is of interest to understand the relative contribution that each of these phenomena have toward these differences. Towards this end the multiple segment model was exercised for a 180° pressure distortion by incorporating the various options in the following succession:

- Case 1) Parallel Compressor (Using 36 segments for comparison purposes)
- Case 2) Case 1 Plus Inertial Acceleration
- Case 3) Case 2 Plus Fluid Particle Swirl
- Case 4) Case 3 Plus Inlet Flow Angle Variation
- Case 5) Case 4 Plus Circumferential Cross Flow
- Case 6) Case 5 Plus Unsteady Rotor Loss

These calculations were performed for a corrected low rotor speed of 8200 RPM using the stalling distortion level measured by NASA LeRC. Since the predicted critical level of distortion was lower than the level measured by NASA for a number of these cases, it was necessary to relax the constraint of the NASA operating line. A lower operating line was used so that a comparison could be made with the only variable being the model calculation option. The results of these calculations for the circumferential variation in inlet corrected airflow, static and total pressures, and total temperature at the NASA measurement locations are shown in Figure 10. The distorted sector was located circumferential between 90° and 270° on the figure. The effect of each option is noted as follows:

Parallel Compressor (Case 1)

The parallel compressor essentially sets two levels of mass flow, Figure 10a, consistent with compressor boundary conditions and quasi-steady compressor performance. It is the dominant factor in determining levels of pressure distortion attenuation and resultant temperature distortion amplitude, Figures 10e to 10bb.

Inertial Acceleration (Case 2)

Near the edges of the distortion the fluid in the rotors experience significant accelerations consistent with non-steady inertial forces. The pressure and temperature changes due to these forces alter the compressor performance and change the circumferential mass flow distribution from that dictated by parallel compressor theory (Figure 10a). For the TF30, however, the quasi-steady performance dominates, and only minor changes occur in attenuation. The mass flow distribution is affected primarily as a more gradual transition between the two levels set by parallel compressor.

Fluid Particle Swirl (Case 3)

The dominant influence of particle swirl is to cause a "rotation" of the temperature distortion relative to the pressure distortion. This starts in the form of "spikes" near the edges of the distortion region (Figures 19g and 10m) near the front of the engine. This is due to the inlet differences in fluid particle entropy level at the edges. In the front of the engine there is very little "parallel compressor" temperature distortion due to total pressure distortion attenuation. As the air progresses through the compressor, a combination of the circumferential movement of the "spike" region and an increase in the "parallel compressor" distortion is evident (Figures 10s, 10v, and 10y). In the rear stages the "spike" has a smaller effect relative to the "parallel compressor" so that at the exit plane (Figure 10bb), it is barely noticeable. Since the temperature distortion is altered by particle swirl there is a change in the front to rear stage match which dramatically alters the mass flow distribution (Figure 10a). The overall total pressure attenuation, (Figure 10z), however, is still primarily set by parallel compressor.

Inlet Flow Angle Variation (Case 4)

The non-uniform inlet static pressure (Figure 10c) which the compression system imposes on the flow, causes the inlet flow angle to vary in front of the inlet guide vane. The inlet guide vane, however, is assumed to re-align the flow into the first rotor. Consequently, there is no significant effect on flow distribution or distortion attenuation (Figures 10a, 10z).

Circumferential Cross Flow (Case 5)

Flow redistribution within the fan and compressor (through cavities shown in Figure 2) changes the front to rear stage match and has a pronounced effect on the inlet mass flow distribution (Figure 10a). The mass flow variation from maximum to minimum is increased which results in more attenuation in the front stages of the compressor. Additionally, the lower minimum mass flow is indicative of operation with reduced stall margin for the imposed distortion.

Unsteady Rotor Loss (Case 6)

Recognition of the fact that blade boundary layers do not separate or re-attach instantaneously alters blade row performance, particularly in regions where blade loss is increasing rapidly with incidence. The effect on blade row performance changes the inlet mass flow variation required to meet boundary conditions (Figure 10a). The differences between Case 5 and Case 6 are relatively small because of the lower operating line used for this series of calculations.

In order to better demonstrate the influence of unsteady rotor loss on compressor stability, additional calculations were made to predict critical distortion amplitude on the NASA operating line. This was done in two steps. The model was first run with all distorted flow effects except the non-steady rotor loss (comparable to Case 5). The second step included the non-steady rotor loss (comparable to Case 6). Critical distortion levels were predicted at several rotor speeds and compared with simple 2-segment classic parallel compressor predictions from Reference 1 and NASA LeRC data in Figure 11. It should be noted that the parallel compressor prediction at 8600 RPM is high due to a problem with the data used in Reference 1. The data used at that rotor speed were recorded with the distortion located 180° out of phase with the distortion position used at 7400, 7800 and 8200 RPM. This resulted in an error in calculated bypass ratio. This problem was corrected for the present work by using new data at 8600 RPM supplied by NASA LeRC with the same relative distortion position as the other data. The predictions were corrected to the same RNI as the data as noted previously. Circumferential crossflows are primarily responsible for the change between the classic parallel compressor prediction and the multiple segment model prediction from the first step. A significant proportion of the crossflow occurs behind the front and middle stages of the low pressure compressor. Consequently, these stages experience a larger circumferential variation in incidence and blade loading, and are predicted to be much more sensitive to distortion. The non-steady rotor loss effect, however, more than compensates for the crossflows and the final prediction is an increased tolerance relative to classic parallel compressor which, at the lower speeds investigated, is closer to the actual test results.

From Figure 11 it can be noted that the model results without unsteady rotor loss are approximately at a fixed increment below the NASA test data. The effect of unsteady rotor loss was apparently stronger at increased rotor speed. This latter observation was somewhat unexpected because the governing equations for unsteady rotor loss, equations 1 and 2, depend only upon rotor chord length, and the product of the fluid velocity relative to the rotor and the time period which the rotor experiences the distortion (related to the inverse of rotor wheel speed). The first parameter is invariant and the second is nearly constant over the investigated range of rotor speed. Consequently, the details of the model results were explored at 8200 RPM, as shown in Figure 12.

This figure depicts the inlet mass flow distribution for three separate stall point calculations. multiple segment model, multiple segment model without unsteady rotor losses, and classic parallel compressor theory. The very low minimum airflow for the multiple segment model relative to the other two calculations demonstrates the requirement for extrapolating compressor performance, as stated earlier, to flow rates below the uniform flow stall limit. More significant is the fact that the average flow rate is also considerably lower for the multiple segment model calculation (38.4 Kg/sec, 83.5 lbs/sec vs 39.4 Kg/sec, 86.8 lbs/sec for the case without unsteady rotor loss and 39.2 Kg/sec, 86.4 lbs/sec for the classic parallel compressor). This implies that the engine match will change because the reduced low pressure compressor average pumping capacity will raise bypass ratio

This change in bypass ratio is evident from a comparison between NASA engine data with a uniform inlet and with a 180° pressure distortion of sufficient amplitude to stall the engine shown in Figure 13. In this figure the uniform inlet data is shown as a solid line. The 180° data is shown as individual points to demonstrate data scatter. The line shown earlier in Figure 7, which was the basis for the model calculations, is a best fit of the individual 180° distortion data points. As seen in Figure 13, the effect is strongest at the higher rotor speeds which showed the largest discrepancy between model prediction and data. Furthermore, the TF30-P-3 low pressure compressor flow capacity is dependent upon engine bypass ratio as illustrated in Figure 14. This figure was derived from uniform inlet compressor rig testing at P&WA and also demonstrates increased effects at higher rotor speeds.

A review of the NASA engine 180° distortion data points used to determine bypass ratio for the model calculation was subsequently made to estimate the possible error range. Figure 15 shows the distorted engine bypass ratio vs speed variation which corresponds to an uncertainty in engine core airflow of $\pm 1\%$. An uncertainty in core airflow of this magnitude would result in a variation in predicted critical distortion amplitude of ± 0.02 to ± 0.03 as shown on Figure 16. From Figure 16, it is evident that the uncertainty in the engine operating match with circumferential distortion is very significant to the model calculation. This fact, coupled with the increased bypass ratio effects on engine core flow capacity at higher speed, make it the most probable explanation of the prediction error. If this is true, then the parallel compressor calculation (ref. 1) would also be subject to the same uncertainty in engine operating conditions.

Circumferential Distortion Extent

The sensitivity of the TF30-P-3 engine to circumferential distortion extent was investigated at approximately 7400 and 8200 RPM low rotor speed. This included distortion extents of 60° and 120°. A limited amount of NASA LeRC data was available with 120° pressure distortion for comparison with the model predictions. These were supplemented by a P&WA distortion sensitivity correlation based upon a number of engine distortion tests. Engine match points for the different circumferential extents were assumed to be determined solely by low rotor speed and not influenced by the distortion extent. This assumption was made because the fixed instrumentation in the NASA LeRC engine was not sufficient to accurately calculate engine match point. For this reason, the same engine match shown in Figures 6, 7, and 8, which was derived from 180° distortion data, was also used for the other distortion extents.

Results of the model calculation are shown in comparison with NASA data and the P&WA K θ correlation at a corrected low rotor speed of 8200 RPM in Figure 17a. For a distortion extent of 180°, the NASA data and the correlation are in good agreement, while the model prediction for critical distortion amplitude is high by approximately 0.3. As distortion extent is reduced, the model predicts a trend which is less steep than the correlation. However, the model trend agrees well with the limited NASA data. The change between 180° and 120° is, in any case, quite small. The discrepancy between the model and the correlation at 60° may be due to an inadequacy in the correlation or the model. If the model is suspect, the discrepancy is most likely due to circumferential crossflow or unsteady rotor loss effects which have an increasingly greater effect on stability at lower extents of distortion. The crossflow tends to reduce the critical distortion level while the unsteady rotor blade loss increases it. Since both of these calculations are somewhat approximate, it is most likely a combination of errors in modeling both phenomena that causes the discrepancy. Another source of error is the possibility of a change in engine match with circumferential distortion extent which, as already mentioned, was assumed to be negligible because of a lack of definitive data. In any case the multiple segment model prediction is significantly better than classic parallel compressor which predicts the wrong trend with distortion extent.

Results at a low rotor corrected speed of 7400 RPM as shown in Figure 17b. At this lower rotor speed there again was very little difference between the critical 120 degree and 180 degree distortion amplitudes. The agreement between model and experiment is within the prediction accuracy set by model tolerances.

The increase in critical distortion amplitude at 60°, as mentioned, is attributable to unsteady rotor loss effects. In order to illustrate this, the engine inlet corrected airflow distribution has been plotted at 8200 RPM for three different distortion extents in Figure 18. The significant feature in this figure is the extent of the circumference over which the flow rate is lower than the uniform inlet stall flow (~ 37.5 Kg/sec, 83.0 lbs/sec) at this rotor speed. Although the pressure distortion extents differ by as much as 120° there is close agreement in the "less-than-stall" flow extent. In fact, this low flow extent is approximately 150° for each pressure distortion extent at its respective critical distortion amplitude. This implies that conditions must be favorable for stall over almost half of the circumference regardless of distortion extent. As the pressure distortion extent is reduced it is necessary to increase the distortion amplitude to achieve the required circumferential flow extent. When viewed from this perspective, it is understandable that the critical 120° pressure distortion (nearly 150°) amplitude is only slightly greater than the stalling 180° pressure distortion amplitude. Similarly, since the 60° pressure distortion extent is much less than 150°, the required distortion amplitude is significantly higher.

180° Circumferential Temperature Distortion

Engine sensitivity to circumferential inlet total temperature distortion was also investigated experimentally at NASA LeRC. As previously mentioned, these experiments were conducted using a different engine build (Build B) than that used for inlet pressure distortion testing (Build A). Engine operating conditions were assumed to be the same as engine Build A for the same low rotor speed. The temperature distortion amplitude was varied at a corrected low rotor speed of approximately 7700 RPM, and data were recorded at two levels: the critical level to induce stall and a lower level at approximately 75% of the critical level.

For the "less than critical" distortion case, the engine was operating with the interstage bleed systems closed and a distortion amplitude $(T_{MAX} - T_{MIN})/T_{AVG}$ of 0.11. The multiple segment model was run at these conditions, and the results of the calculated circumferential variation of temperature, total pressure and static pressure in the fan, low and high compressor are compared with data in Figures 19 (a-i). The distorted sector is located circumferentially between 90° and 270° on the figures. While there is only a minimum of data to compare, the model predictions are in good agreement with the distortion levels measured throughout the compression system. The predicted results in these figures are qualitatively the same as for an inlet total pressure distortion (reference 1). There is an attenuation of the total temperature distortion and the creation of a total pressure distortion due to the unequal work done by the distorted and undistorted sides of the compression system. The rotation of the distortion is governed by the same principles as pressure distortion (fluid and sonic velocity, rotor speed, and rotor chord) and is therefore identical at similar engine operating points.

The model prediction for critical distortion amplitude at 7700 RPM was 0.18. The measured amplitude was 0.15. At this point the relative accuracy of this prediction cannot be ascertained because of possible differences between the two engine builds and a difference in RNI between the measured and predicted examples used. However, this matter may be resolved by referring to the following series of data points taken with the two engine builds for which various amplitudes of pressure and/or temperature distortions were applied in order to precipitate an engine stall.

Combined Pressure and Temperature Distortion

In all cases 180° distortions were imposed on the engine. The low temperature and low pressure regions were either aligned or opposed. The data points are presented along with model predictions at the same rotor speeds in Figure 20. On this figure, aligned conditions (low pressure - low temperature) are defined as having positive amplitudes while opposed conditions have negative amplitudes. The corrected low rotor speeds are indicated for each data point and its corresponding model prediction point. It is obvious from this figure that the alignment of low inlet total pressure and temperature results in increased distortion tolerance. This is consistent with the requirement of a uniform exit static pressure. For a given distortion amplitude, the low inlet pressure side can achieve the same exit static pressure as the high inlet pressure side further from stall because it has a higher inlet corrected speed. The alignment of the low inlet total temperature with the low inlet pressure provides the desirable increase in corrected rotor speed. Consequently, the critical pressure distortion amplitude is higher than when there is no temperature distortion. When the low pressure and low temperature regions are opposed, the opposite effect of reduced inlet corrected rotor speed reduces distortion tolerance and the critical amplitude for stall. It is to be expected, then, that an engine will have a base level critical pressure distortion amplitude with no temperature distortion, and this level will increase or decrease as temperature distortion is imposed depending on the relative alignment.

From Figure 20 it is apparent that less pressure distortion was required to stall Engine Build B than Build A. This could be due to any number of things which contribute to variations in the engine operating line or stall line. It is not possible here to speculate the cause of the differences so they will only be noted for purposes of evaluating the model.

It should also be noted that no corrections for Reynolds number index were made to the model predictions for critical temperature distortion amplitude. At the low rotor speeds shown on Figure 20, the Reynolds number correction to the predicted critical pressure distortion amplitude was approximately $-.01$. Since the critical temperature distortion amplitude with no pressure distortion (measured at $RNI = 0.5$) was approximately one and one-half times the measured critical pressure distortion with no temperature distortion, it may be that the predicted values of temperature distortion (predicted for $RNI = 1.0$) should be altered by at least the same correction. With no experimental justification to make a correction from a RNI of 1.0 to a RNI of 0.5 , however, none was made to the model predictions.

Influence of Relative Distortion Orientation

The NASA LeRC engine data with combined pressure and temperature distortion provided some insight into the manner in which these two types of distortions can complement or offset one another. However, it was of interest to explore this facet of distorted flow beyond the available data. For this reason the multiple segment model was exercised for a series of arbitrary combinations of 180° pressure and temperature distortions. These calculations were all performed at a low rotor corrected speed of 8600 RPM. Engine matching conditions were assumed to be identical to those defined from 180° pressure distortion data analyzed in reference 1 and presented in Figures 6, 7 and 8.

For the first series of calculations the low pressure and low temperature regions were either aligned or opposed by 180° . Alignment again implies low inlet total pressure and low inlet total temperature occupy the same circumferential position. Temperature distortion amplitudes $(\max - \min) / \text{avg}$ of .04, .08 and .12 were imposed for each orientation, and the model calculated the critical pressure distortion amplitude required for engine stall. Results are shown in Figure 21. From this figure it can be seen that for each increment of .04 in temperature distortion, the critical pressure distortion amplitude changes by approximately 0.025 when the low pressure and low temperature are opposed, but is altered by smaller increments for increasing temperature distortions when low pressure and low temperature have the same relative alignment.

Other relative distortion orientations were also investigated at a low rotor speed of 8600 RPM. For this analysis the temperature distortion amplitude $(T_{T\max} - T_{T\min}) / T_{T\text{avg}}$ was held constant at a value of .08. The critical pressure distortion amplitude was determined for a total of four orientations differing by 90° circumferentially. Results are shown in Figure 22. The worst case investigated, on the basis of distortion sensitivity, had the low temperature and low pressure regions opposed. This was expected, as explained earlier, but the asymmetry of the figure requires some additional explanation. When the leading edge of the low inlet pressure and high temperature regions are separated by 90° , the engine sensitivity depends upon the order in which the rotor encounters the high temperature and the

low pressure regions. If the rotor meets the high temperature region 90° ahead of the low pressure region the predicted critical pressure distortion amplitude is lower than when the low pressure region leads the high temperature region by 90° . Classic parallel compressor theory would not predict any difference for these two cases. The present model's recognition of the distorted flow field effects makes the distinction possible. These effects alter the local and average pumping characteristics of the compressor so that the stall condition is altered for a given distortion level depending on orientation.

Classic parallel compressor theory would have the same average mass flow and mass flow distribution at the same inlet distortion amplitude. From Figure 23, it can be seen that similar average mass flows and mass flow distributions are predicted at stall by the multiple segment model, but the pressure distortion amplitudes differ by 0.4 (Figure 22). Whether it is a critical minimum flow or a critical minimum circumferential extent of mass flow below the uniform inlet stall mass flow (approximately 42.2 kg/sec, 93 lbs/sec) that must be reached to have a stall, it is clear that the order of the distortions influences the critical distortion amplitude. It should be noted that a fixed engine operating line was assumed in all of these calculations for critical distortion amplitude. The different compressor pumping characteristics demonstrated with different orientation may have a secondary effect due to induced changes in bypass ratio and engine operating line.

Influence of Compressor Bleeds

The TF30 P-3 engine is equipped with overboard bleed systems at the seventh and the twelfth compressor stages. Use of these bleeds alters the engine operating match point and provides additional distortion stall margin. The multiple segment model was exercised with the seventh alone, twelfth alone and both bleeds together. For the seventh stage bleed 6.3% of local mass flow rate was removed from each segment. Six percent of local mass flow was removed to represent the twelfth stage bleed. These amounts are consistent with TF30 P-3 engine specifications. The change in the engine operating match point due to the bleeds was analytically determined using a P&WA engine matching computer program. A summary of pertinent engine parameters for bleeds closed and for the various combinations of bleeds open on the 180° inlet critical pressure distortion level is provided in Table I.

TABLE I – EFFECT OF BLEEDS ON CRITICAL INLET PRESSURE DISTORTION

Bleed Condition		Engine Bypass Ratio	$N1/\sqrt{\theta T_2}$ RPM	$N2/\sqrt{\theta T_3}$ RPM	Total Corrected Airflow		Distortion Level at Stall $P_{Tmax} - P_{Tmin}$ P_{Tavg}	
7th	12th				kg/sec	(lb/sec)	Model Prediction	Data
Closed	Closed	1.37	8200	10100	92.5	204	0.147	0.115*
Open	Closed	1.28	8200	10200	92.5	204	0.24	0.22**
Closed	Open	1.30	8200	10300	92.5	204	0.24	0.21**
Open	Open	1.23	8200	10500	92.5	204	0.37	N/A

*NASA LeRC Data (8190 RPM)

**P&WA Data

The increased distortion tolerance is attributed to the large shift in engine operating point indicated by the bypass ratio. No NASA LeRC data was available to verify the bleeds open predictions, but P&WA engine data was available for the cases where the two bleeds were opened independently. Note that the model consistently overpredicts the critical distortion level by approximately 0.03. This error may be due to either the uncertainty in the original base engine match point determined from the NASA data, or to the extrapolated blade row performance characteristics, or both. The important point is that the trend due to the effect of bleeds on distortion tolerance has been accurately modeled.

Table II documents the results of similar model predictions for the influence of compressor bleeds on temperature distortion sensitivity.

TABLE II – EFFECT OF BLEEDS ON CRITICAL INLET TEMPERATURE DISTORTION

Bleed Condition		Engine Bypass Ratio	$N1/\sqrt{\theta T_2}$ RPM	$N2/\sqrt{\theta T_3}$ RPM	Total Corrected Airflow		Distortion Level at Stall $T_{Tmax} - T_{Tmin}$ T_{Tavg}	
7th	12th				kg/sec	(lb/sec)	Prediction	Data
Closed	Closed	1.53	7700	9980	85.9	189	0.18	0.15
Open	Closed	1.41	7700	10060	86.2	190	0.43	—
Closed	Open	1.44	7700	10210	86.2	190	0.38	—
Open	Open	1.36	7700	10290	86.2	190	0.60	—

No NASA LeRC or P&WA bleeds-open data are available to verify these calculations. It is evident, however, the compressor bleeds have a similar powerful influence on temperature distortion tolerance through the large shift in the operating point indicated by the change in bypass ratio.

Stall Sites

High response pressure records supplied by NASA LeRC were investigated to determine the location of the initial instability. As mentioned earlier, the multiple segment model prediction placed the initial stall in the low pressure compressor. Since each component was modeled using its inlet and exit boundary conditions (fan-station 2.0 and 2.6F, LPC-station 2.0 and 3.0, HPC-station 3.0 and 4.0), it was not possible to predict the location with any more precision. The following Table III shows the agreement with the model.

TABLE III – ORIGIN OF INSTABILITY

Rdg No	Distortion	$N1/\sqrt{\theta}$	Location of Initial Instability	
			Measured	Predicted
330	180° Pressure	7300	2.3 – 2.6	LPC
331	180° Pressure	7900	2.3 – 2.6	LPC
336	180° Pressure	8200	2.3 – 2.6	LPC
341	180° Pressure	8600	LPC	LPC
359	120° Pressure	8167	2.6 – 3.0	LPC
372	120° Pressure	7417	LPC	LPC
7	180° Temperature	7680	2.6 – 3.0	LPC
159	180° Combined (Aligned)	7766	Insufficient Data	LPC
161	180° Combined (Opposed)	7852	LPC	LPC

CONCLUSIONS AND RECOMMENDATIONS

The results of the distortion sensitivity and attenuation study performed on the TF30 P-3 engine using the P&WA multiple segment parallel compressor model compared to the experimental performance of the engine are summarized as follows:

- 1) Simple parallel compressor theory provided only a first order approximation of the critical distortion amplitude and attenuation for the 180° pressure distortion cases investigated.
- 2) The principle modifiers to the simple parallel compressor theory were the circumferential cross flow and unsteady rotor loss effects accounted for in the multiple segment model. Circumferential cross flow increased the distortion of inlet mass flow and the rate of distortion attenuation through the front stages of the compression system. Cross flow decreased the tolerance of the compression system to distortion. Unsteady rotor loss effected primarily the distortion sensitivity, improving the compression systems' predicted tolerance to distortion.

- 3) The critical distortion level predictions using the multiple-segment parallel compressor model were subject to uncertainties in the compressor blade performance characteristics and the assumed engine operating line
- 4) Multiple segment model predictions of tolerance to 180° pressure distortion were accurate at the lower speeds investigated, but overpredicted the critical distortion amplitude at the higher speeds investigated
- 5) The model predicted the correct trend of tolerance to reduced circumferential extents of pressure distortion, showing that the compression system was less sensitive to extents less than 120° . This is in contrast to classic parallel compressor theory which predicted the opposite trend
- 6) The model predictions for 180° temperature distortion attenuation appeared to be accurate based upon limited experimental data. The accuracy of the critical distortion prediction could not be assessed because of possible performance differences between the 2 engine builds and 2 levels of RNI used in the investigation
- 7) The model was used to predict the critical amplitude for arbitrary orientations of combinations of pressure and temperature distortion. Limited data verified the predicted trends
- 8) Compressor overboard bleeds provided large improvements in distortion tolerance to both pressure and temperature distortion. Predicted effects of bleeds on pressure distortion sensitivity were verified by P&WA data. No data were available to verify their influence on temperature distortion sensitivity
- 9) For the range of low rotor speeds investigated (7300 - 8600 RPM) all stalls initiated in the low pressure compressor of the TF30 P-3. This was in agreement with the multiple segment model predictions

As a continuation of this effort toward increased understanding of engine response to circumferential distortion, the following actions are recommended

- 1) Since unsteady flow effects can alter the pumping characteristics of a compressor, it is possible that operating line shifts will occur which influence distortion sensitivity. This possibility should be explored by taking detailed measurements (including distortion rotation) necessary to accurately calculate engine bypass ratio under distorted flow conditions
- 2) Alternate stability criteria should be explored which are less sensitive to extrapolation of compressor blade row performance characteristics

LIST OF SYMBOLS

τ	Unsteady Rotor Loss Time Constant
t	Time
K	Proportionality Constant
b	Rotor Blade Chord Length
U	Fluid Velocity (Relative to Rotor)
P	Pressure
T	Temperature
$N1/\sqrt{\theta T_2}$	Corrected Low Rotor Speed
$N2/\sqrt{\theta T_3}$	Corrected High Rotor Speed
Q	Dynamic Pressure
Loss	Blade Loss (Entropy Rise)
W	Mass Flow Rate
θ	(a) Temperature/Std Day Temp (b) Circumferential Location
δ	Pressure/Std Day Pressure
LPC	Low Pressure Compressor
HPC	High Pressure Compressor
BPR	Engine Bypass Ratio (Fan Duct Flow/Primary or Core Engine Flow)
RNI	Reynolds Number Index, $\delta/\phi\sqrt{\theta}$
ϕ	Abs Viscosity/Std Day Abs Viscosity

Subscripts

Superscripts

Q S	Quasi-Steady State	—	Average
max	Maximum		
min	Minimum		
avg	Average		
A	Air		
E	Primary Engine Core		
F	Fan Bypass Duct		
T	Total		
S	Status		
1	Low Pressure Spool		
2	High Pressure Spool		

REFERENCES

- 1) "Modeling and Analysis of the TF30 P-3 Compressor System With Inlet Pressure Distortion", R S Mazzawy, G A Banks, NAS CR-134996, April, 1976
- 2) "Effect of a 180° Extent Inlet Pressure Distortion on the Internal Flow Conditions of a TF30 P-3 Engine", C E deBogdan, J H Dicus, D G Evans and R H Soeder, NASA TM X-3267, September 1975
- 3) "Experimental Evaluation of a TF30 P-3 Turbofan Engine in an Altitude Facility Effect of Steady-State Temperature Distortion", W M Braithwaite, NASA TM X-2921, November 1973
- 4) "Technique for Inducing Controlled Steady-State and Dynamic Inlet Pressure Disturbances for Jet Engine Tests", C L Meyer, J E McAulay, T J Biesiadny, NASA TMX-1946, 1970
- 5) "Compressor Surge and Stall Propagation", H W Emmons, C E Pearson and H P Grant, Transactions of the ASME, May, 1955
- 6) "Compressor Critical Response Time Determination Study", R S Mazzawy, G A Banks, C. R Weber, AFAPL-TR-76-45, June, 1976

REFERENCES

- 1) "Modeling and Analysis of the TF30 P-3 Compressor System With Inlet Pressure Distortion", R. S. Mazzawy, G. A. Banks, NAS CR-134996, April, 1976.
- 2) "Effect of a 180° Extent Inlet Pressure Distortion on the Internal Flow Conditions of a TF30 P-3 Engine", C. E. deBogdan, J. H. Dicus, D. G. Evans and R. H. Soeder, NASA TM X-3267, September 1975.
- 3) "Experimental Evaluation of a TF30 P-3 Turbofan Engine in an Altitude Facility: Effect of Steady-State Temperature Distortion", W. M. Braithwaite, NASA TM X-2921, November 1973.
- 4) "Technique for Inducing Controlled Steady-State and Dynamic Inlet Pressure Disturbances for Jet Engine Tests", C. L. Meyer, J. E. McAulay, T. J. Biesiadny, NASA TMX-1946, 1970.
- 5) "Compressor Surge and Stall Propagation", H. W. Emmons, C. E. Pearson and H. P. Grant, Transactions of the ASME, May, 1955.
- 6) "Compressor Critical Response Time Determination Study", R. S. Mazzawy, G. A. Banks, C. R. Weber, AFAPL-TR-76-45, June, 1976.

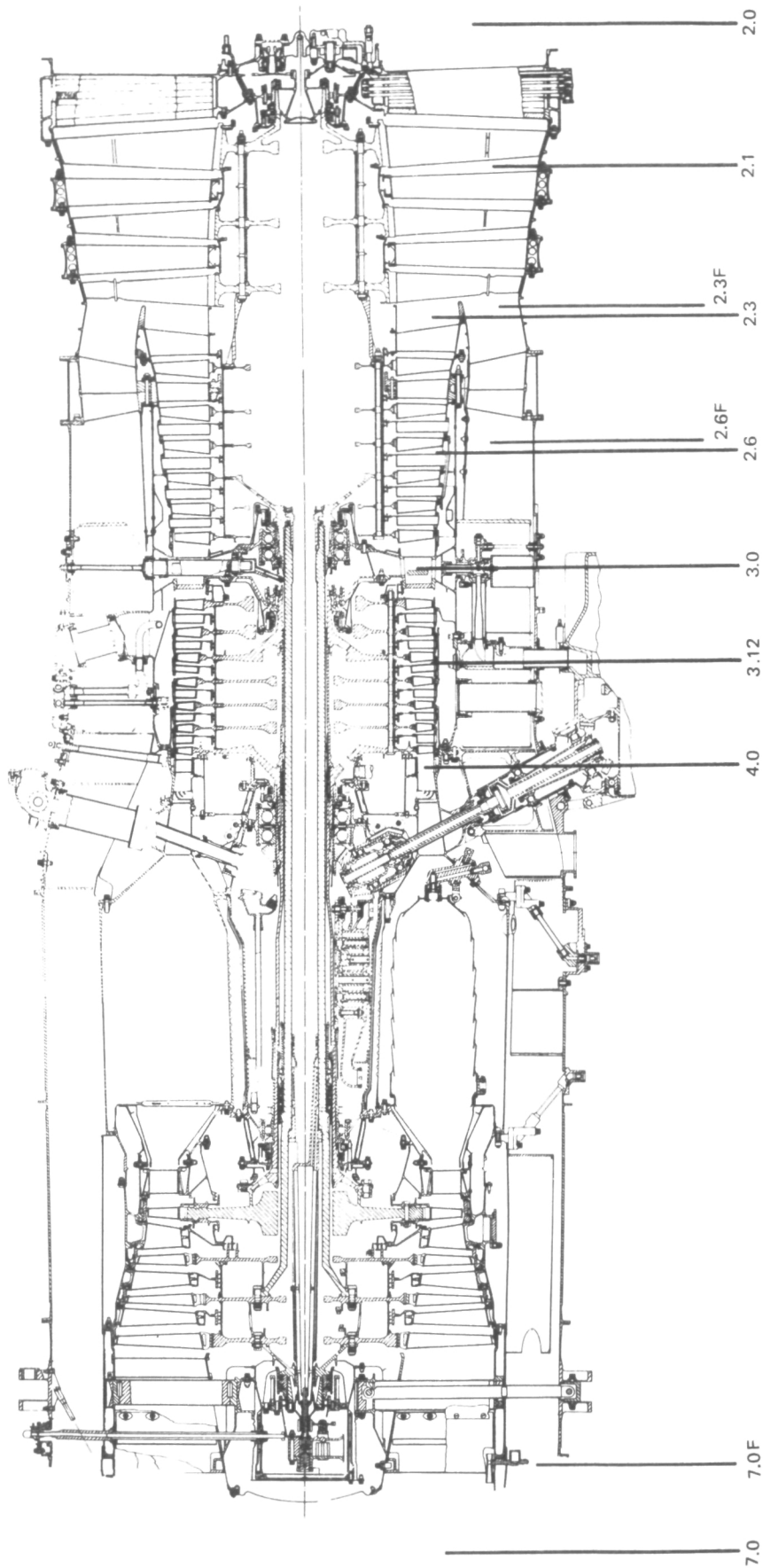


Figure 1 TF30 Engine Cross Section With Instrumentation Locations

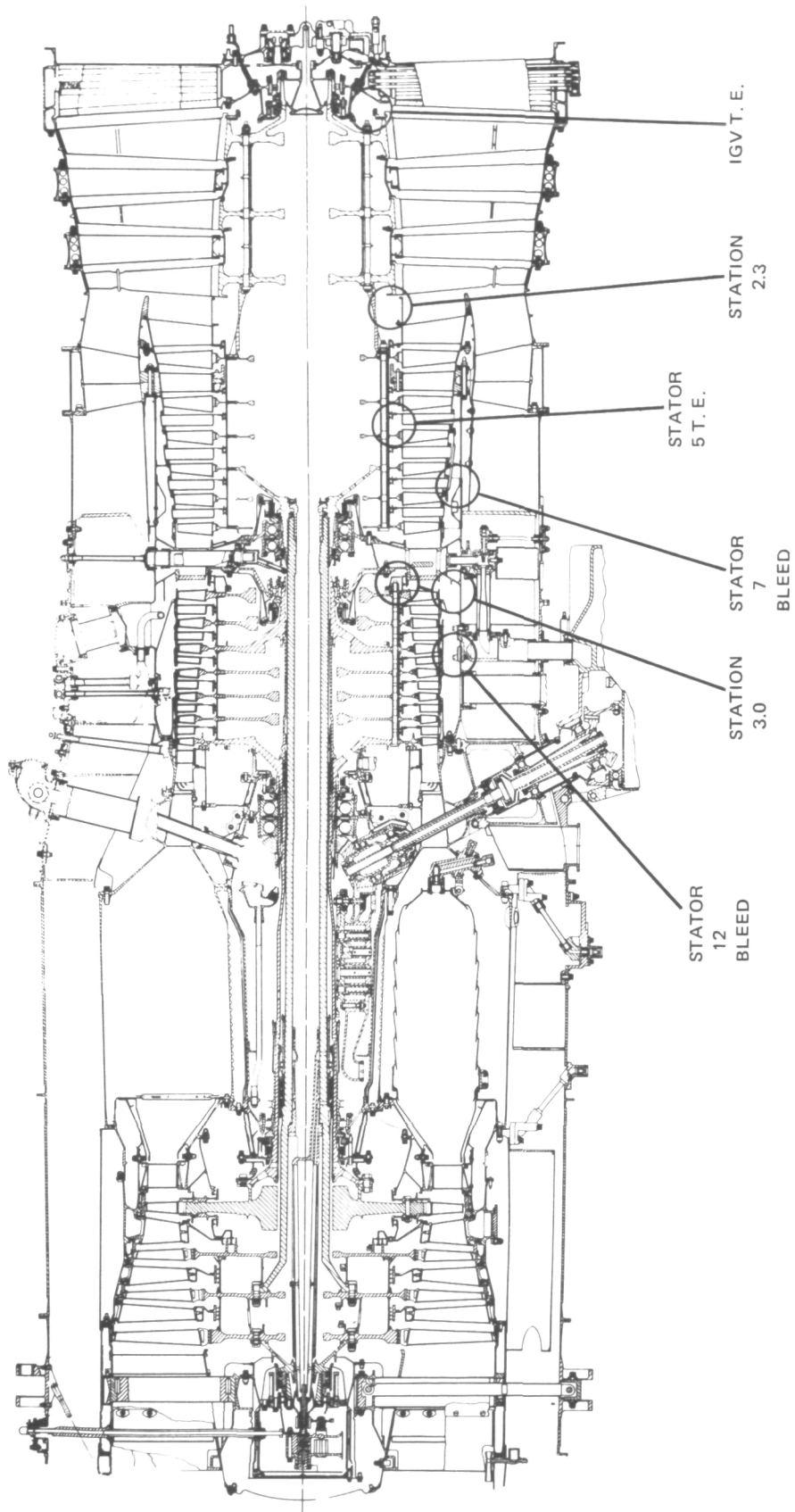


Figure 2 TF30 Engine Cross Section With Crossflow Cavity Locations

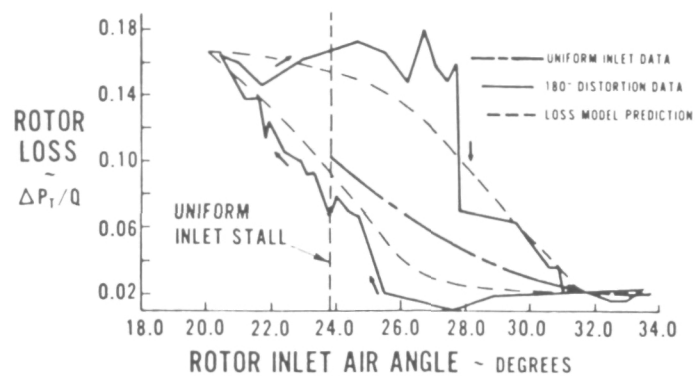


Figure 3 Rotor Response to Inlet Air Angle – Experimental Data and Prediction

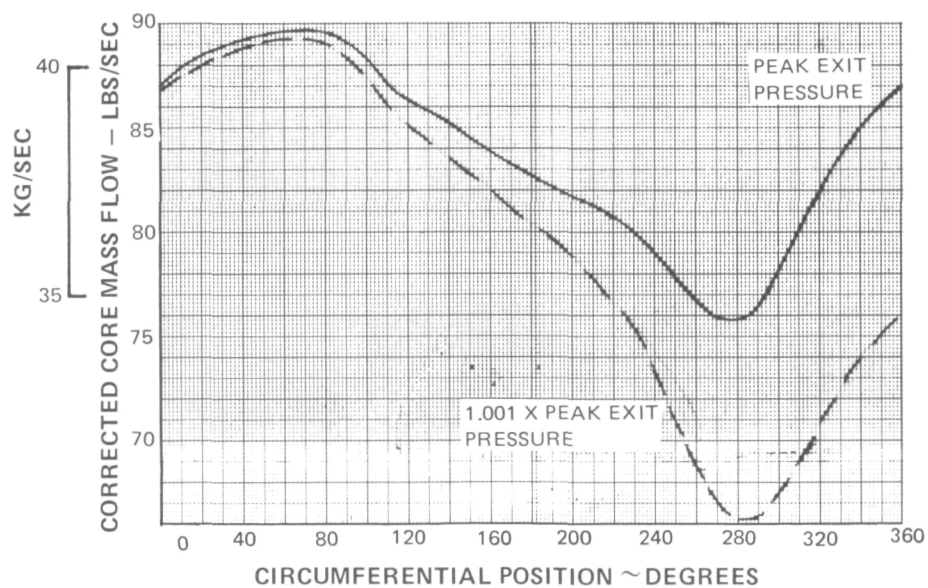


Figure 4 Model Calculation of Discontinuity in Mass Flow Distribution Caused by Exceeding Peak Exit Pressure

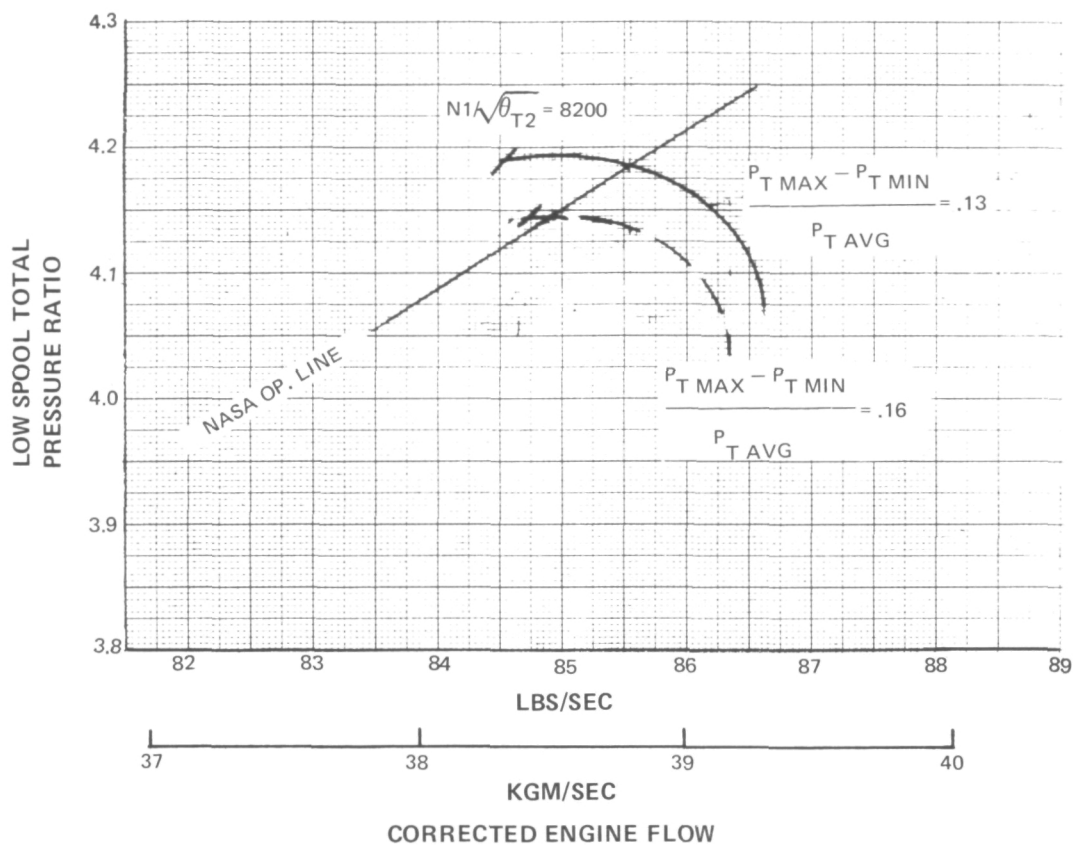


Figure 5 Example Determination of Critical Distortion Amplitude –
 $N_1/\sqrt{\theta_{T2}} = 8200$ RPM

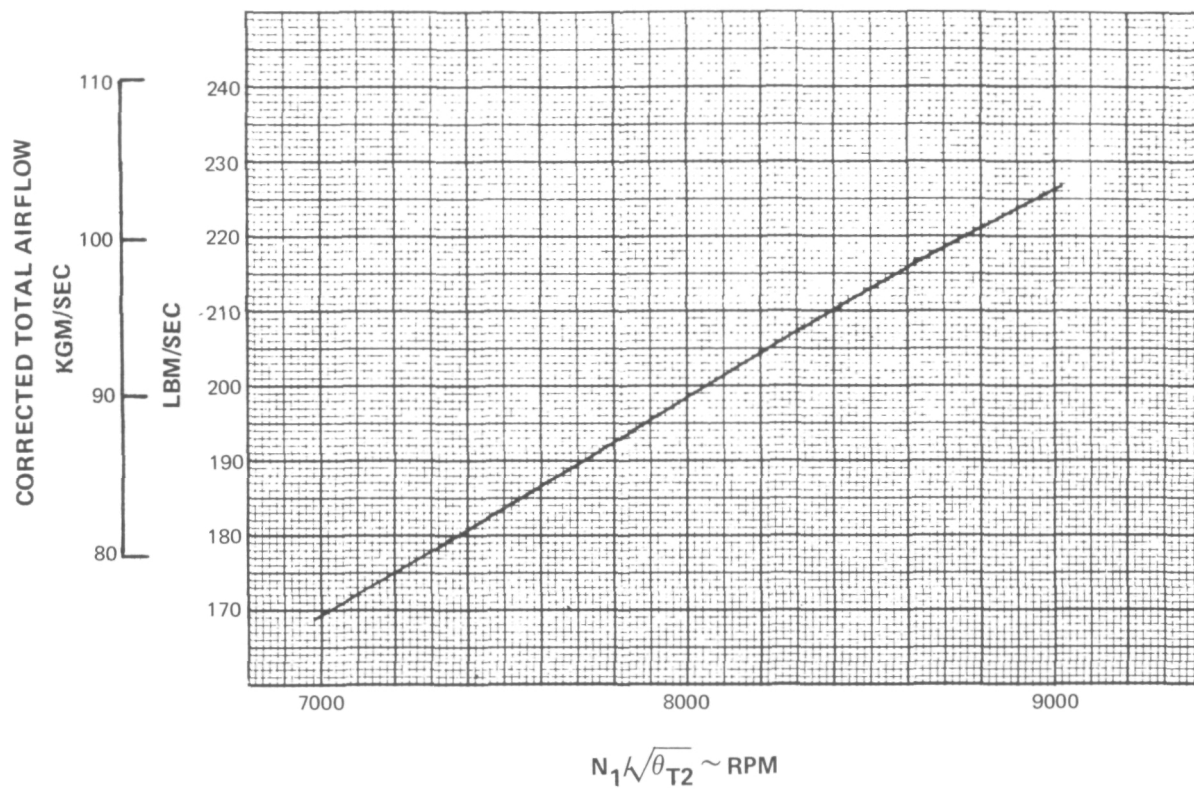


Figure 6 Total Corrected Airflow – Low Rotor Speed Characteristic at $RNI = 0.5$

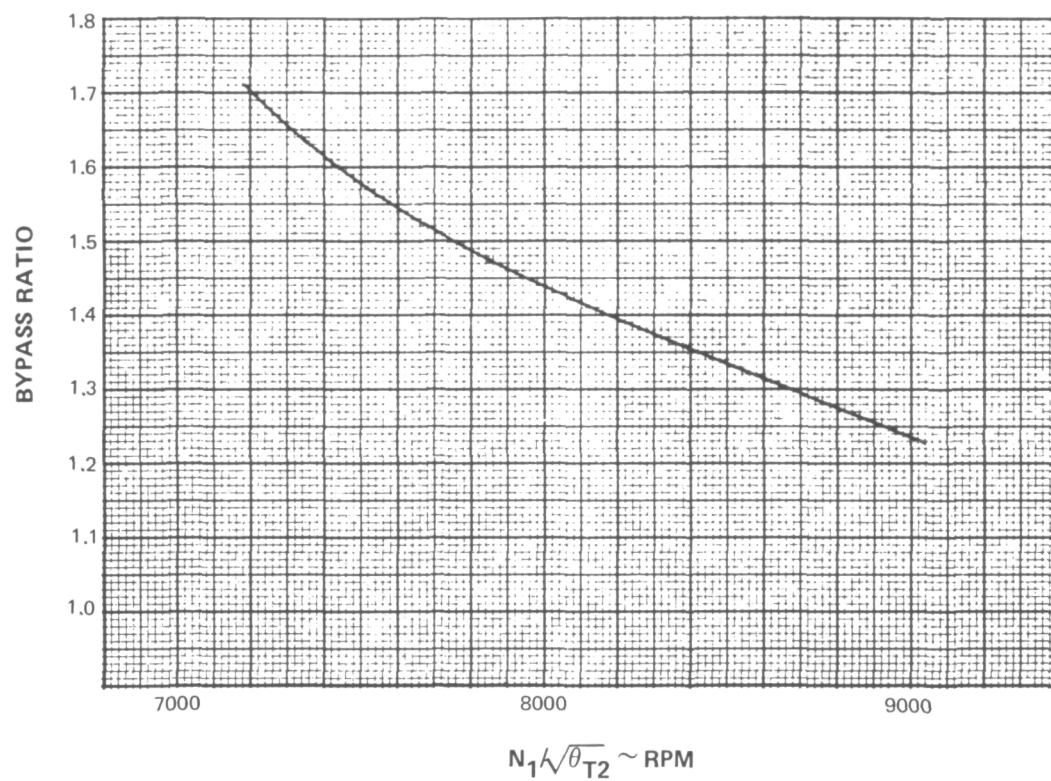


Figure 7 Bypass Ratio – Low Rotor Speed Characteristic at $RNI = 0.5$

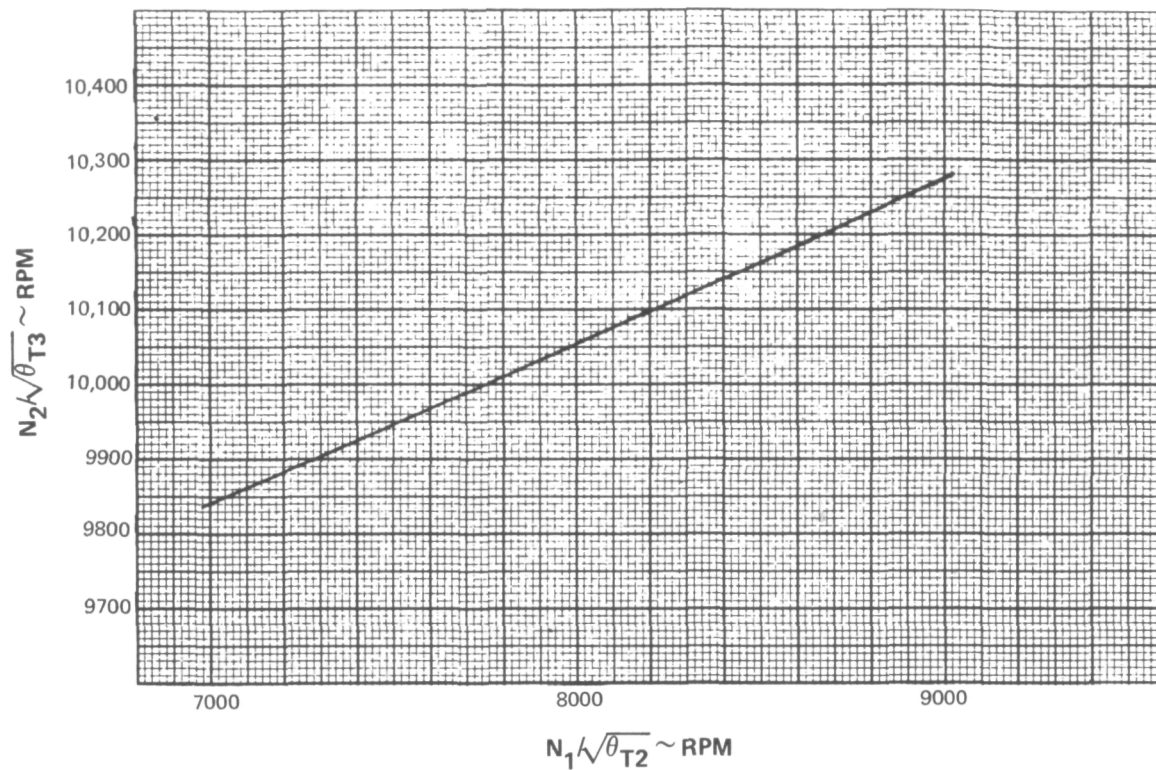


Figure 8 Corrected High Rotor Speed – Low Rotor Speed Characteristic
at RNI = 0.5

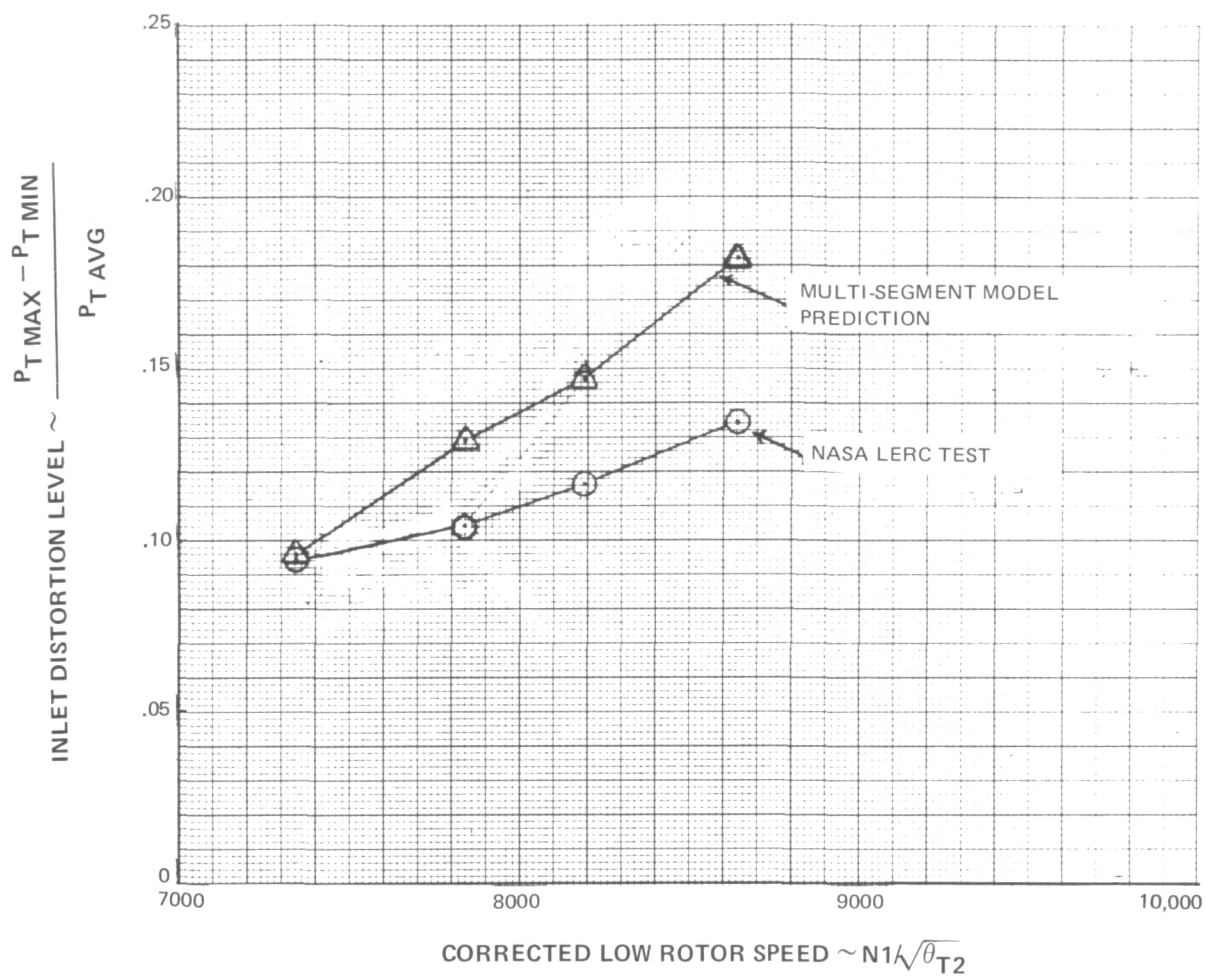


Figure 9 Comparison of Predicted Critical 180-degree Pressure Distortion Amplitude with Data, RNI = 0.5

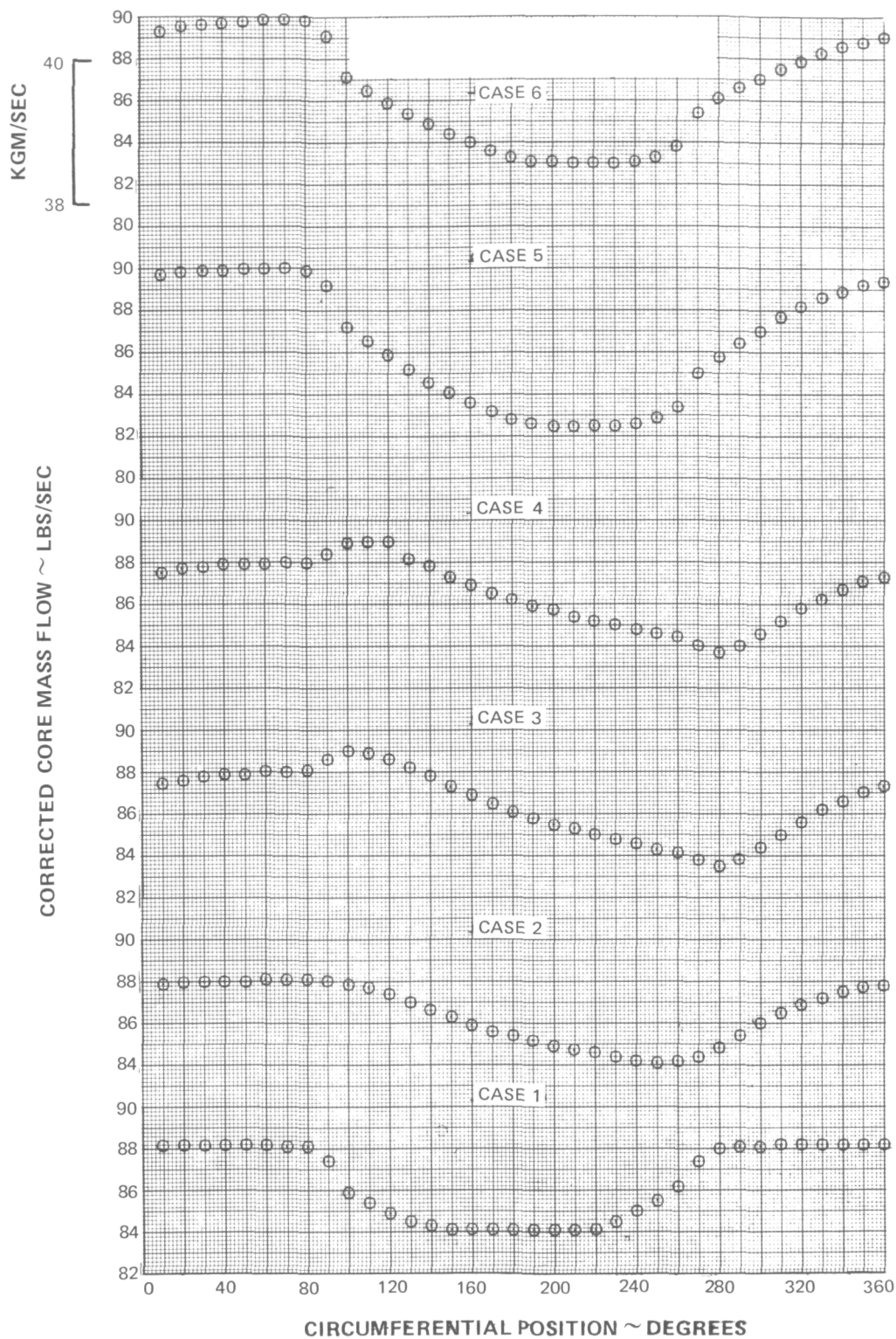


Figure 10 – Circumferential Variation of Predicted Flow Properties with 180-degree Pressure Distortion at $\Delta P_T/P_T = 0.116$, $N_1/\sqrt{\theta_{T2}} = 8200$ RPM

Figure 10a Inlet Core Corrected Airflow

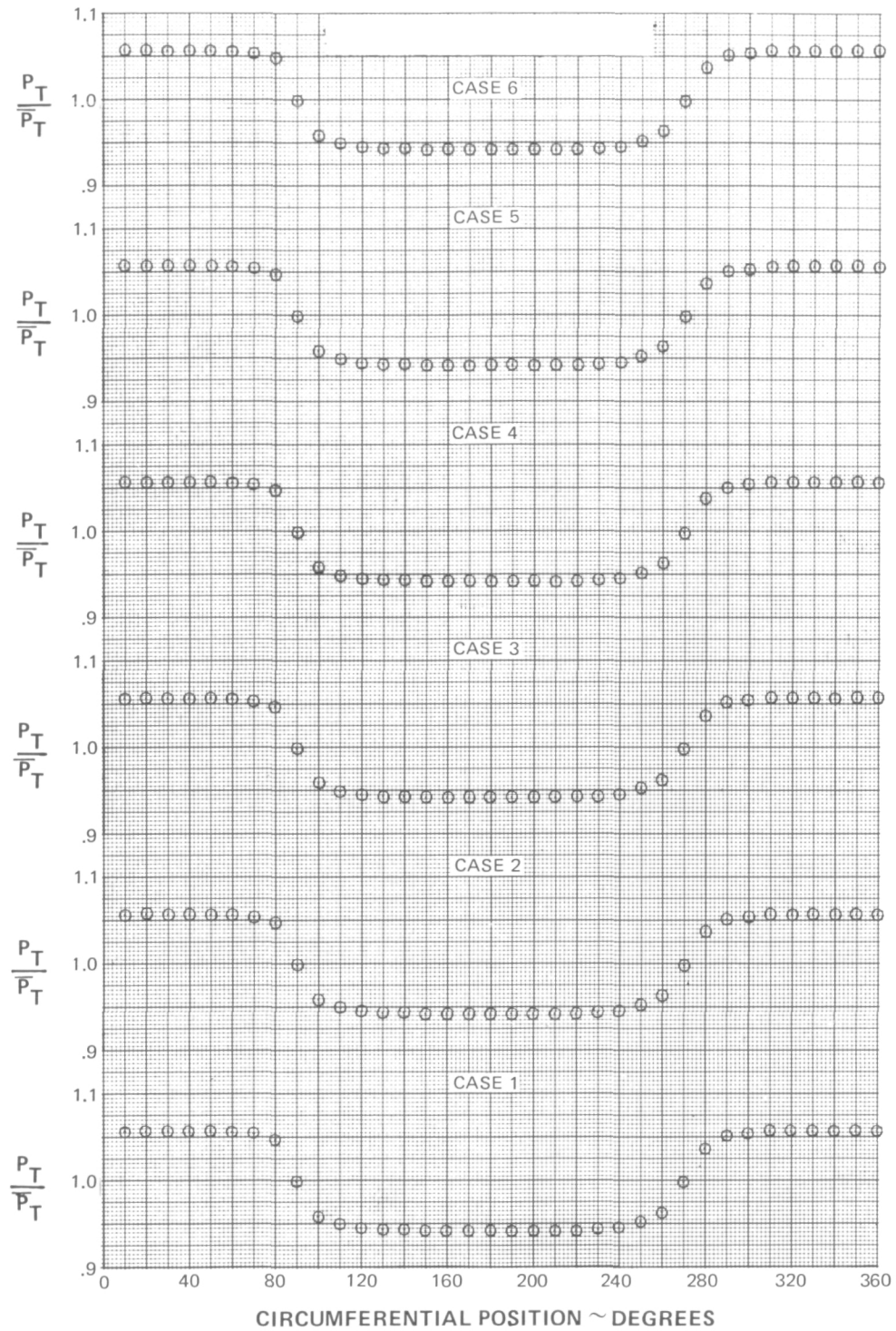


Figure 10b Station 2.0 Total Pressure Distortion

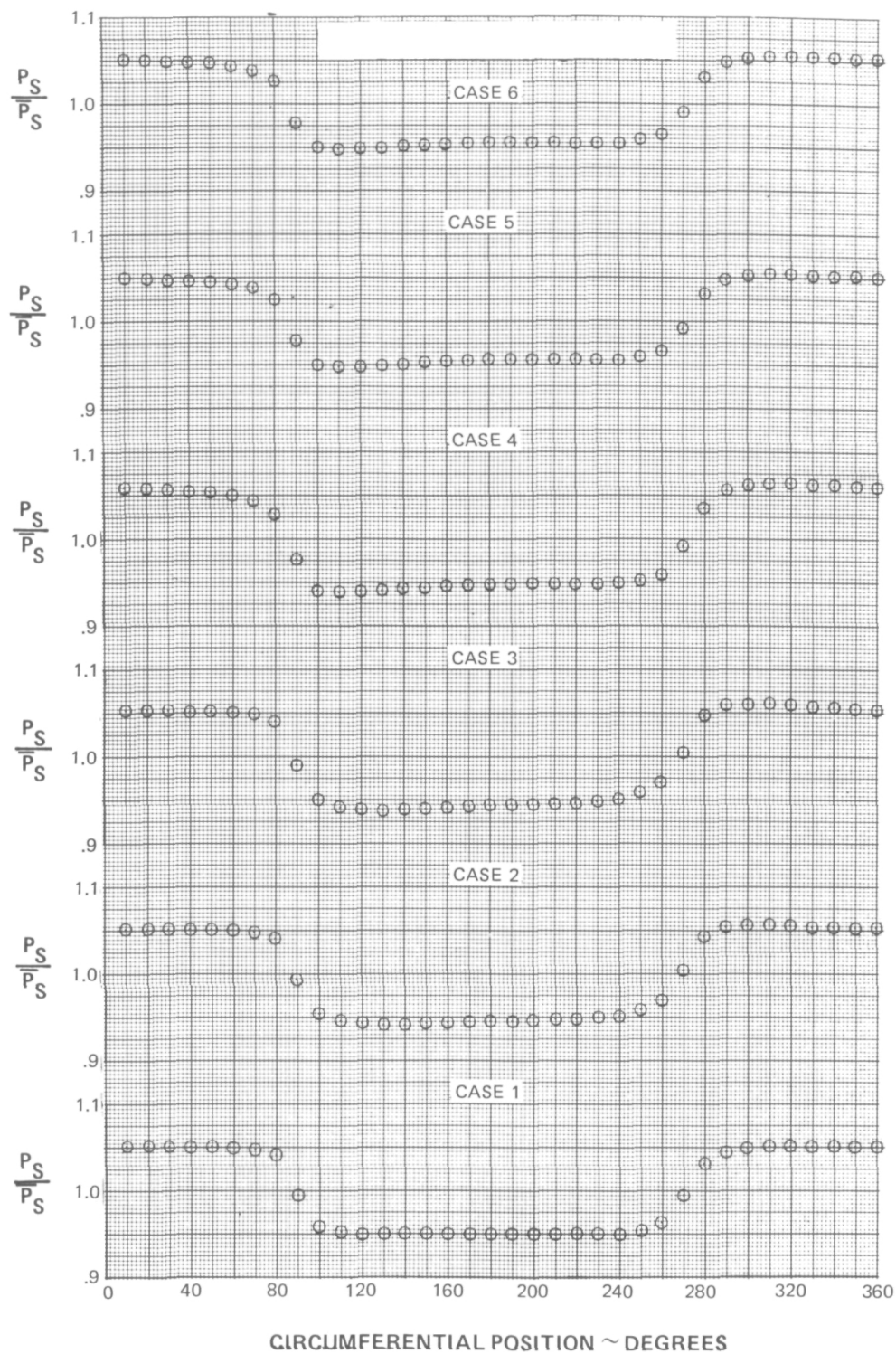


Figure 10c Station 2.0 Static Pressure Distortion

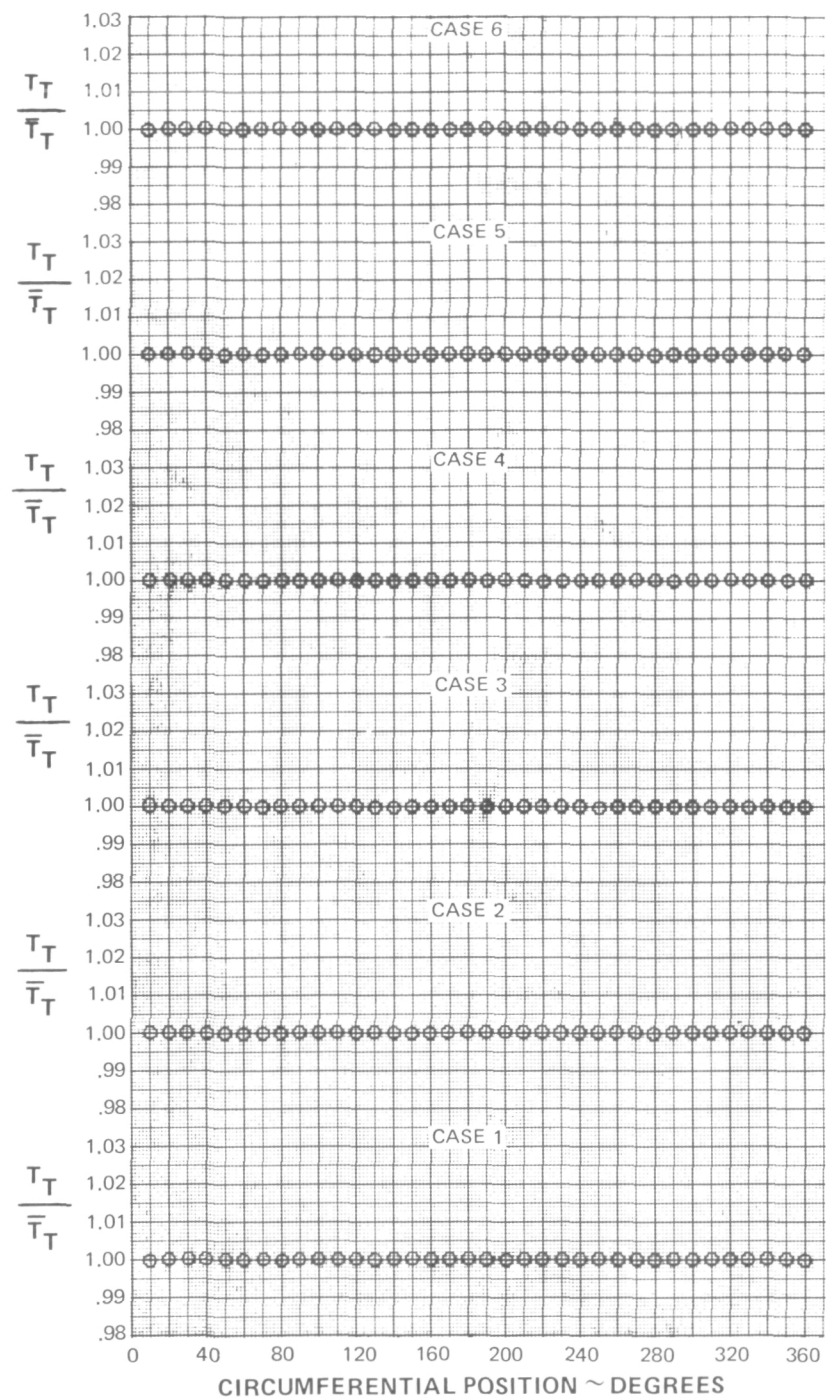


Figure 10d Station 2.0 Total Temperature Distortion

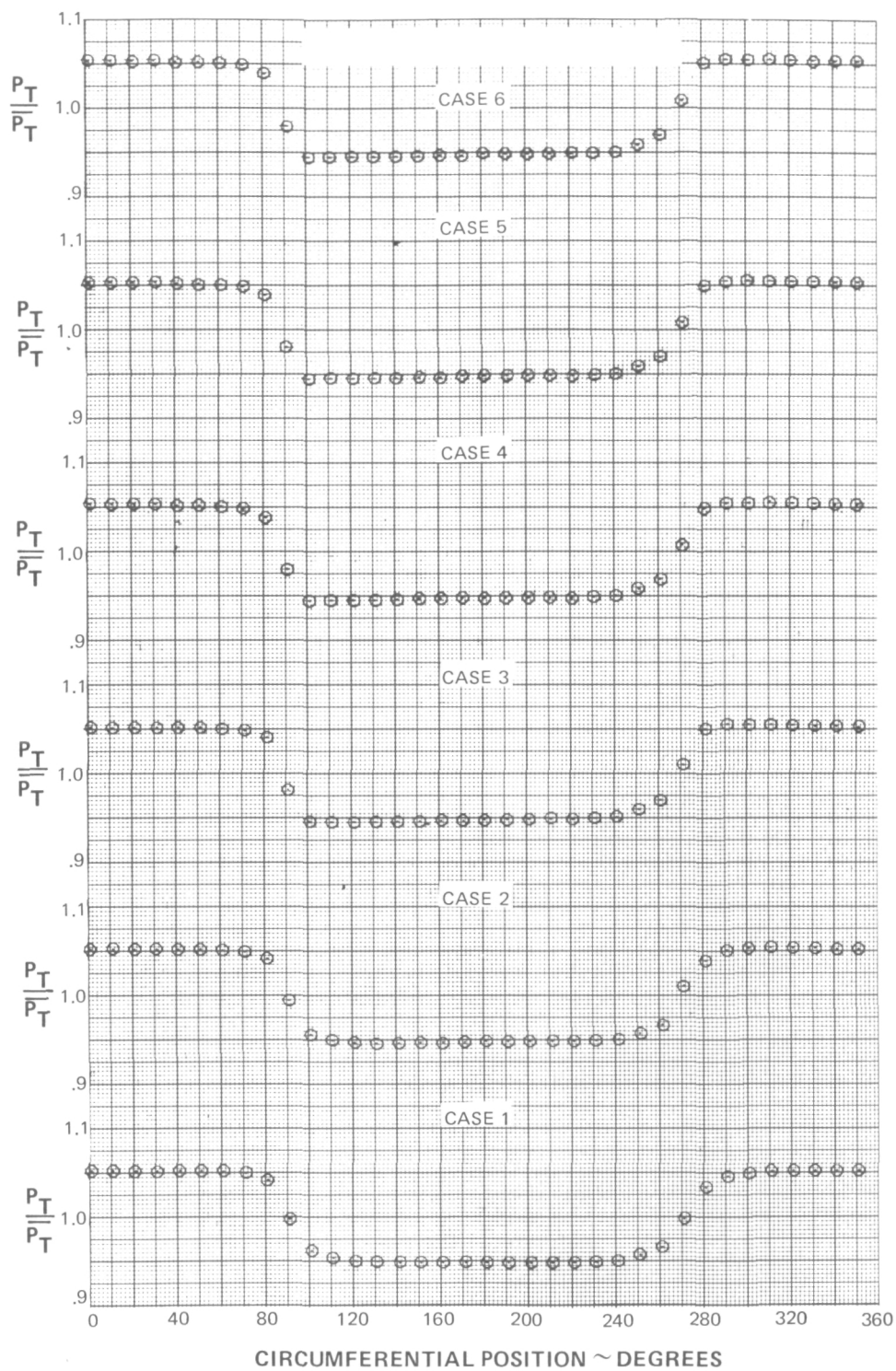


Figure 10e Station 2.1F Total Pressure Distortion

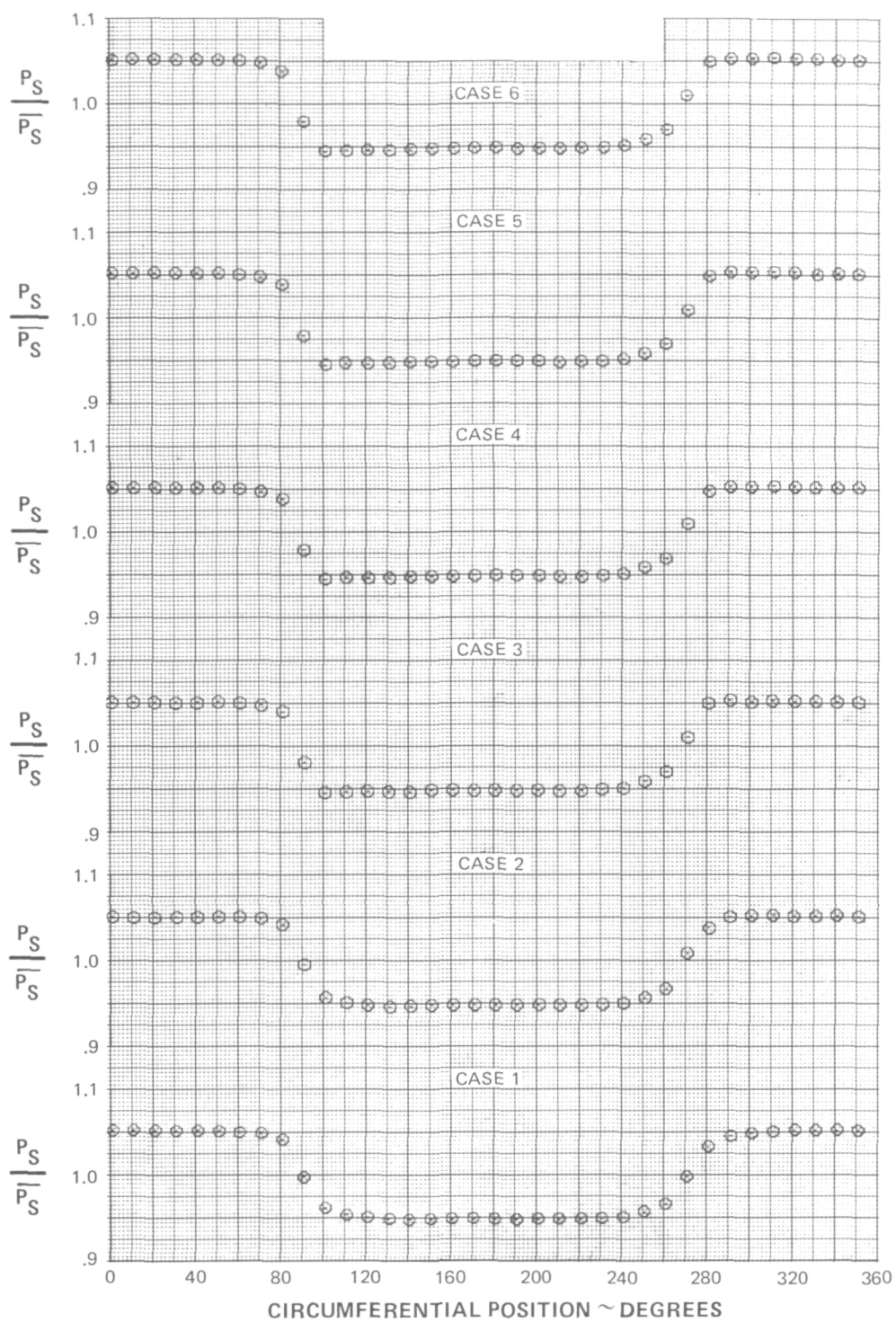


Figure 10f Station 2.1F Static Pressure Distortion

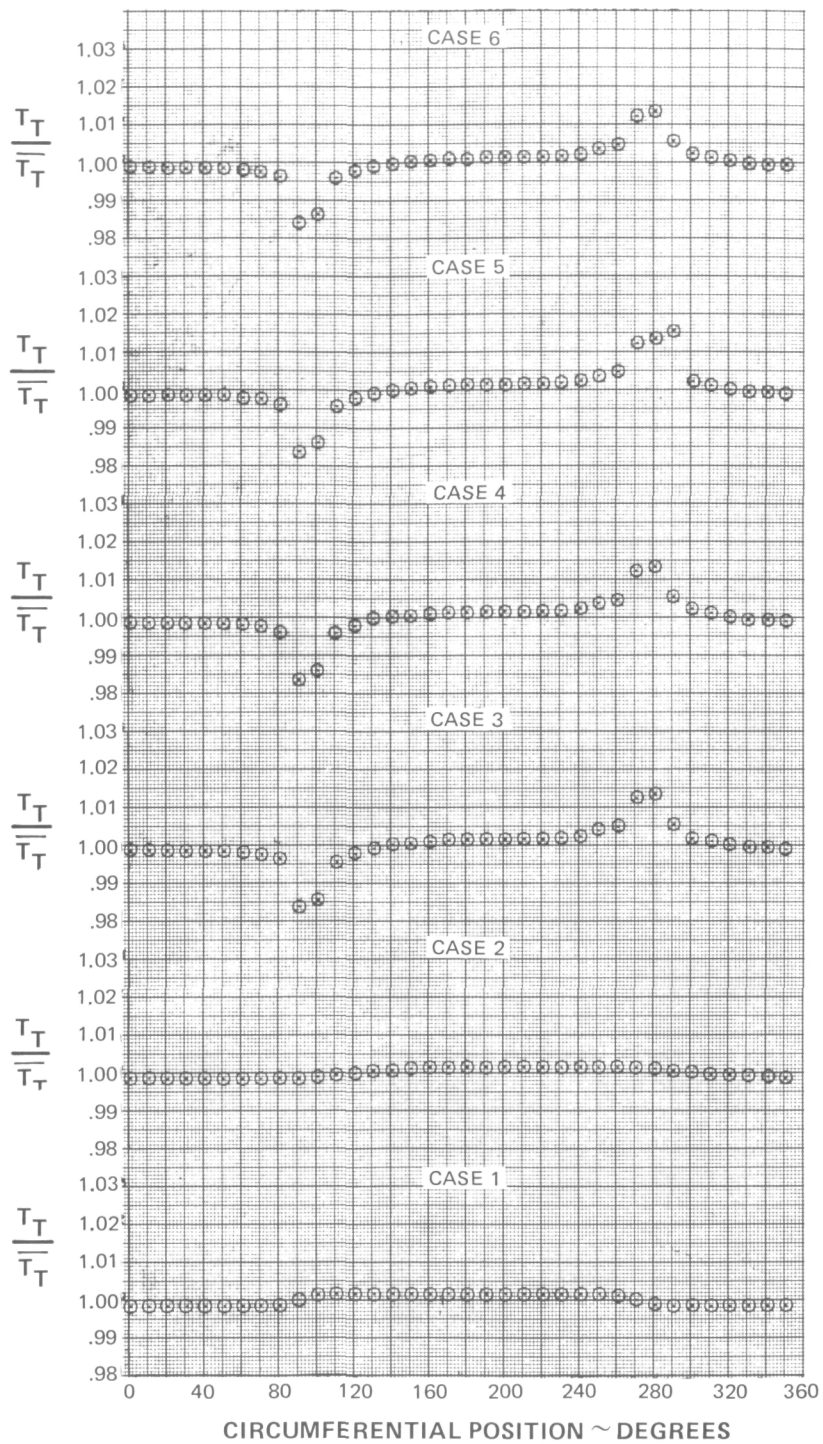


Figure 10g Station 2.1F Total Temperature Distortion

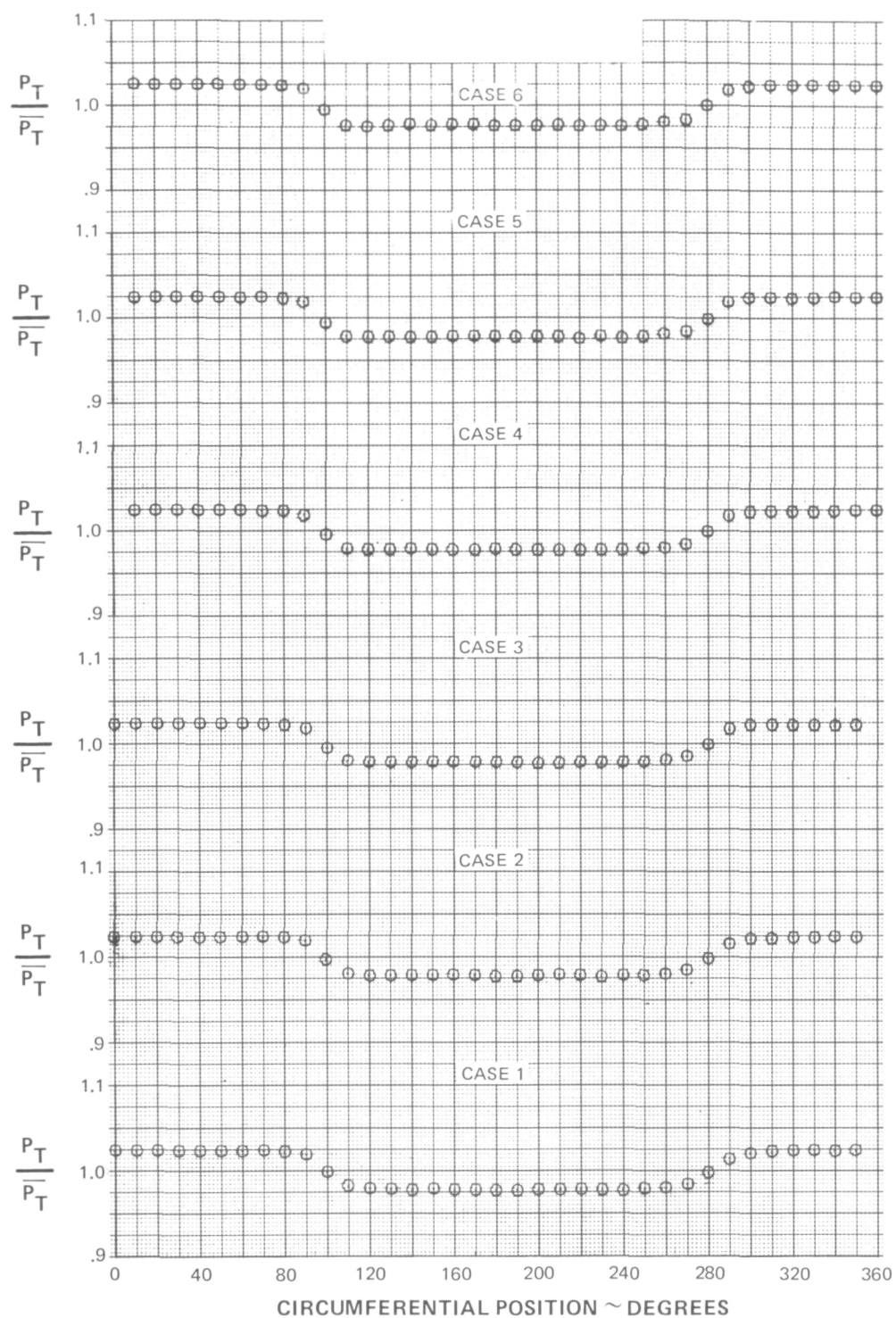


Figure 10h Station 2.3F Total Pressure Distortion

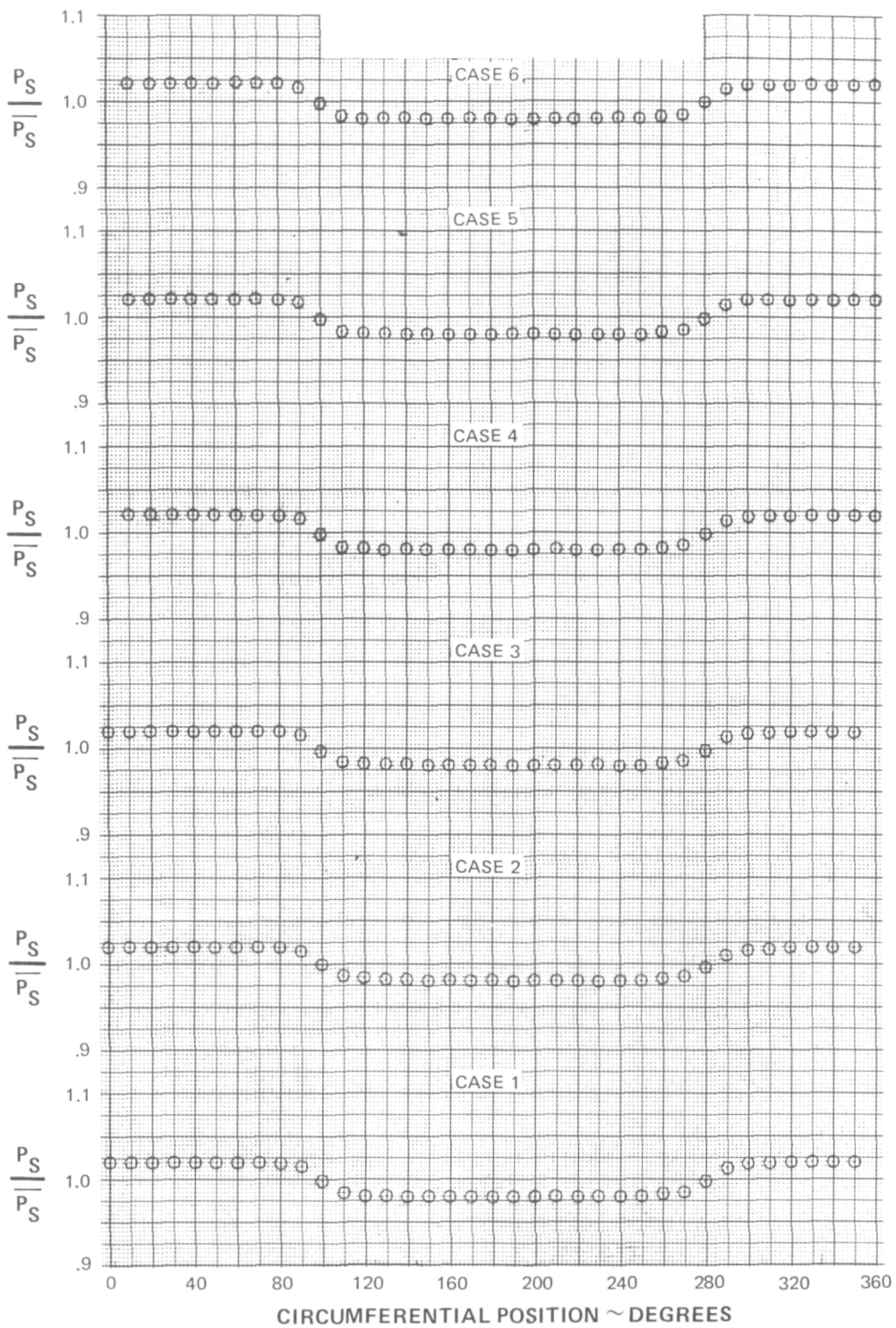


Figure 10i Station 2.3F Static Pressure Distortion

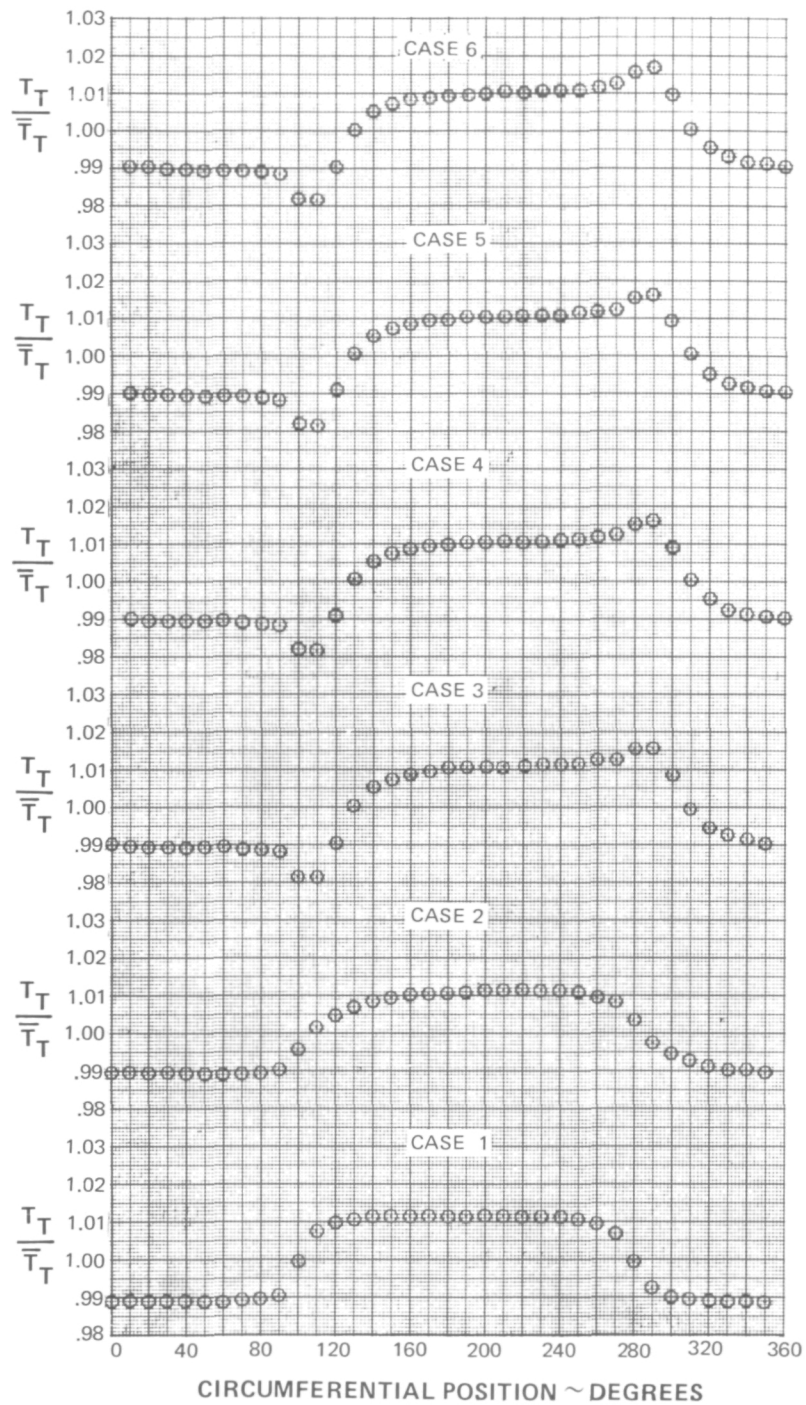


Figure 10j Station 2.3F Total Temperature Distortion

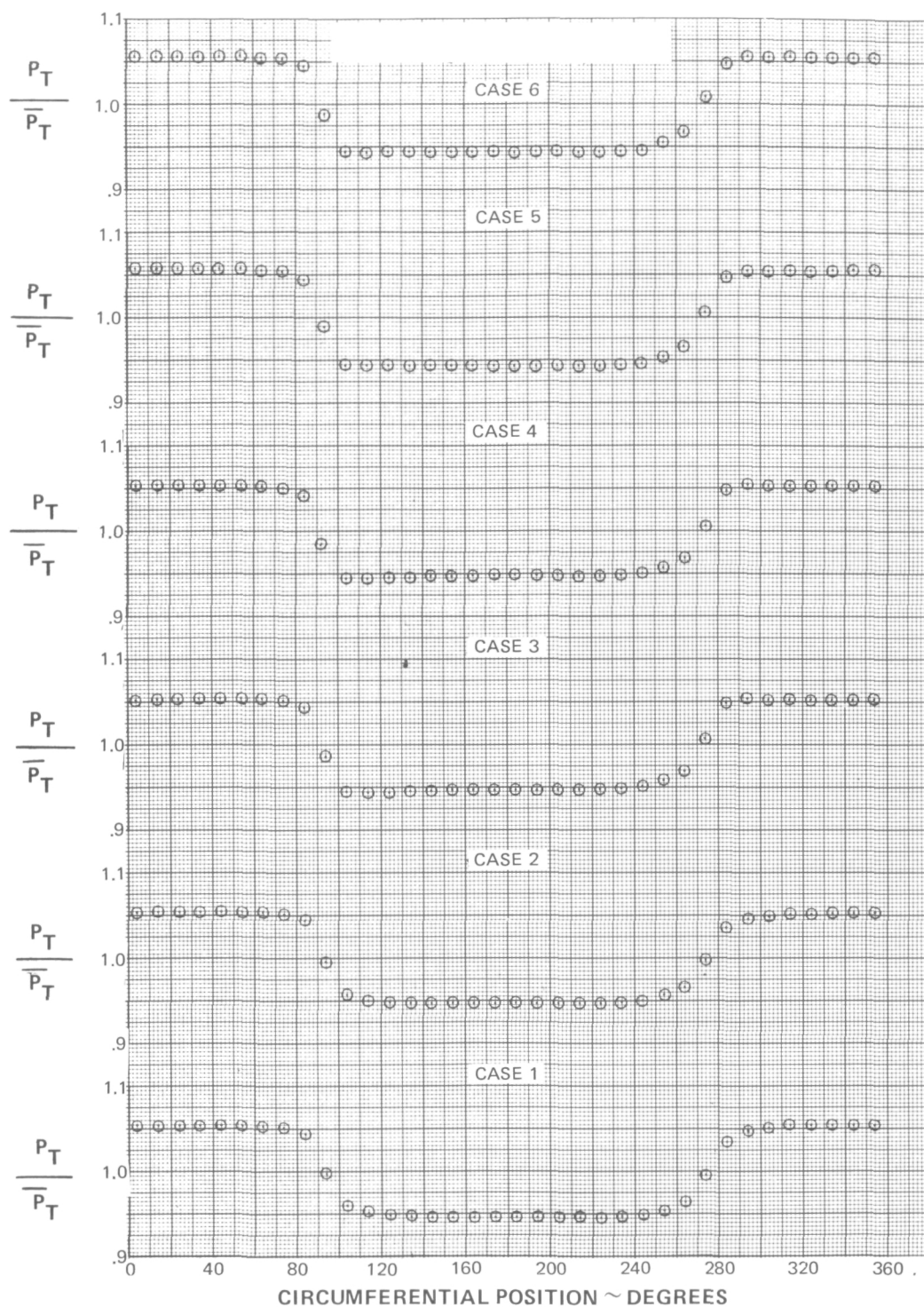


Figure 10k Station 2.1 Total Pressure Distortion

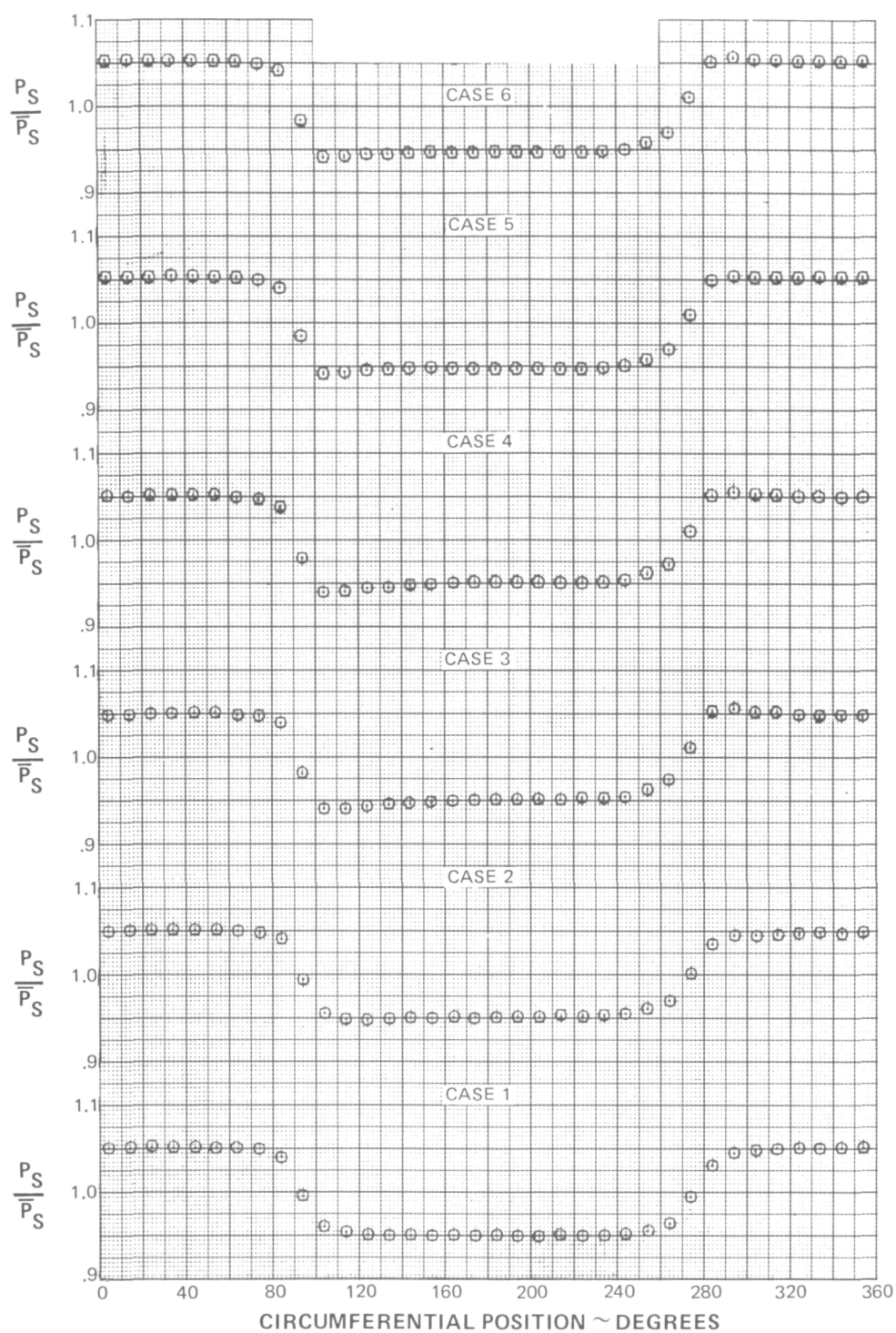


Figure 10l Station 2.1 Static Pressure Distortion

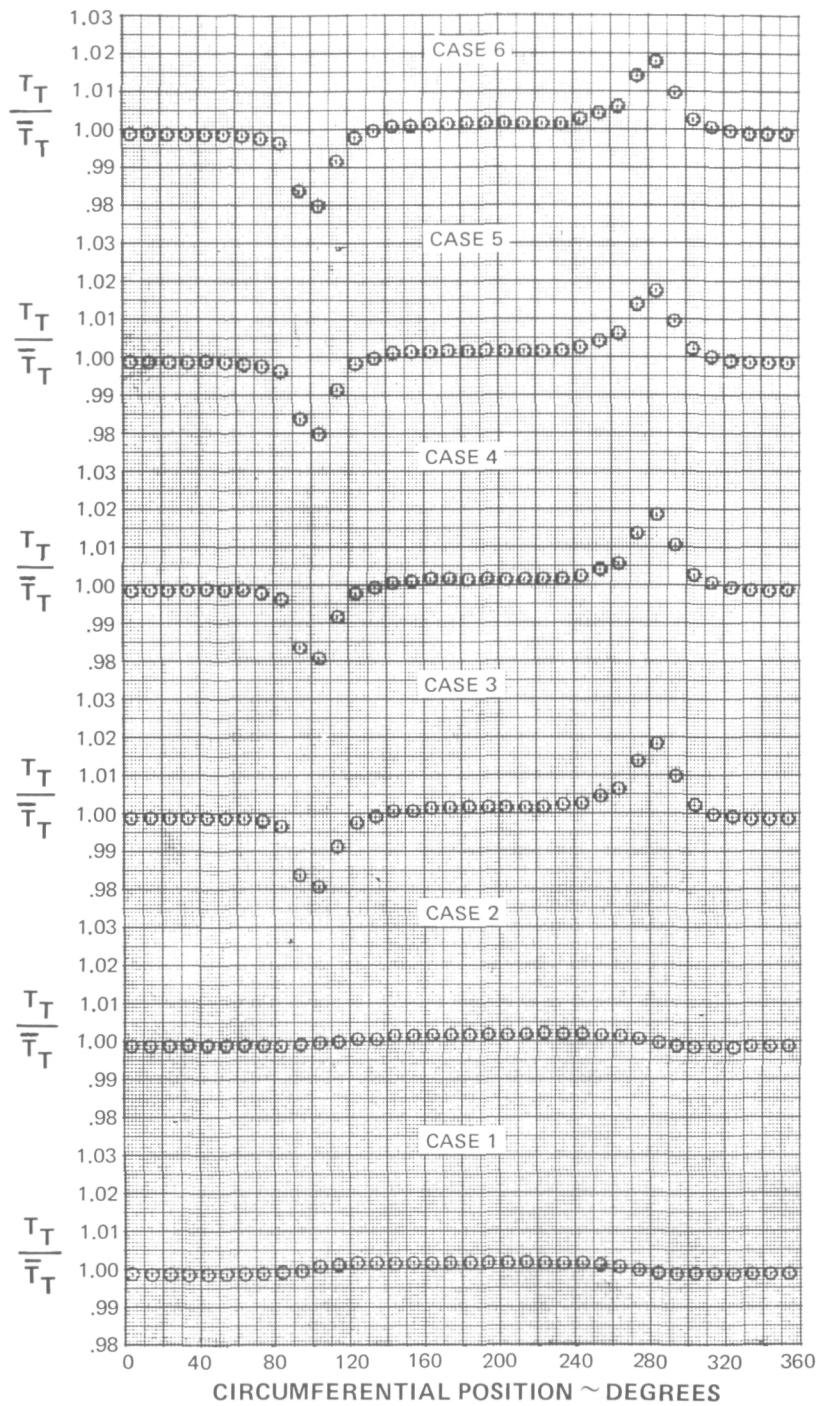


Figure 10m Station 2.1 Total Temperature Distortion

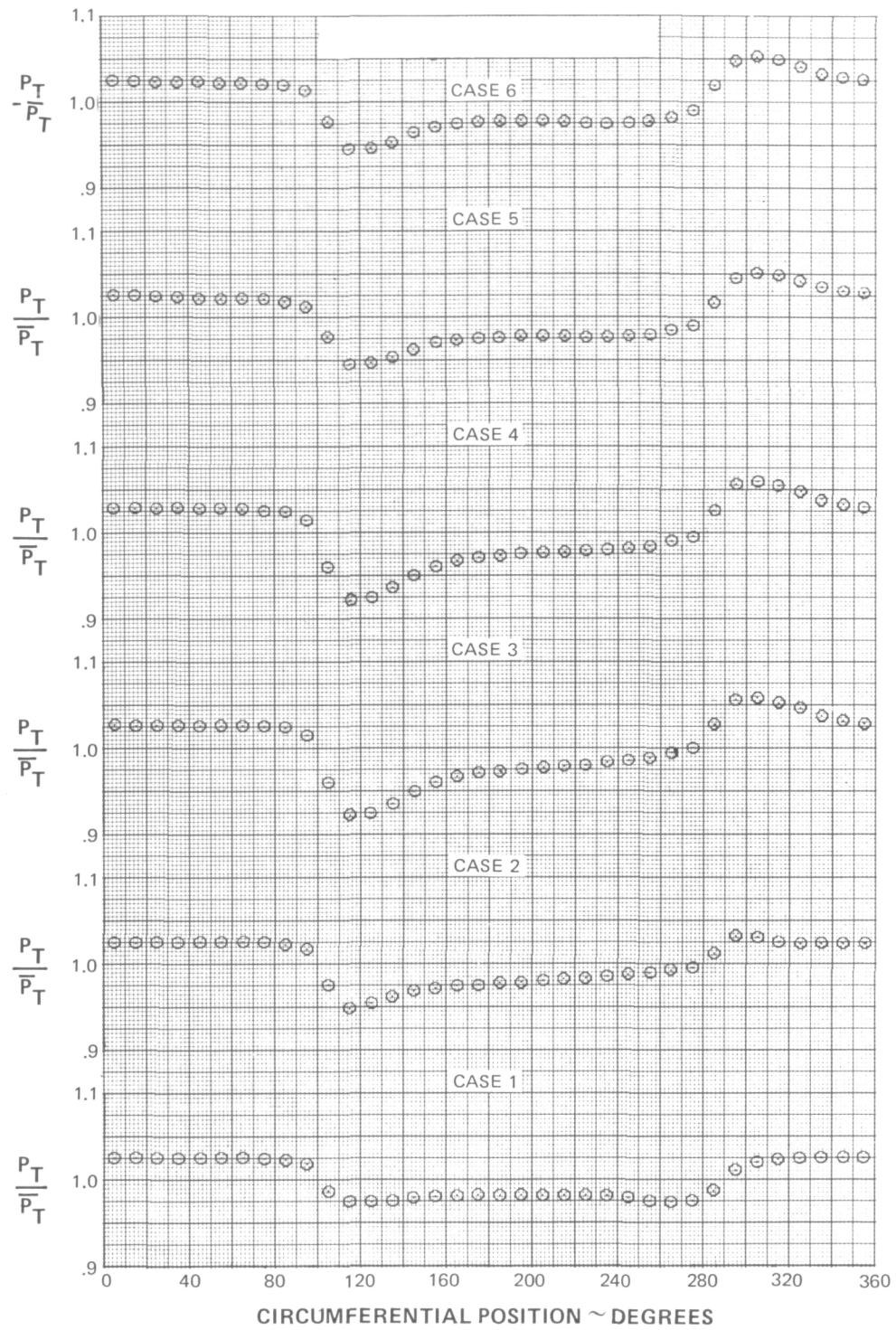


Figure 10n Station 2.3 Total Pressure Distortion

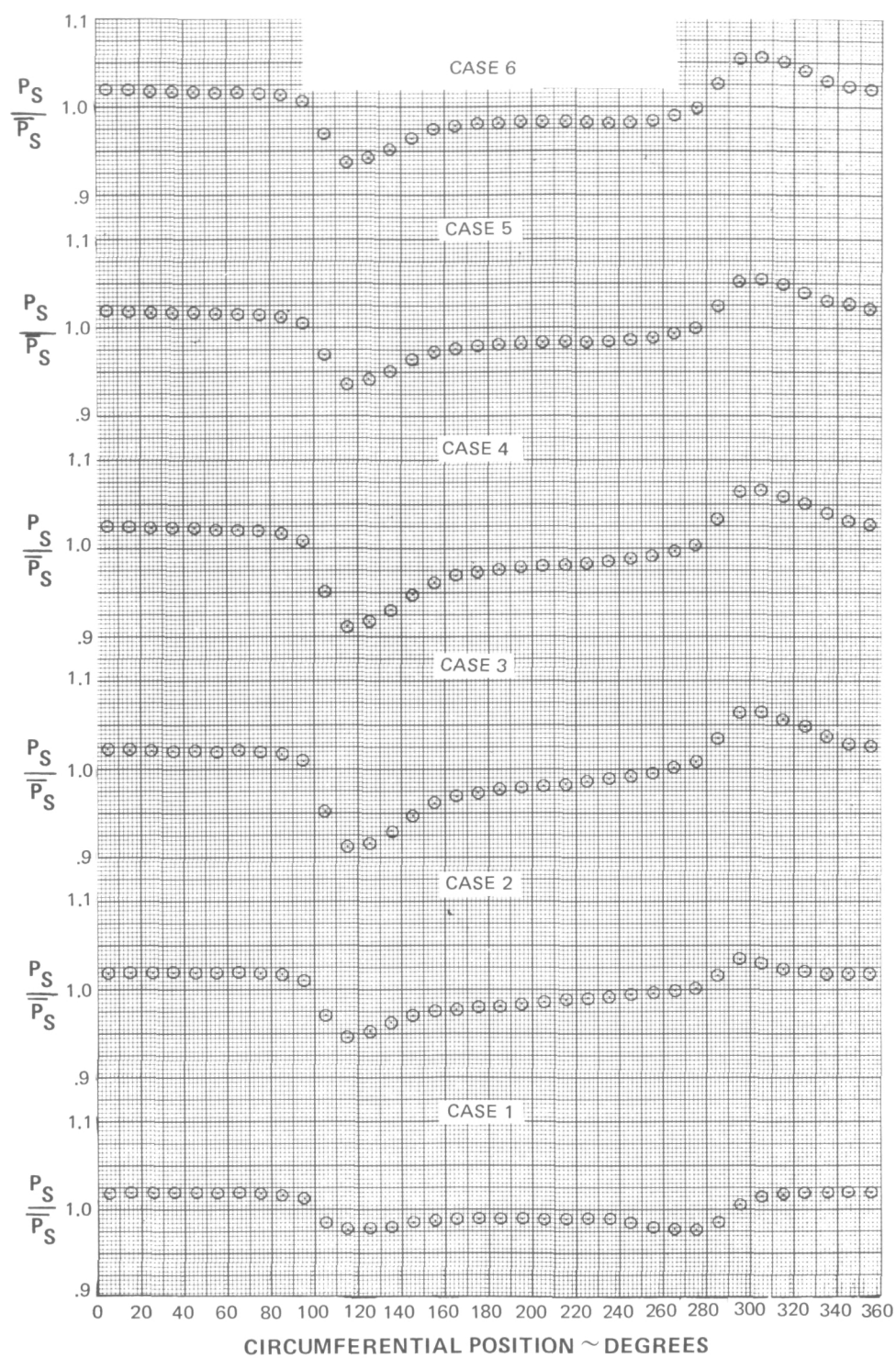


Figure 10o Station 2.3 Static Pressure Distortion

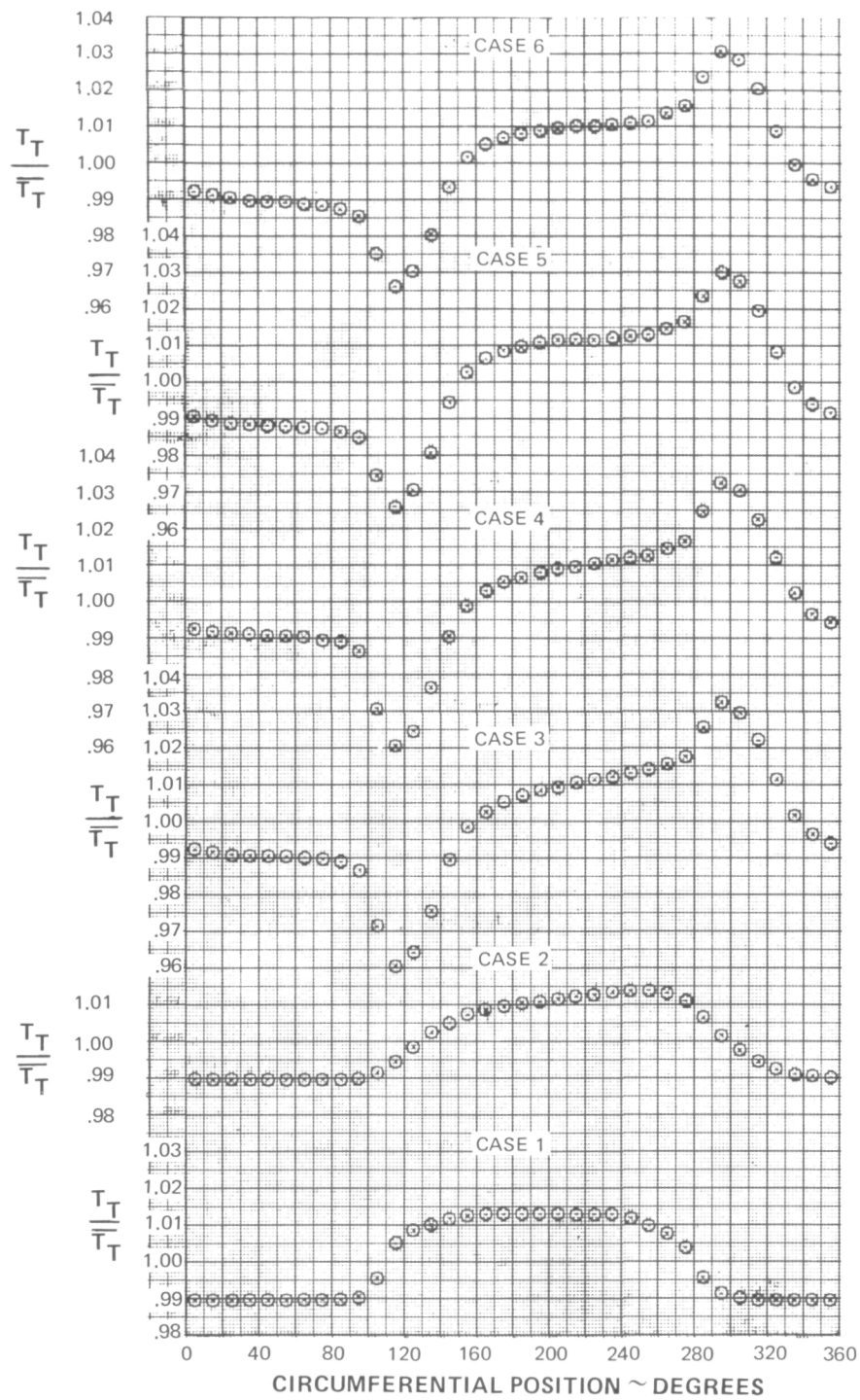


Figure 10p Station 2.3 Total Temperature Distortion

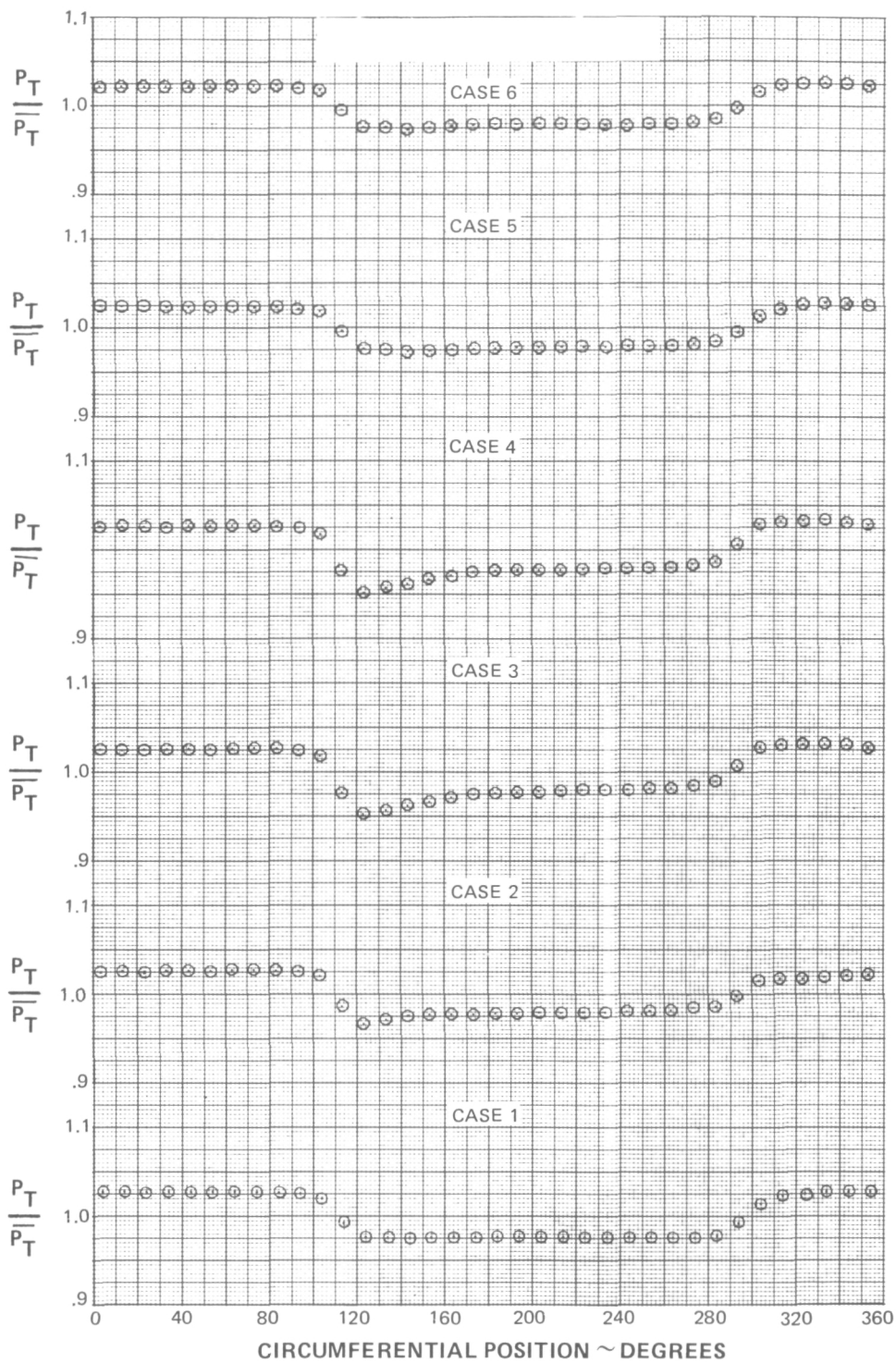


Figure 10q Station 2.6 Total Pressure Distortion

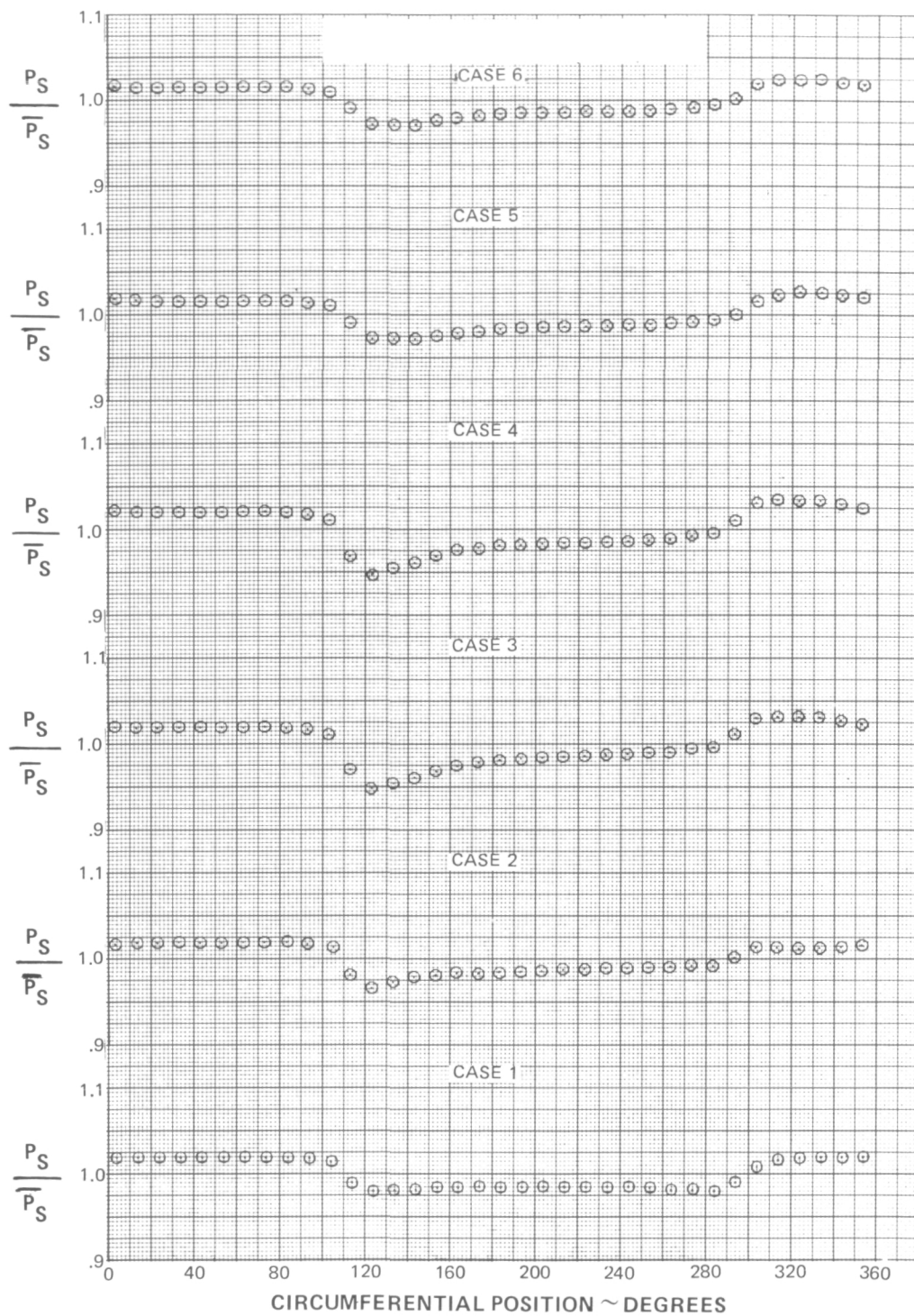


Figure 10r Station 2.6 Static Pressure Distortion

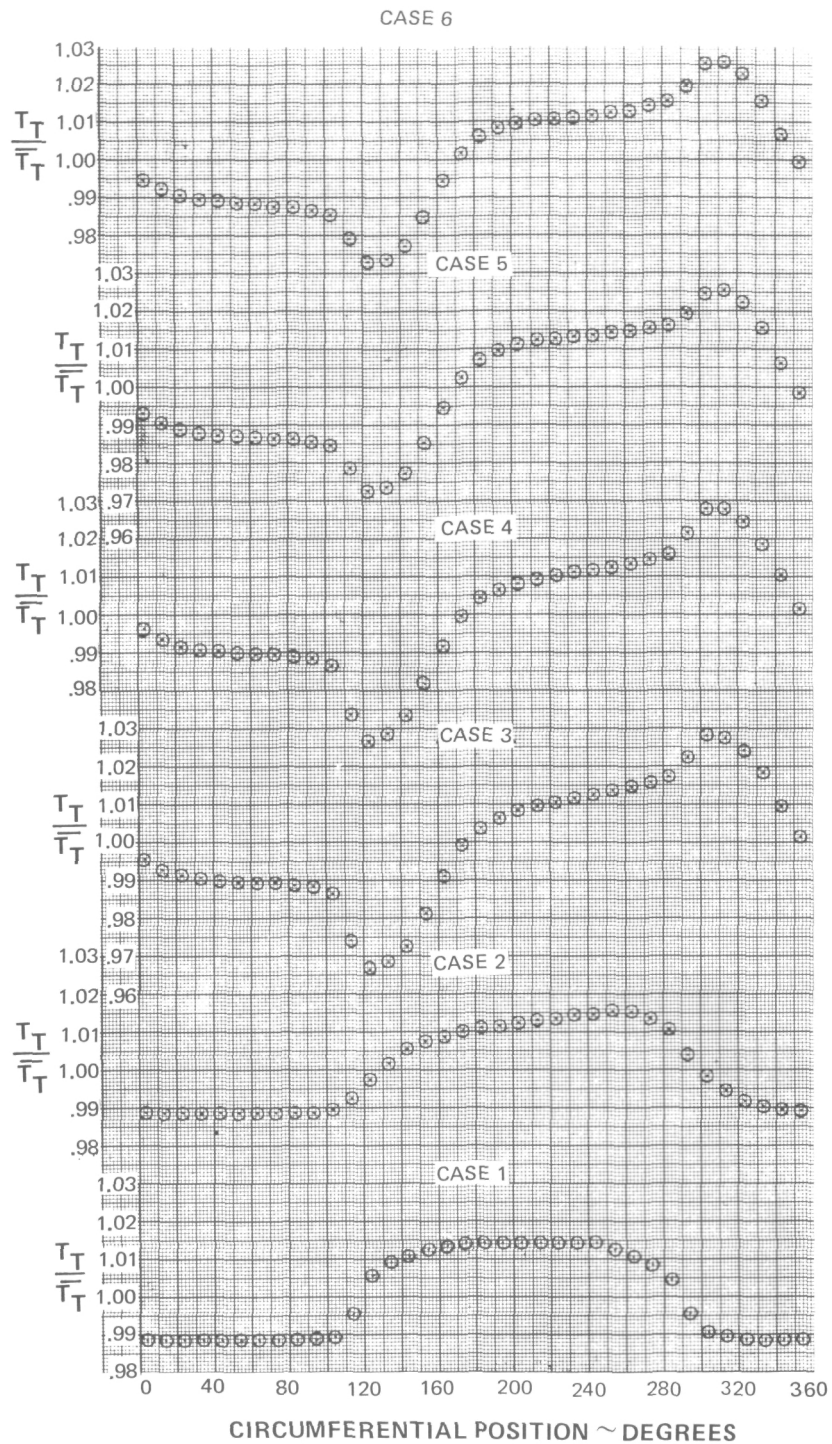


Figure 10s Station 2.6 Total Temperature Distortion

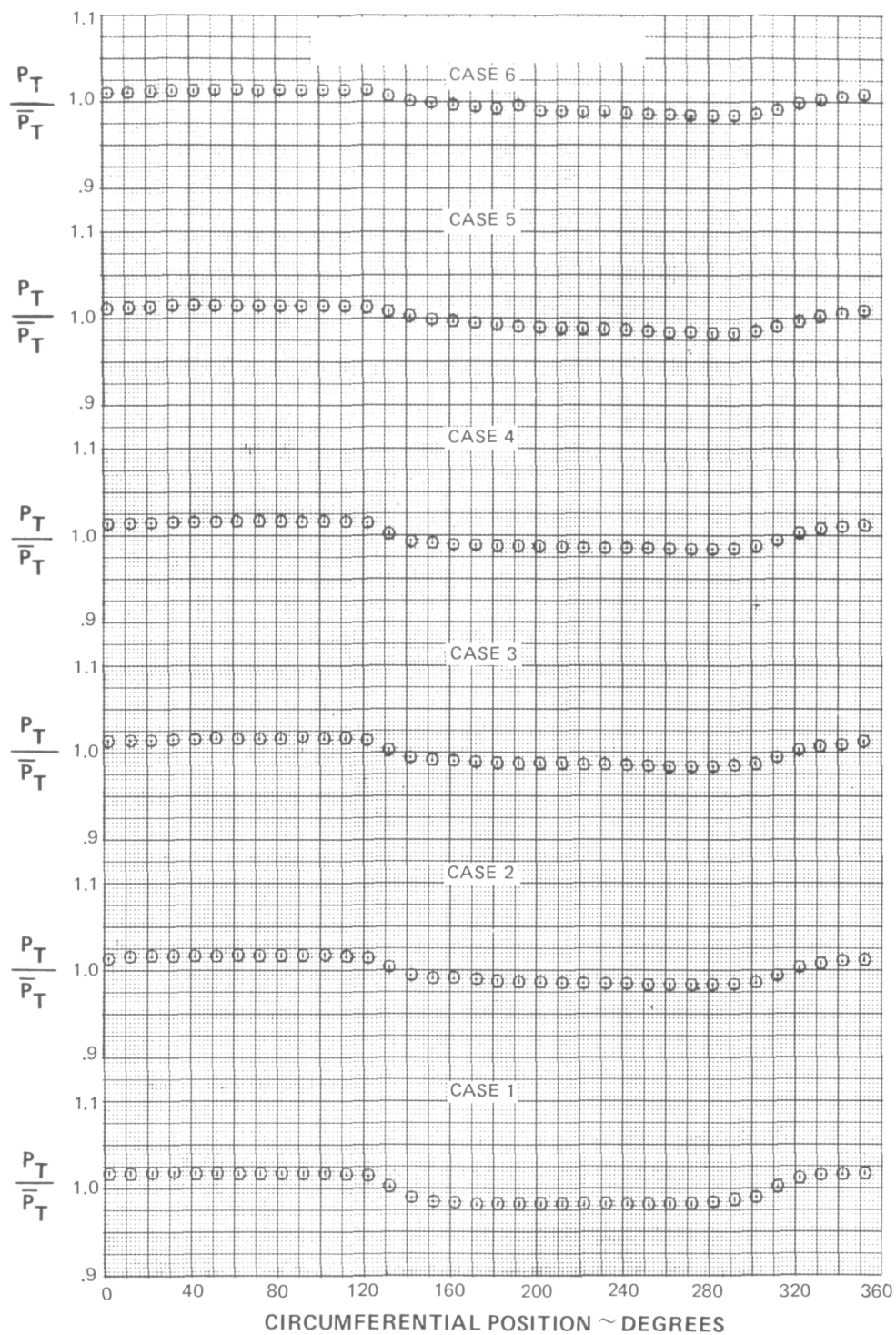


Figure 10t Station 3.0 Total Pressure Distortion

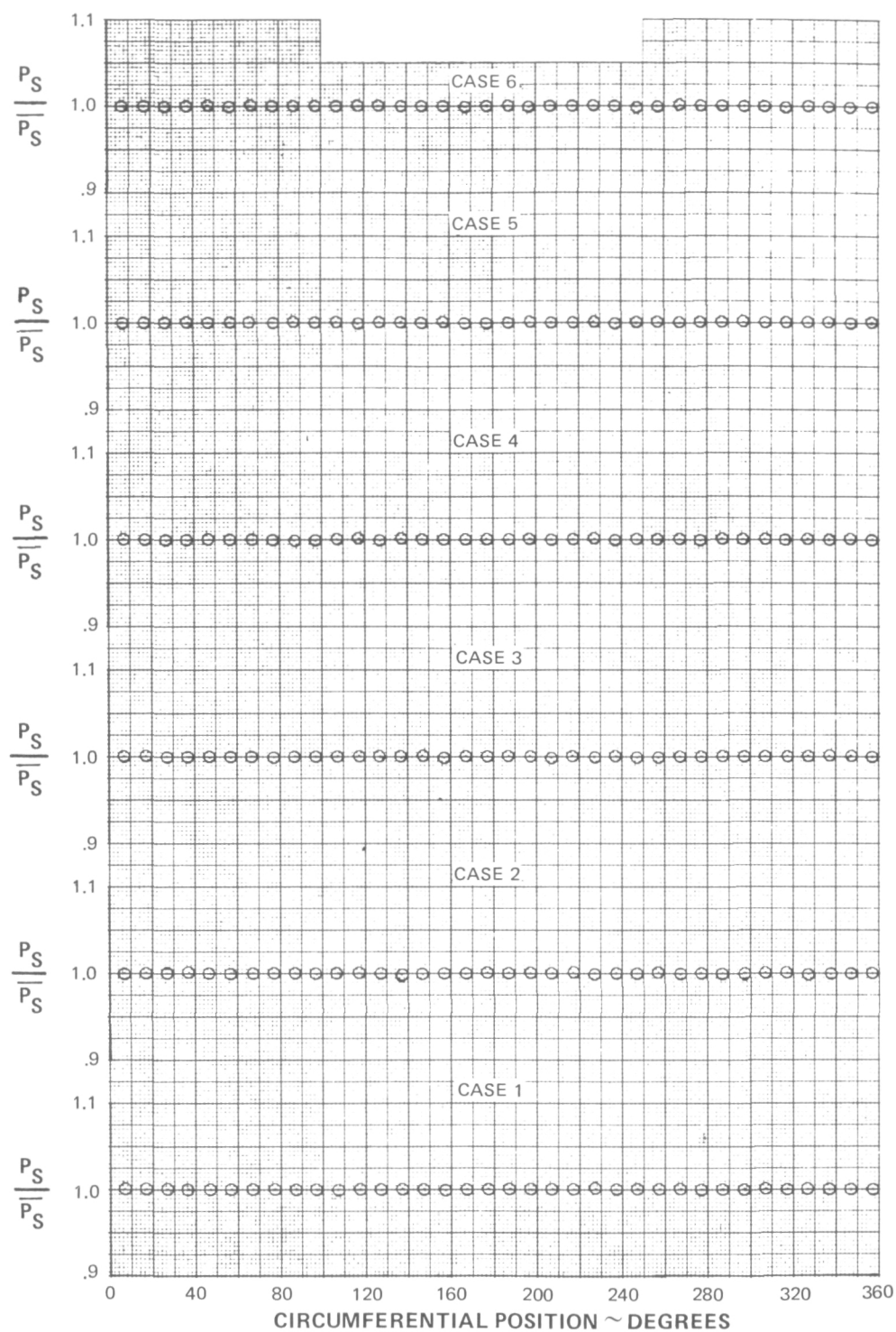


Figure 10u Station 3.0 Static Pressure Distortion

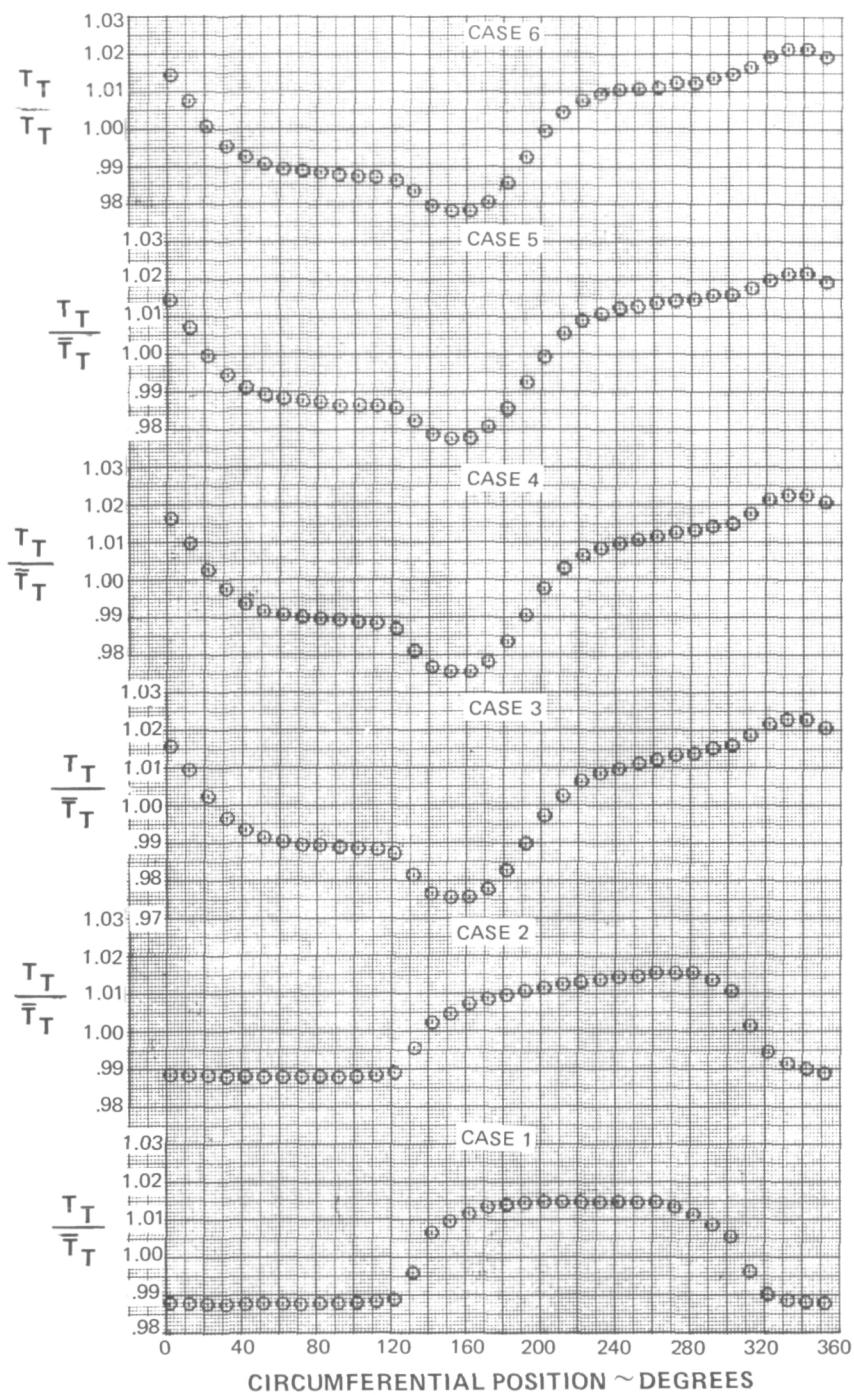


Figure 10v Station 3.0 Total Temperature Distortion

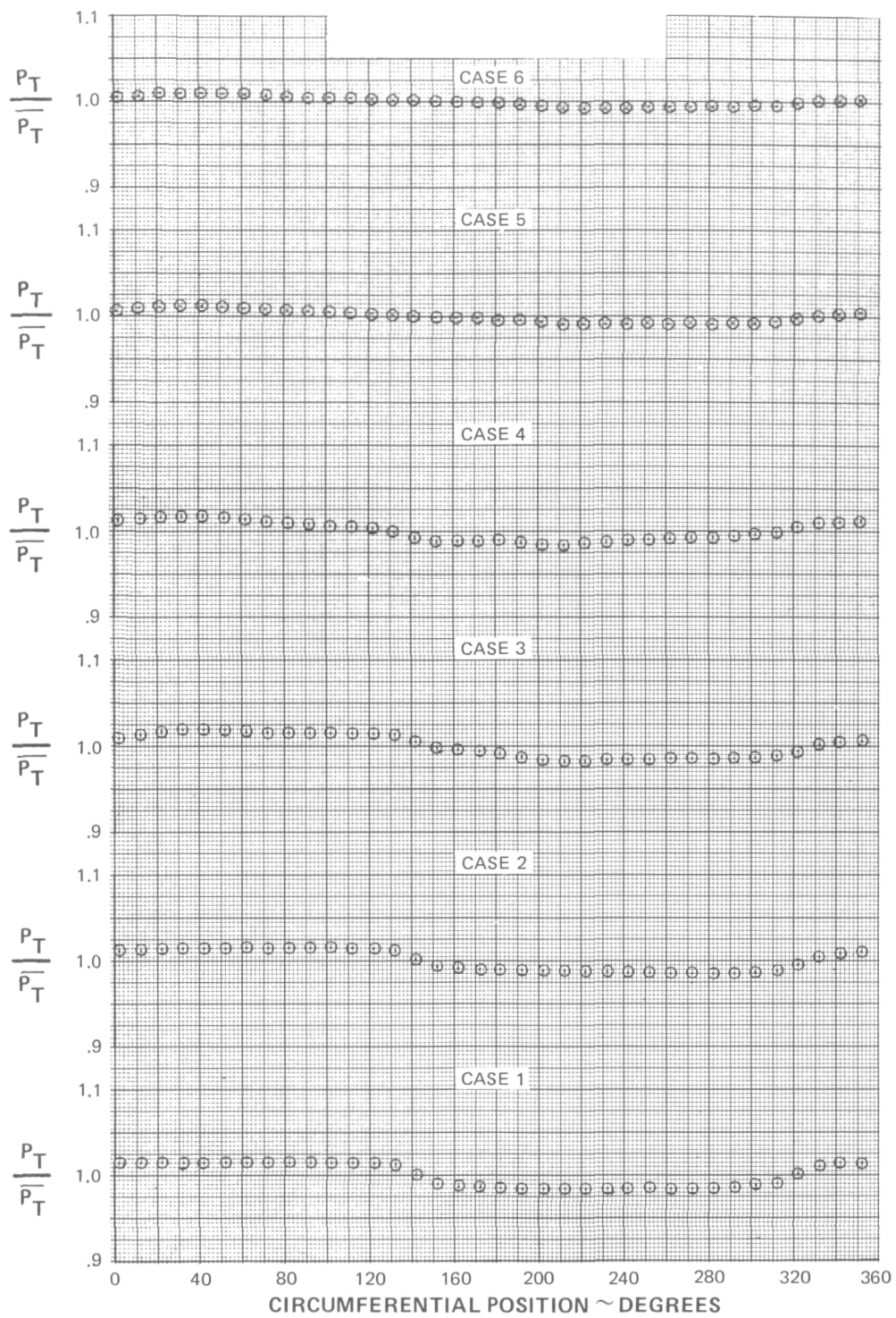


Figure 10w Station 3.12 Total Pressure Distortion

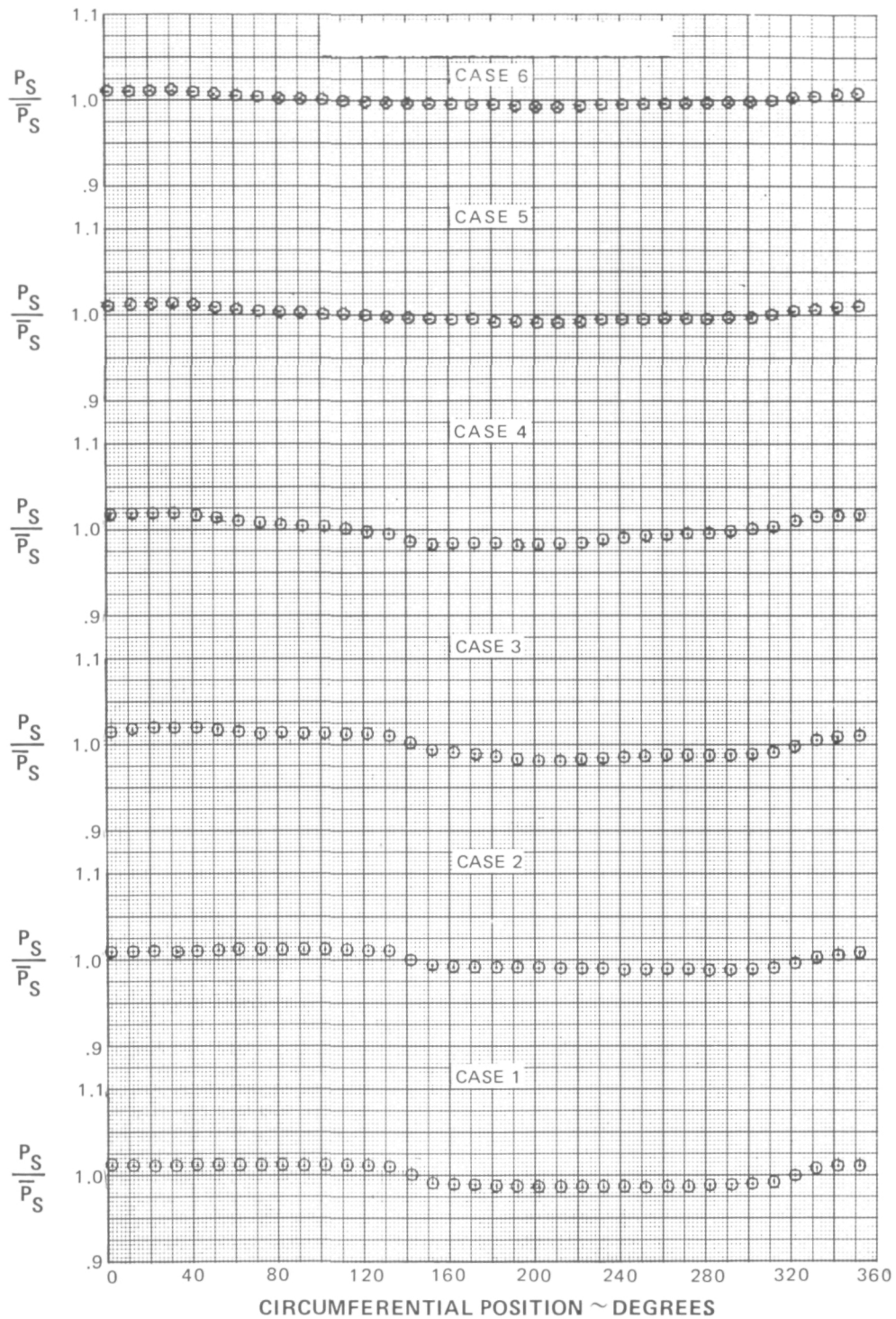


Figure 10x Station 3.12 Static Pressure Distortion

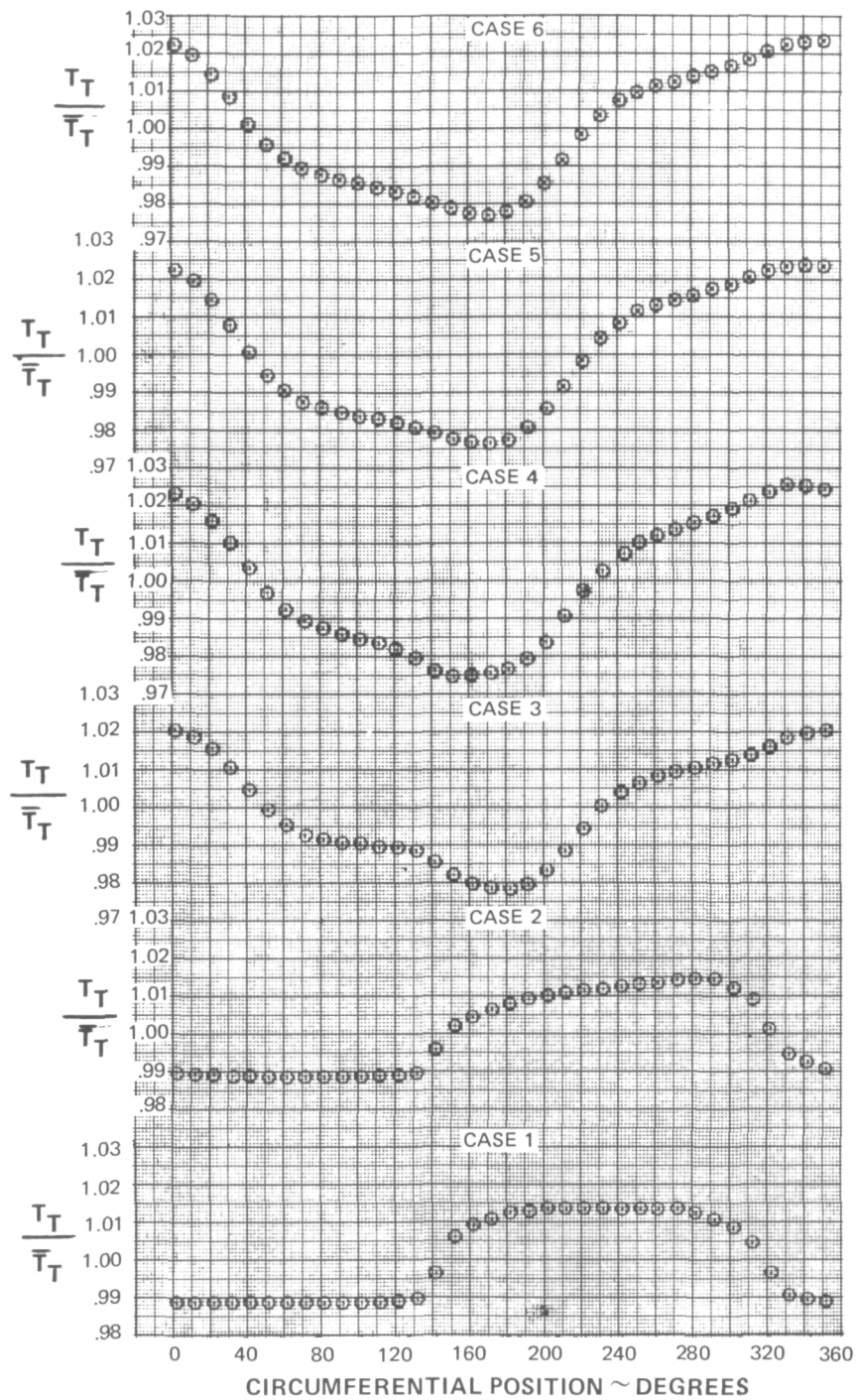


Figure 10y Station 3.12 Total Temperature Distortion

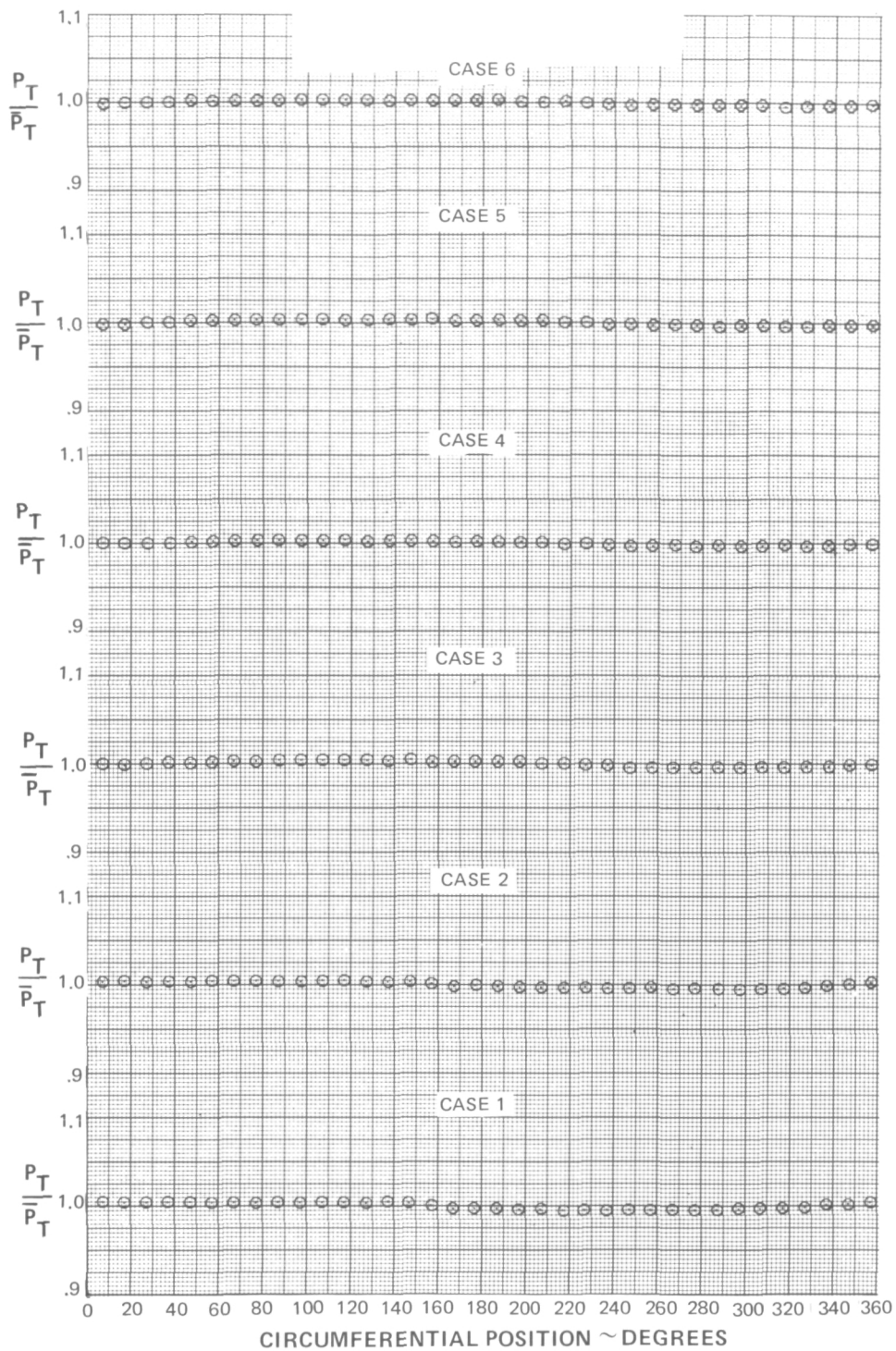


Figure 10z Station 4.0 Total Pressure Distortion

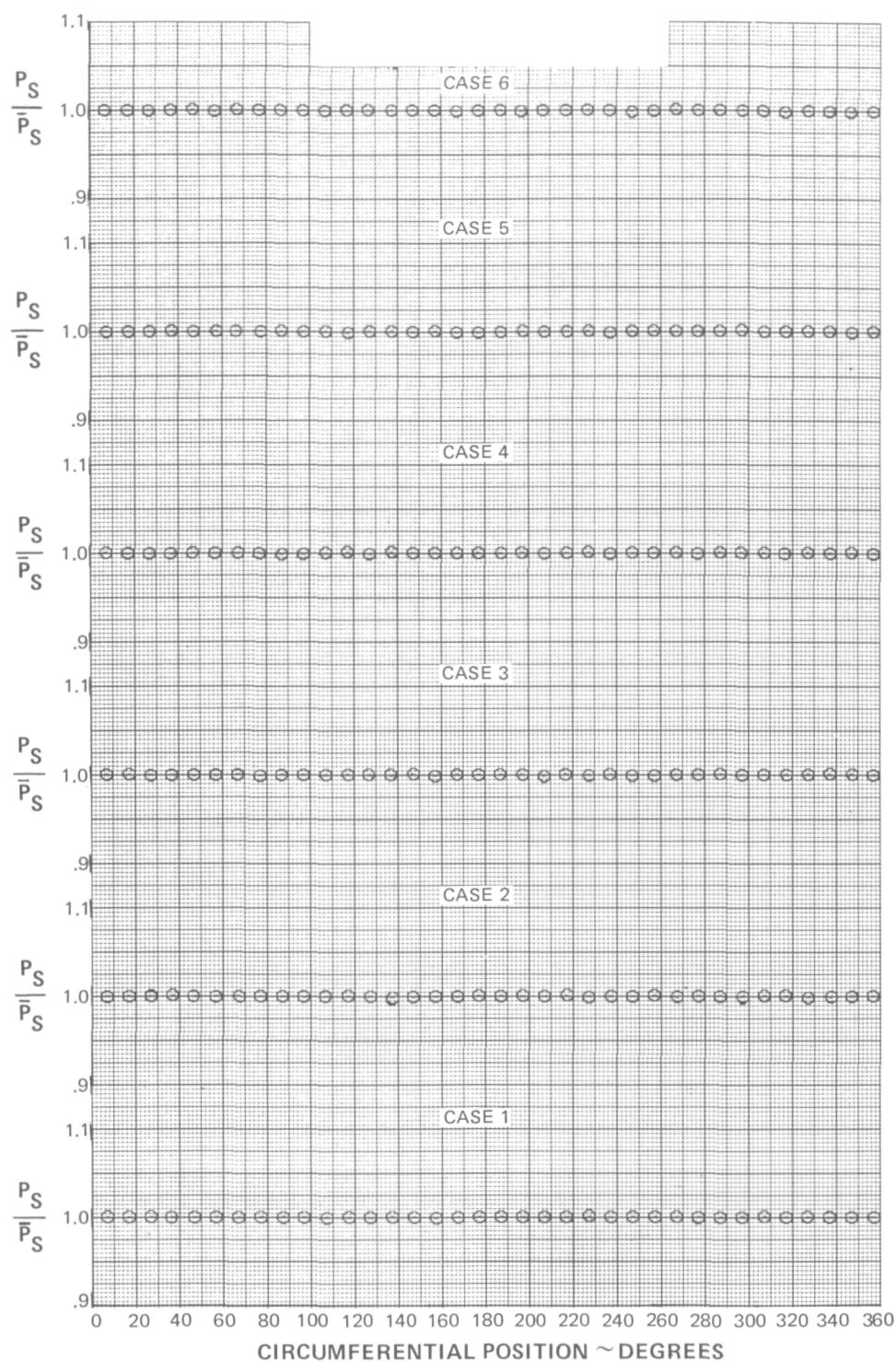


Figure 10aa Station 4.0 Static Pressure Distortion

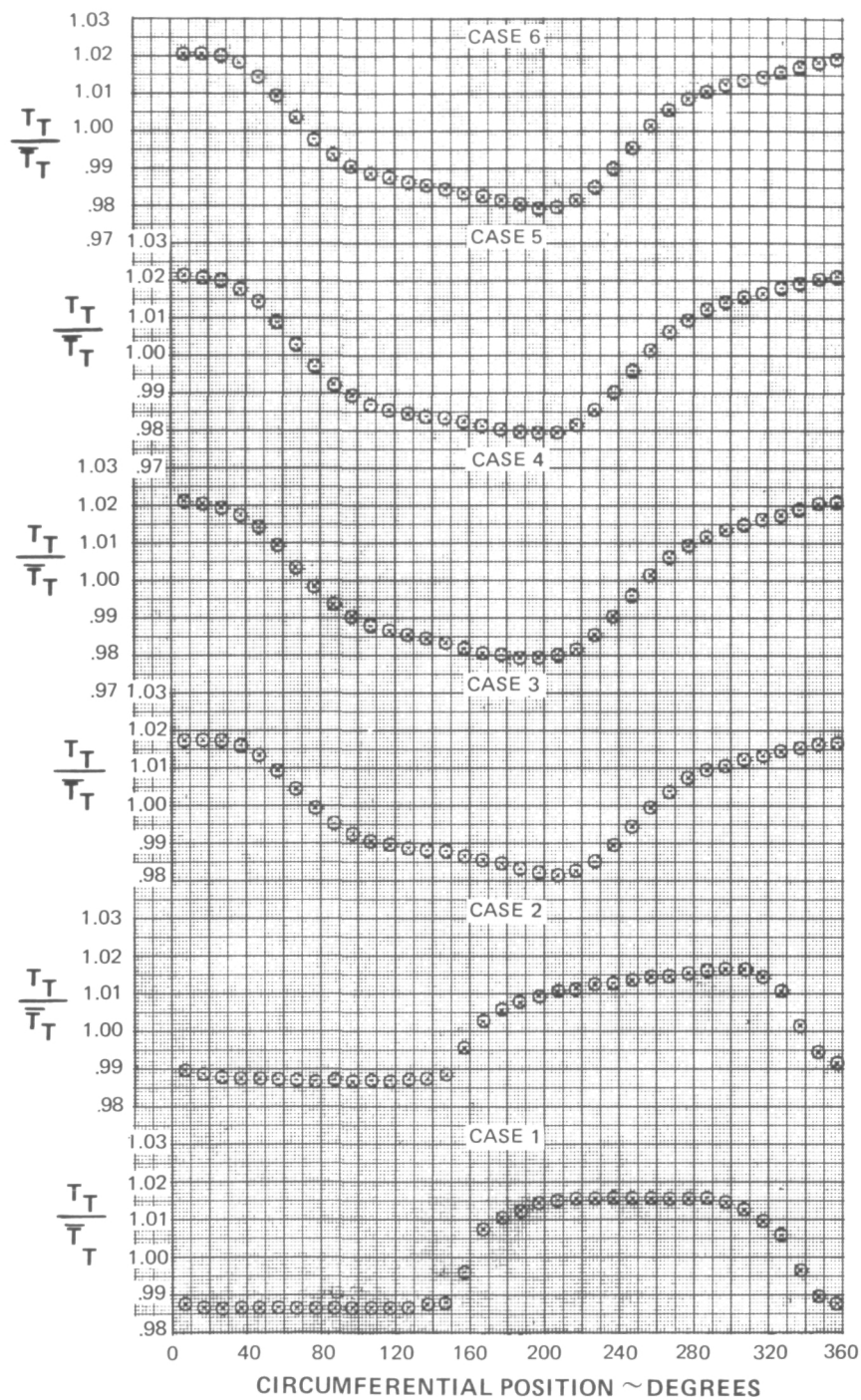


Figure 10bb Station 4.0 Total Temperature Distortion

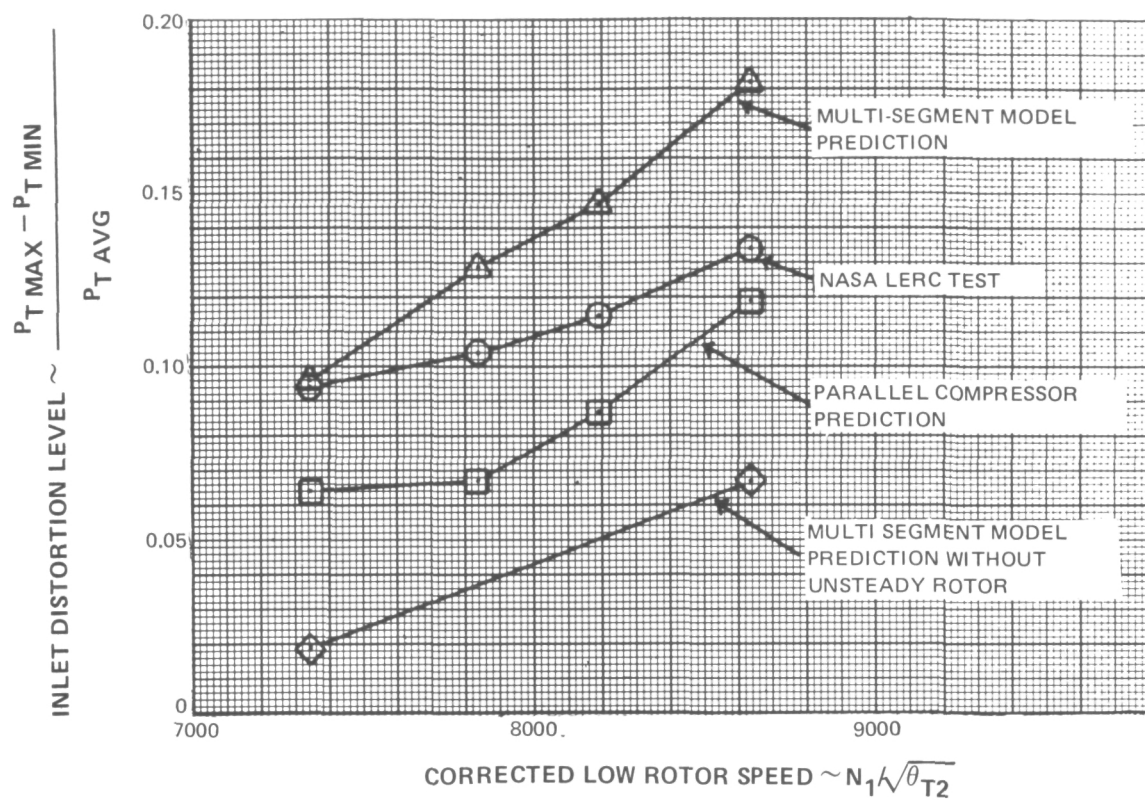


Figure 11 Influence of Unsteady Rotor Loss on Model Prediction at $RNI = 0.5$

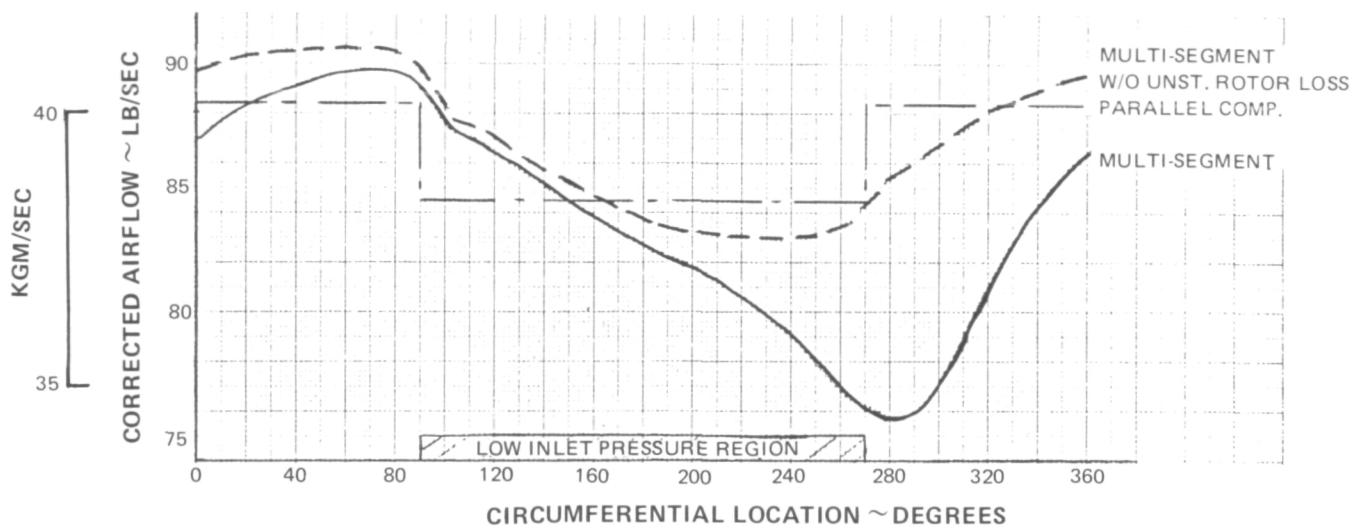


Figure 12 Circumferential Engine Core Mass Flow Distribution at Stall –
8200 RPM, RNI = 1.0

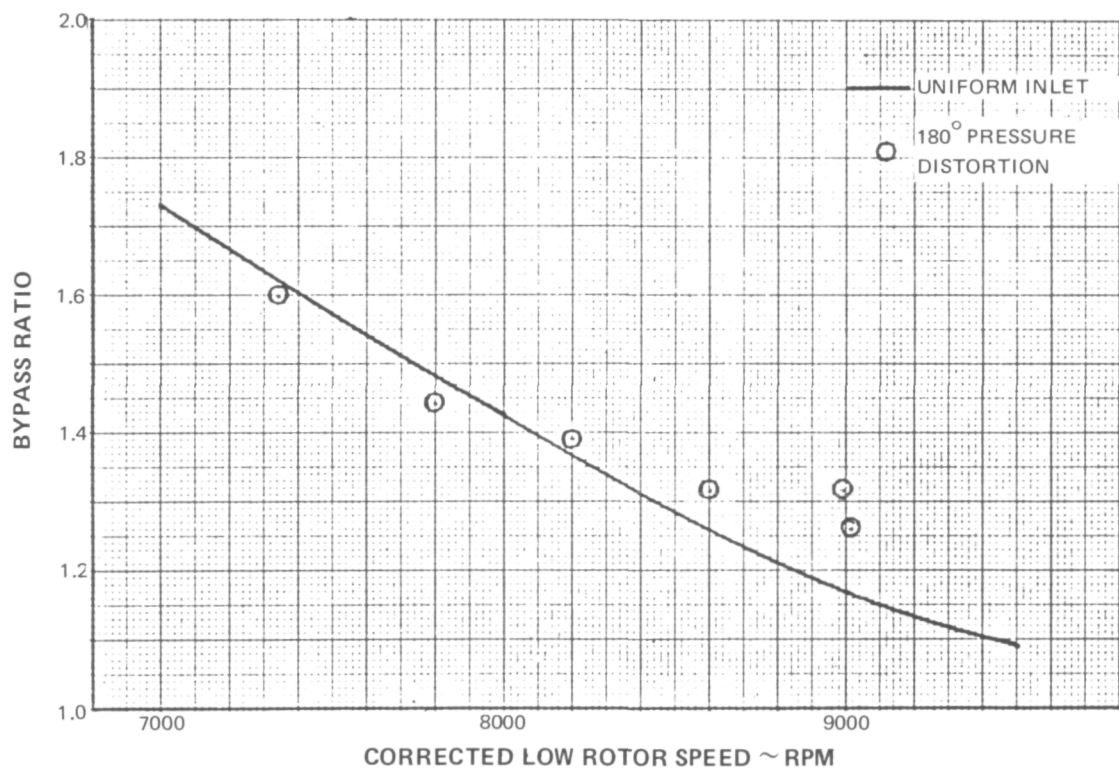


Figure 13 Inlet Distortion Effect on NASA Engine Bypass Ratio,
RNI = 0.5

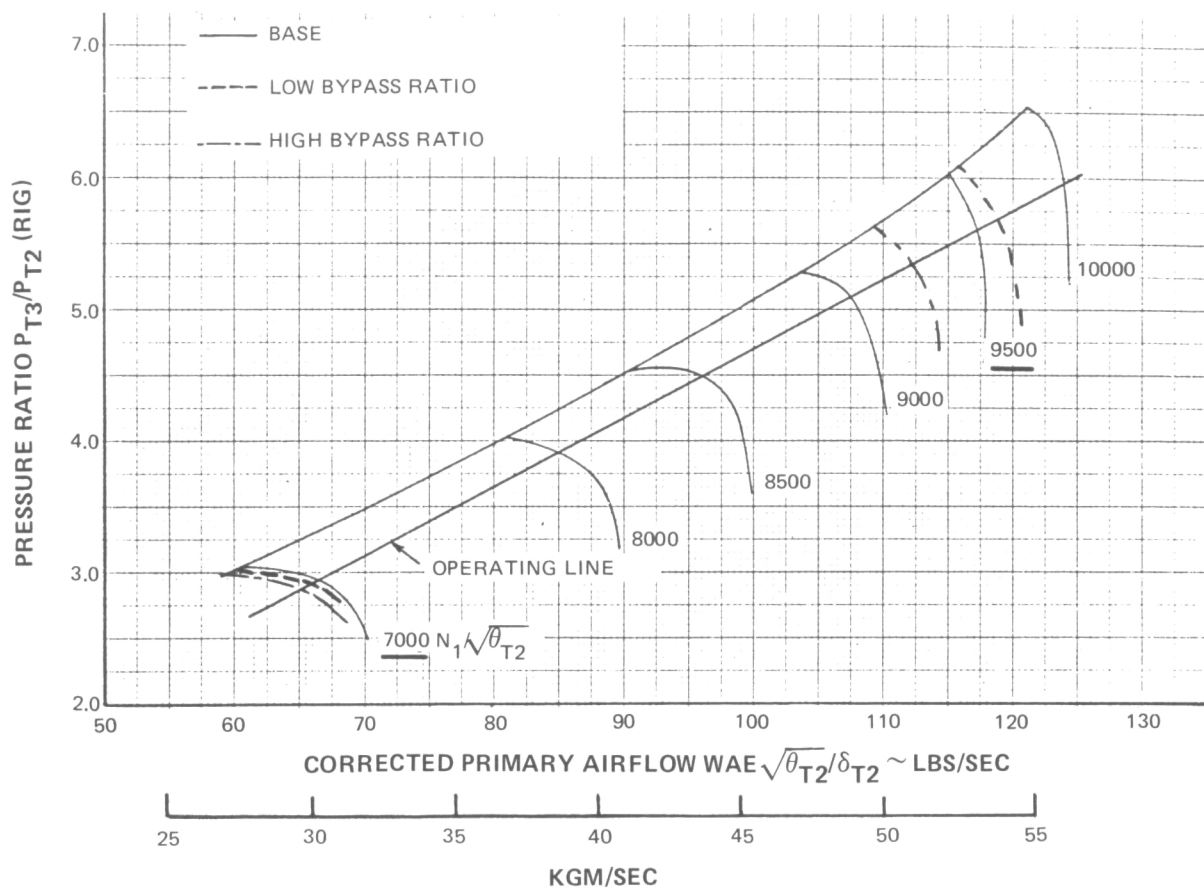


Figure 14 Bypass Ratio Effect on TF30 P-3 Low-Pressure Compressor Rig Performance

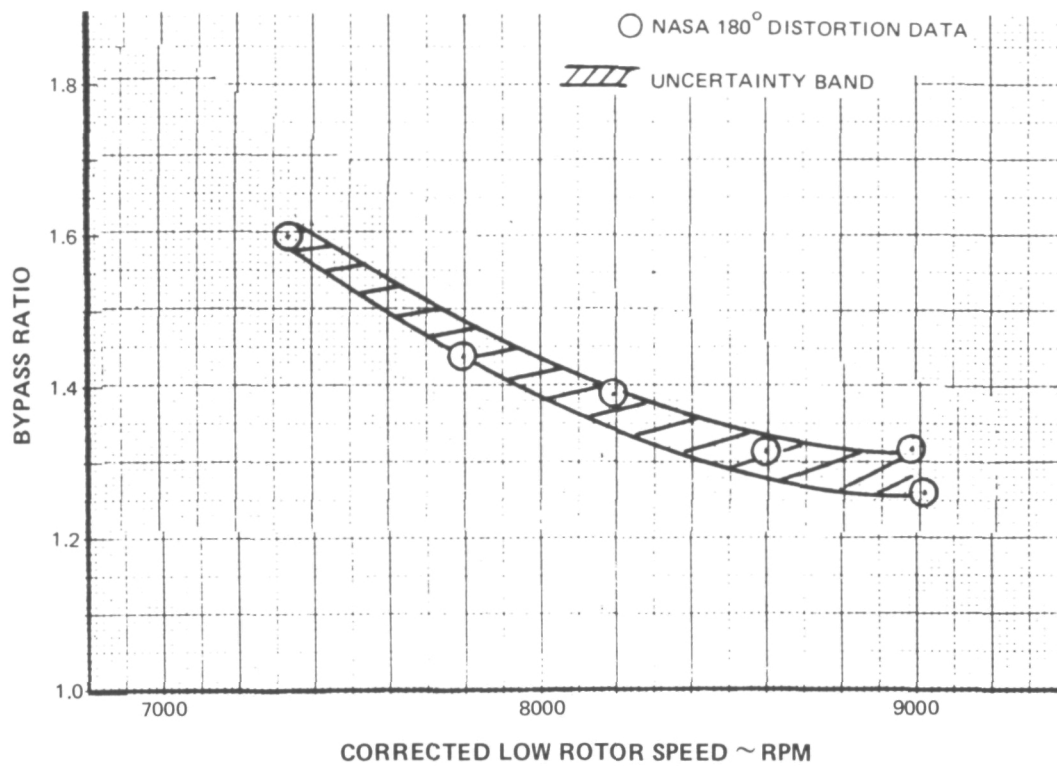


Figure 15 Uncertainty in NASA Engine Bypass Ratio Calculated from Critical Amplitude 180-degree Pressure Distortion Data, $RNI = 0.5$

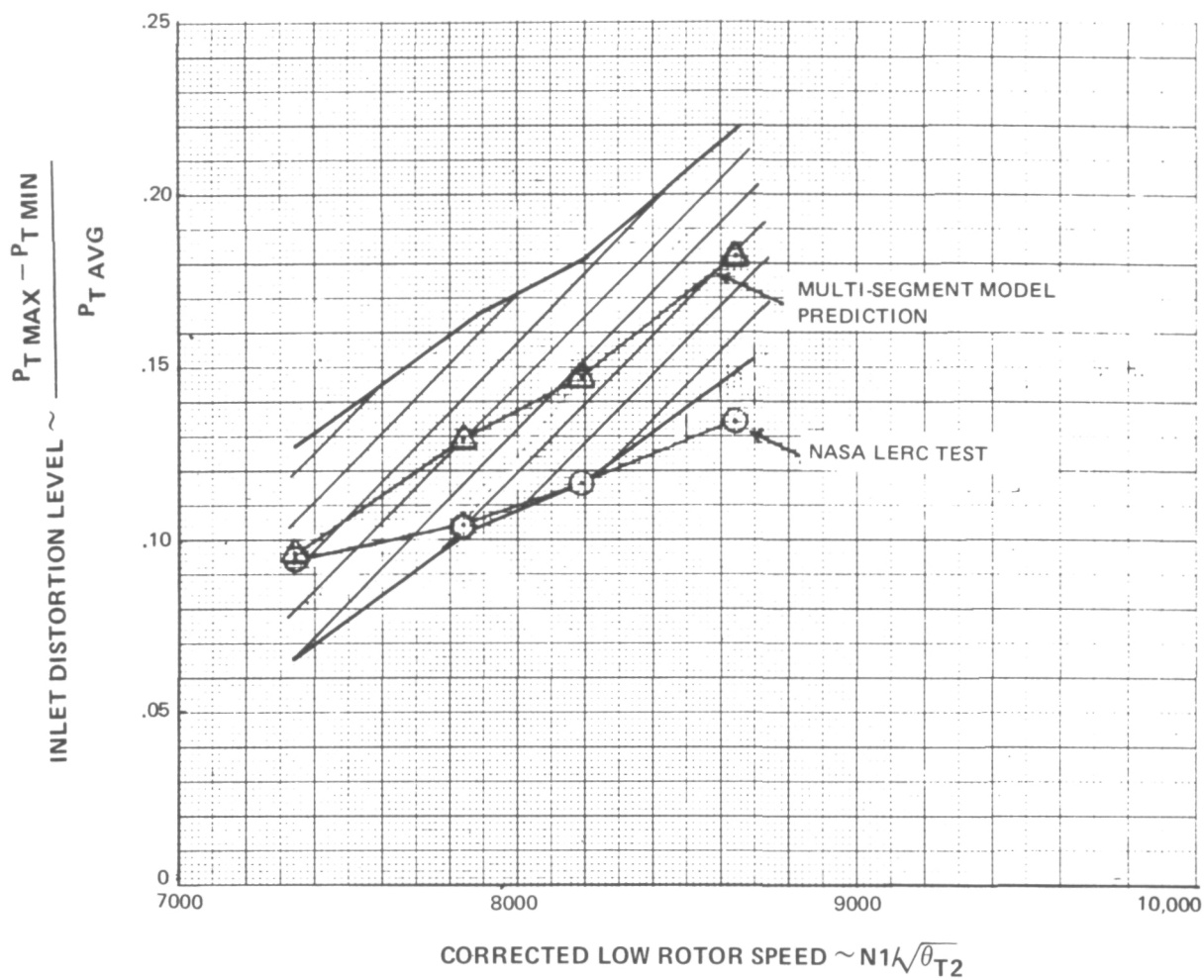


Figure 16 Effect of $\pm 1\%$ Error Band in Calculated NASA Engine Bypass Ratio on Critical Distortion Amplitude

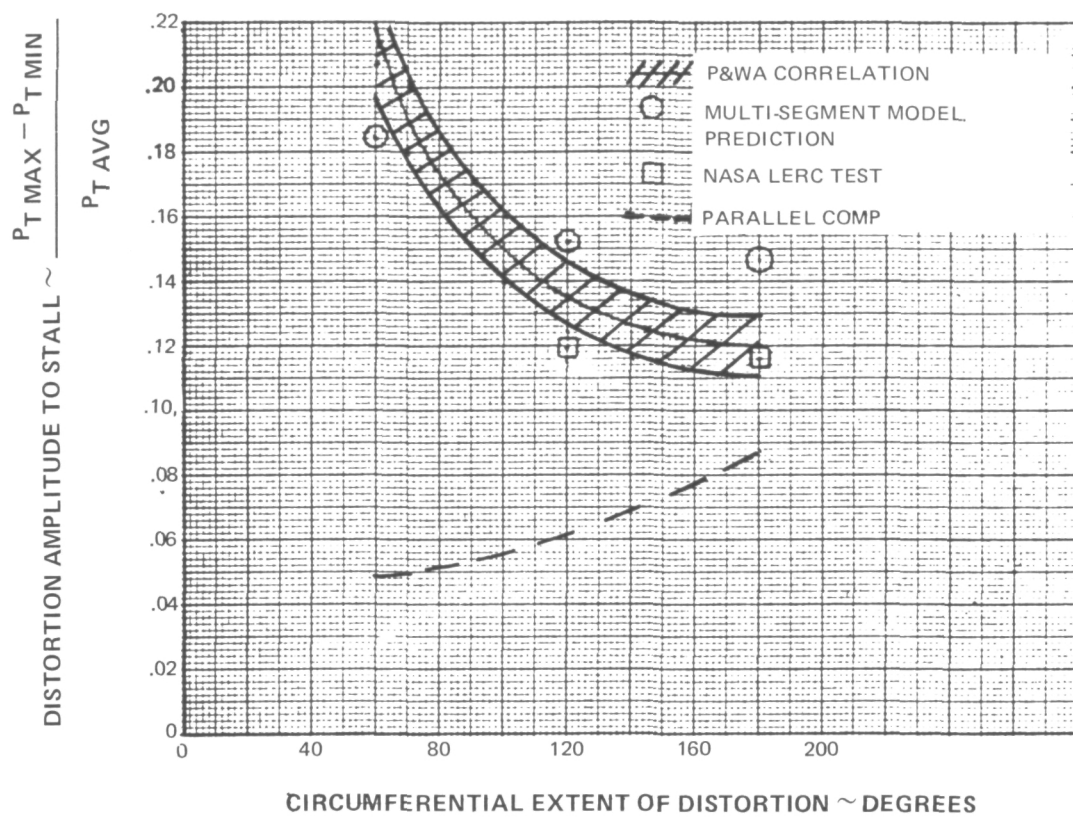


Figure 17(a) Influence of Circumferential Extent of Total Pressure Distortion on Critical Distortion Amplitude $N_1/\sqrt{\theta_{T2}} = 8200 \text{ RPM}$

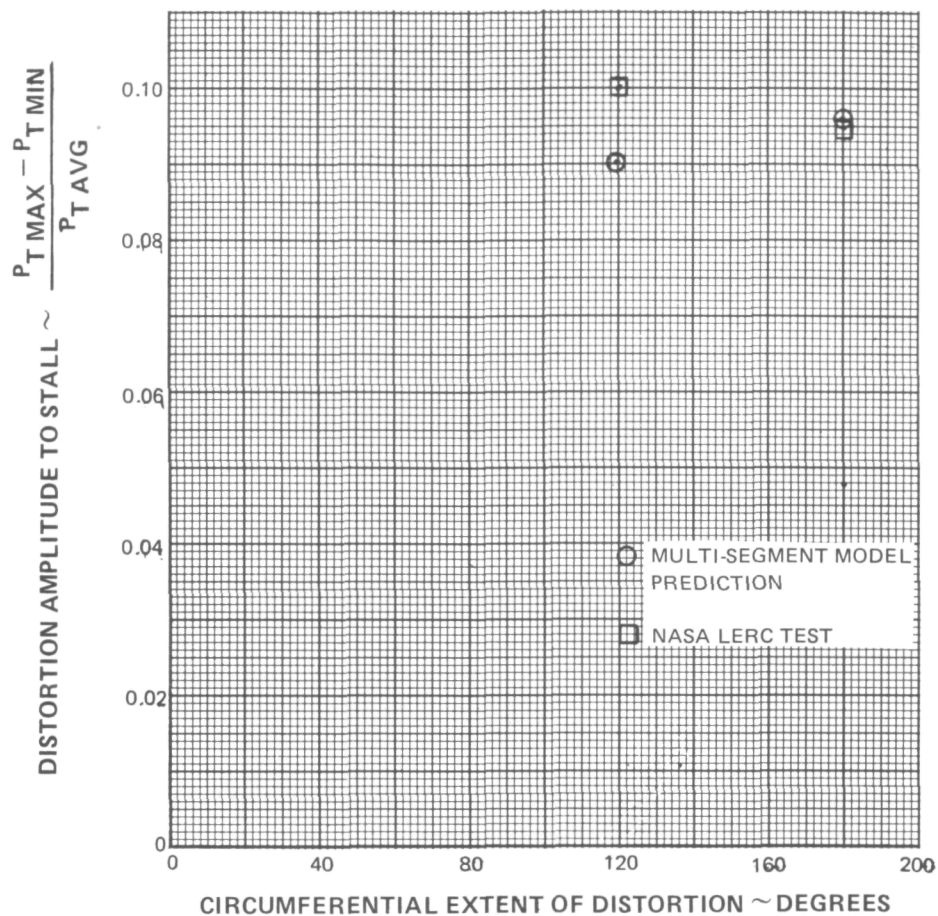


Figure 17 (b) Influence of Circumferential Extent of Total Pressure Distortion on Critical Distortion Amplitude $N_1/\sqrt{\theta_{T2}} = 7400 \text{ RPM}$

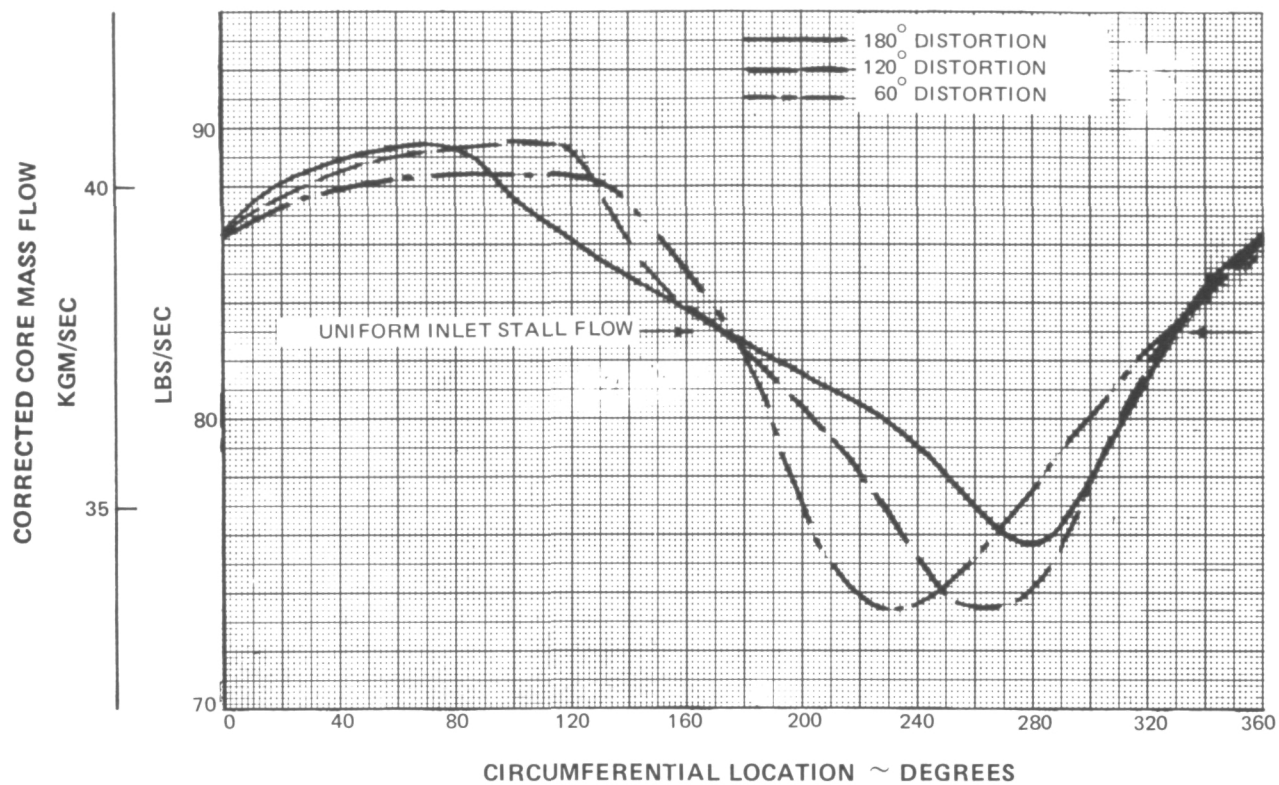


Figure 18 Critical Extent of Low Flow Region for Stall, $N_1/\sqrt{\theta_{T2}} = 8200$ RPM, $RNI = 1.0$

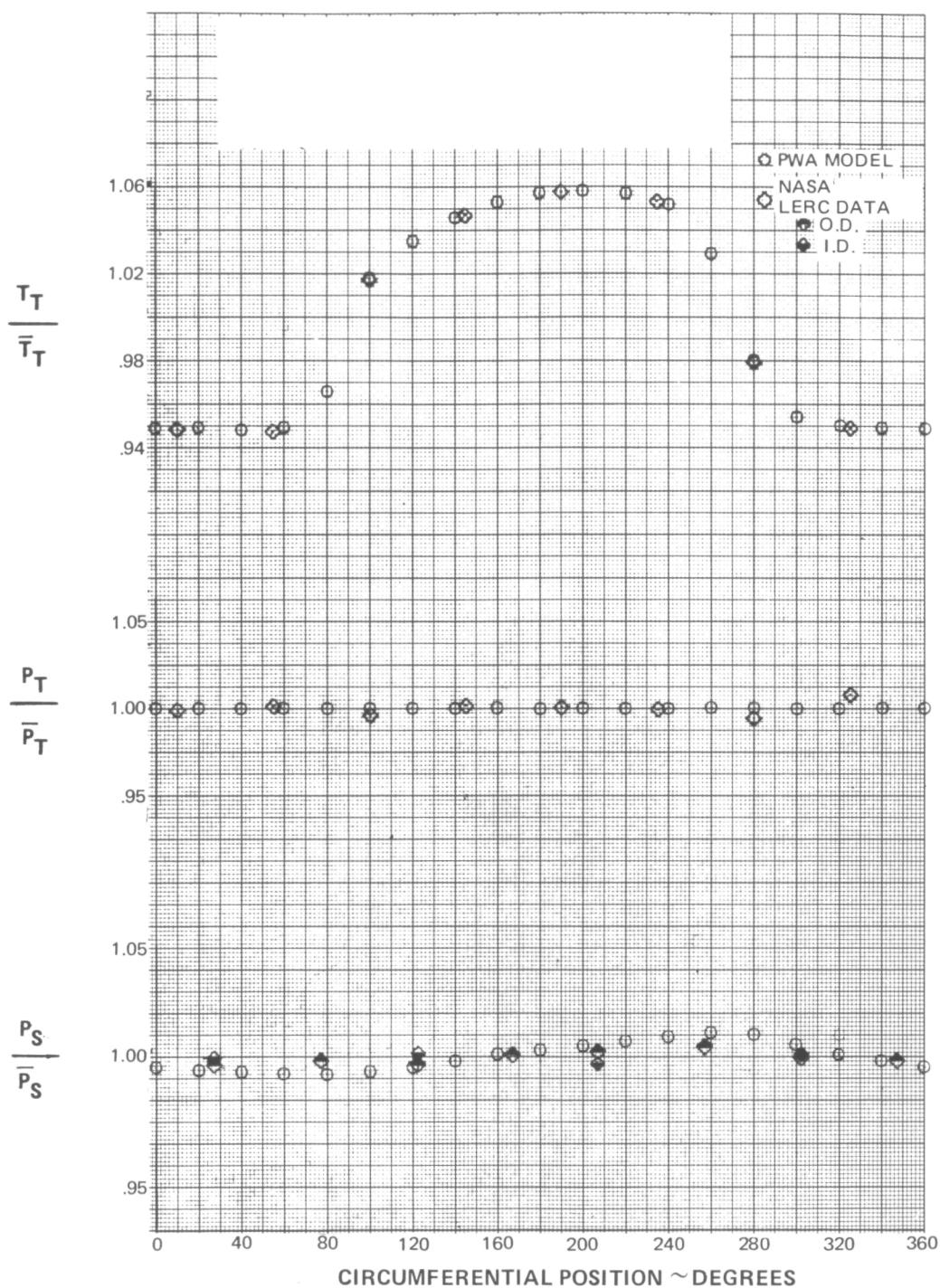


Figure 19a Circumferential Variation of Predicted and Measured Flow Properties with 180-degree Temperature Distortion ($\Delta T/T = 0.11$), $N_1/\sqrt{\theta_{T2}} = 7700$ RPM – Station 2.0

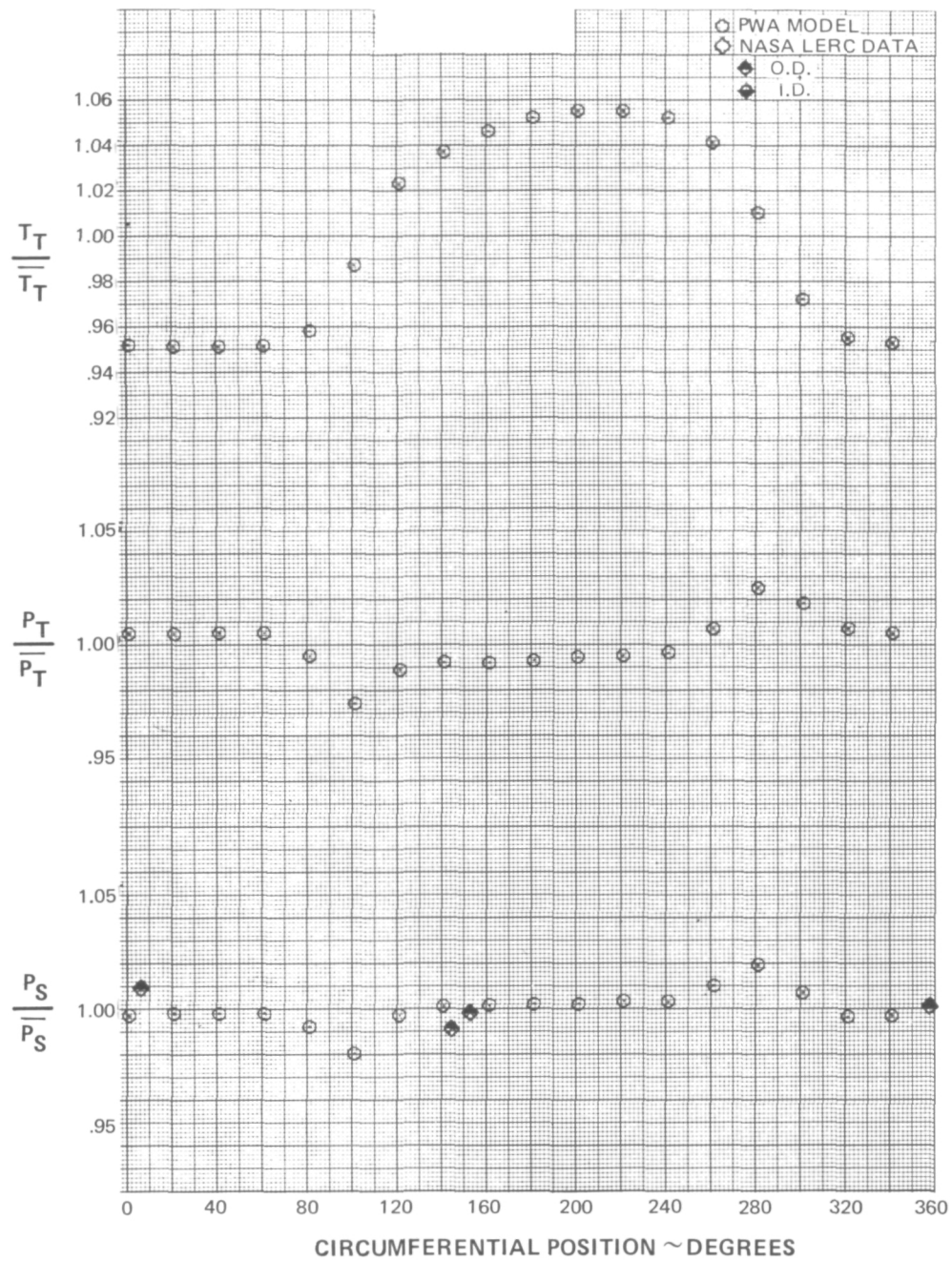


Figure 19b. Total Temperature Distortion ($\Delta T/T = 0.11$) – Station 2.1F

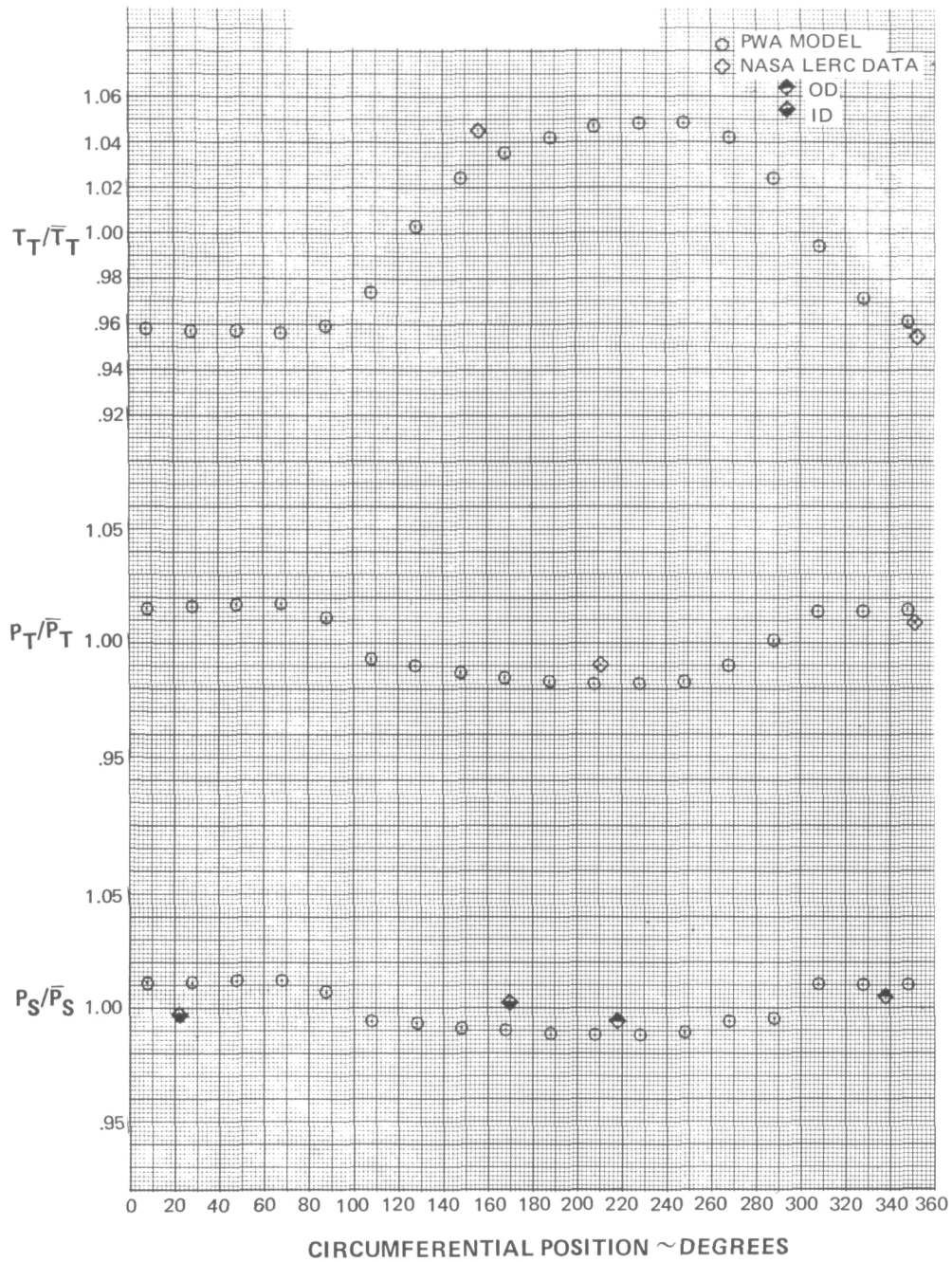


Figure 19c Total Temperature Distortion ($\Delta T/T = 0.11$) – Station 2.3F

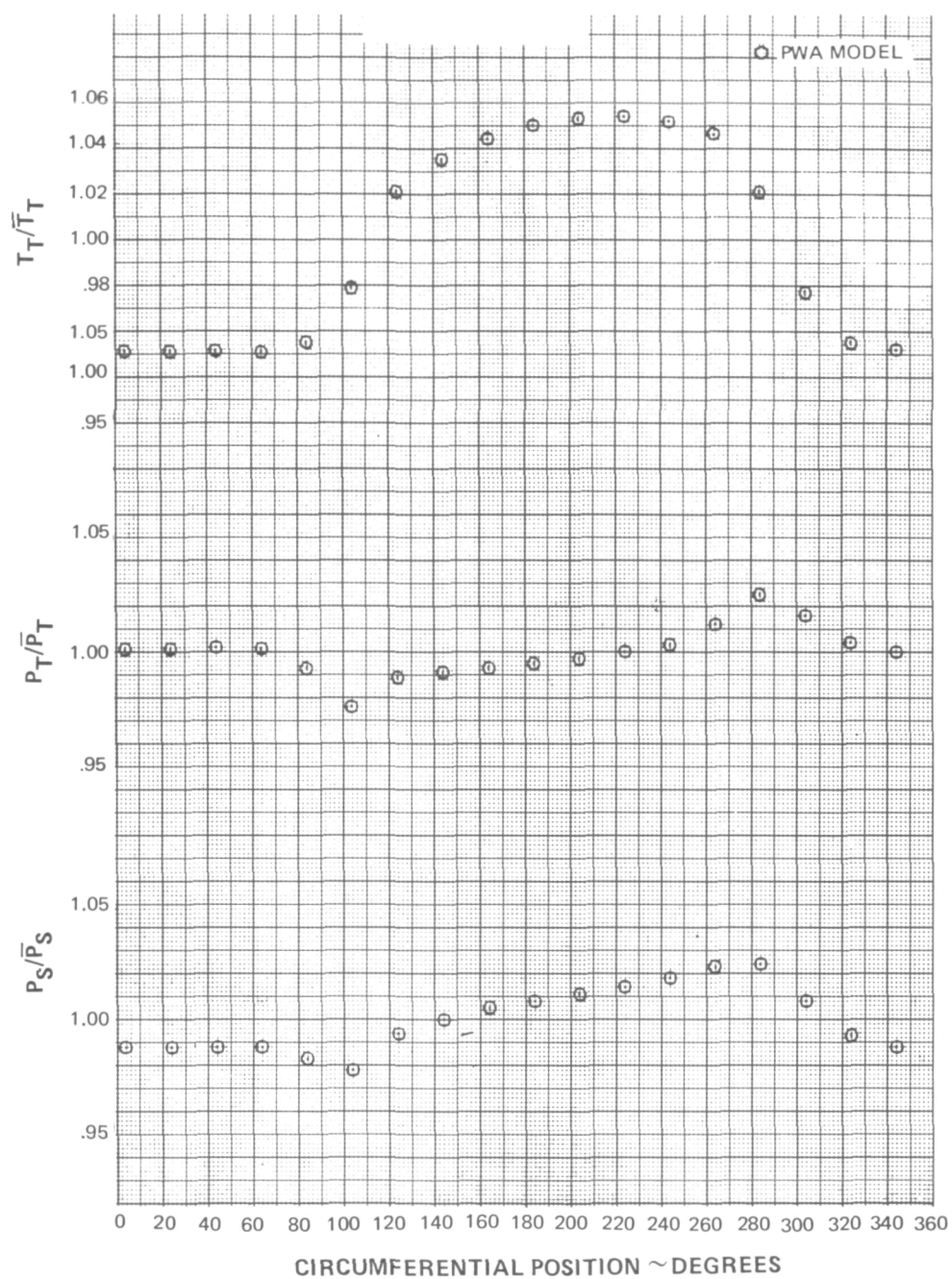


Figure 19d Total Temperature Distortion ($\Delta T/T = 0.11$) – Station 2.1

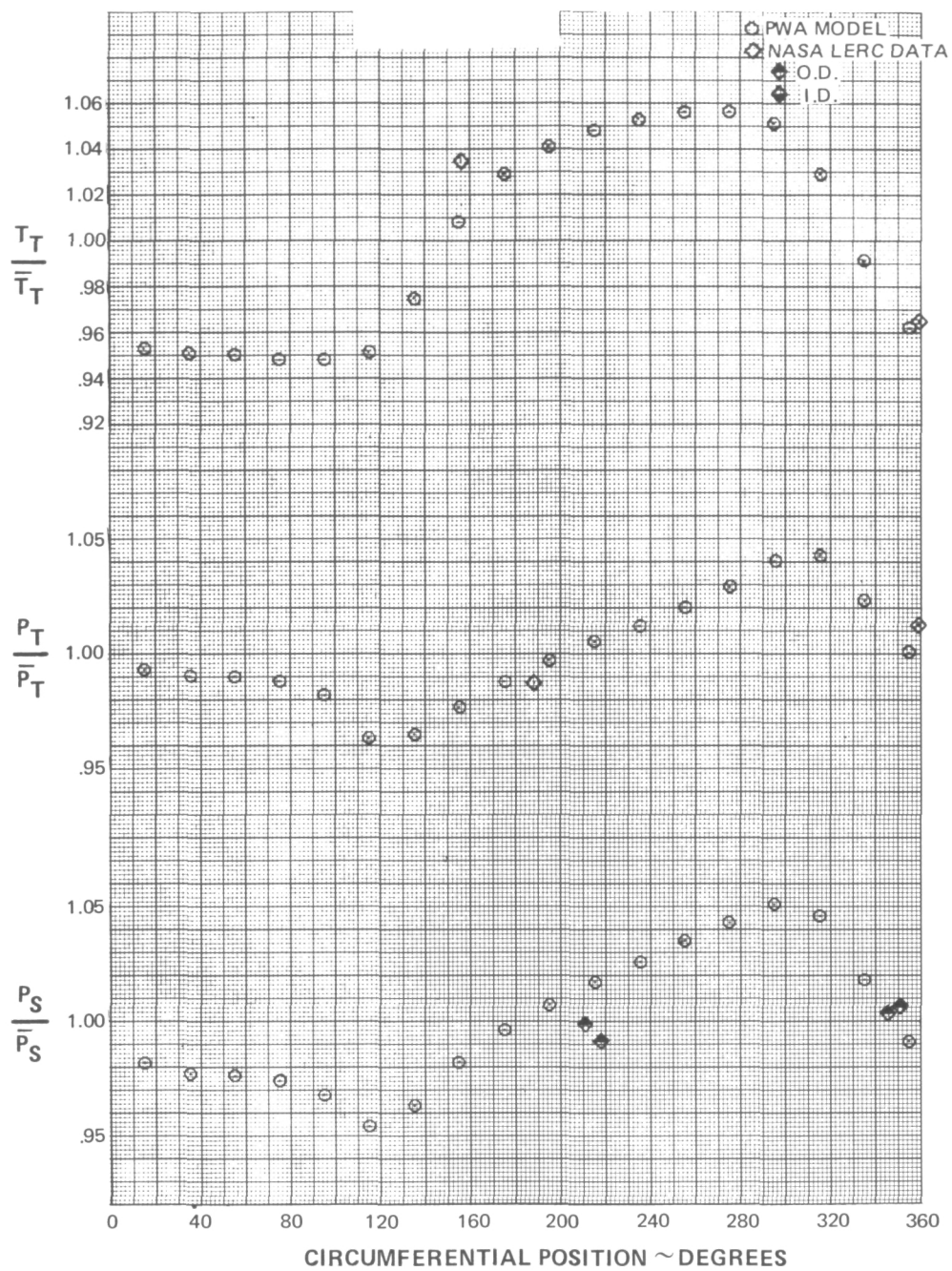


Figure 19e Total Temperature Distortion ($\Delta T/T = 0.11$) – Station 2.3

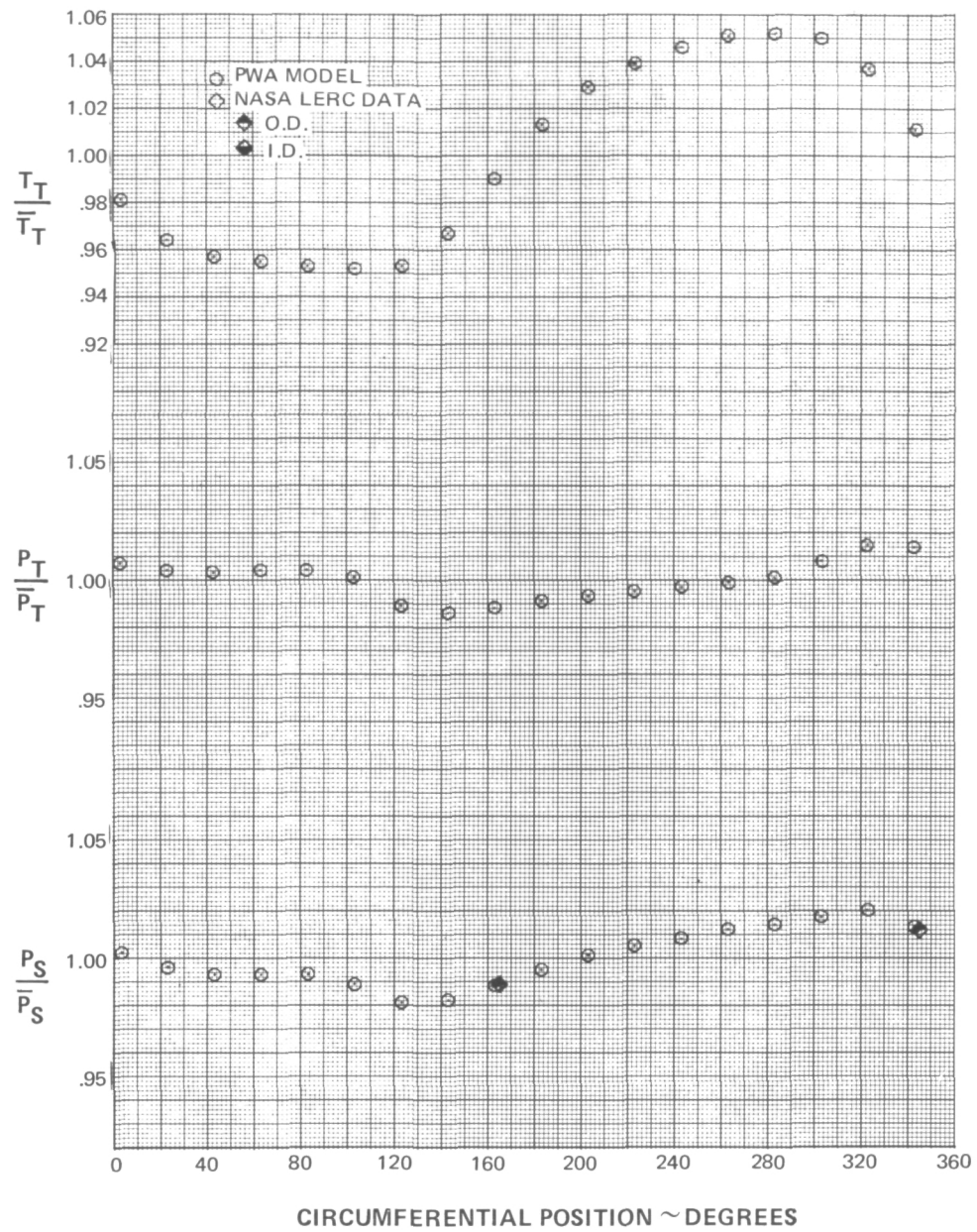


Figure 19f Total Temperature Distortion ($\Delta T/T = 0.11$) – Station 2.6

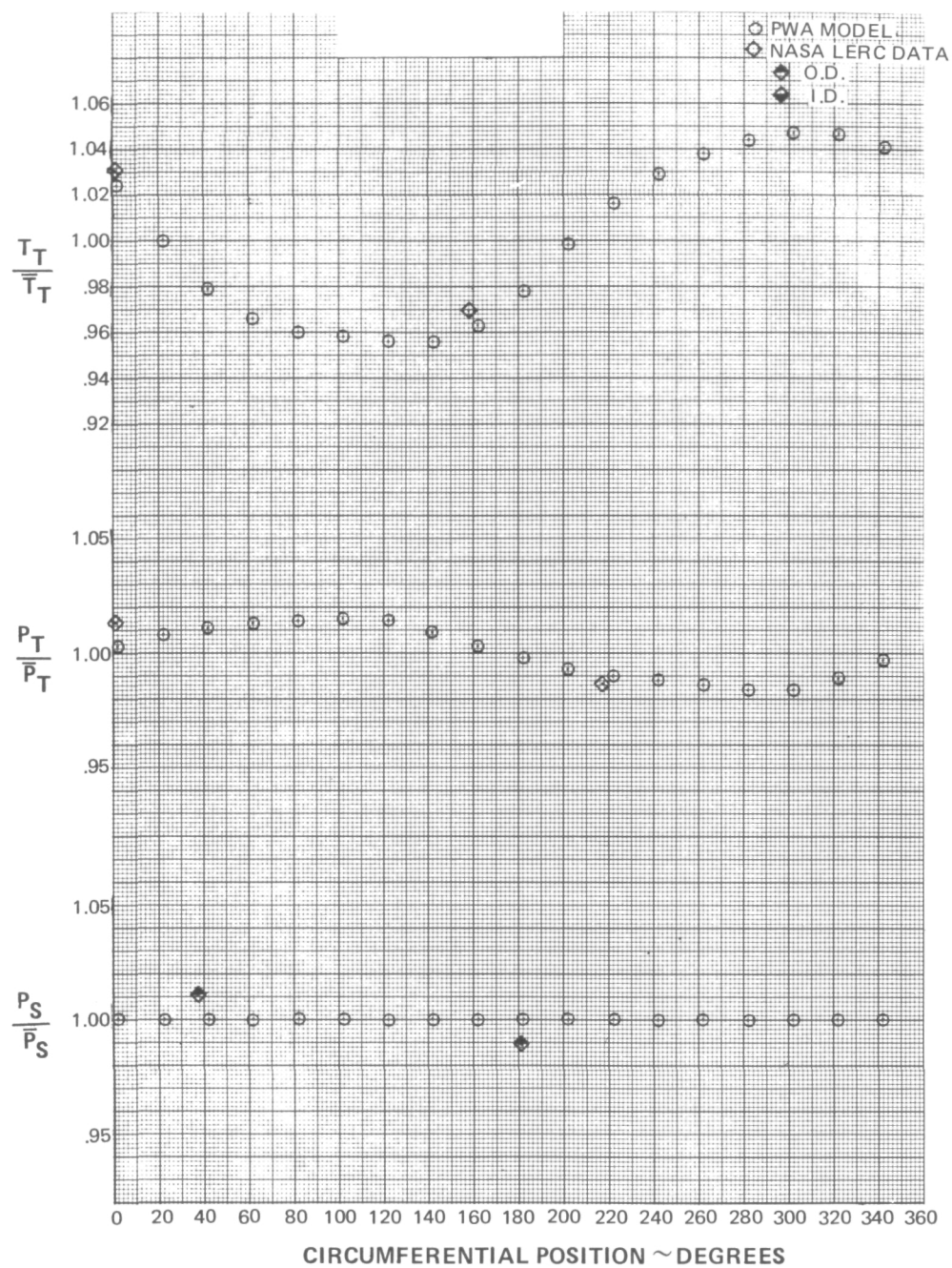


Figure 19g Total Temperature Distortion ($\Delta T/T = 0.11$) – Station 3.0

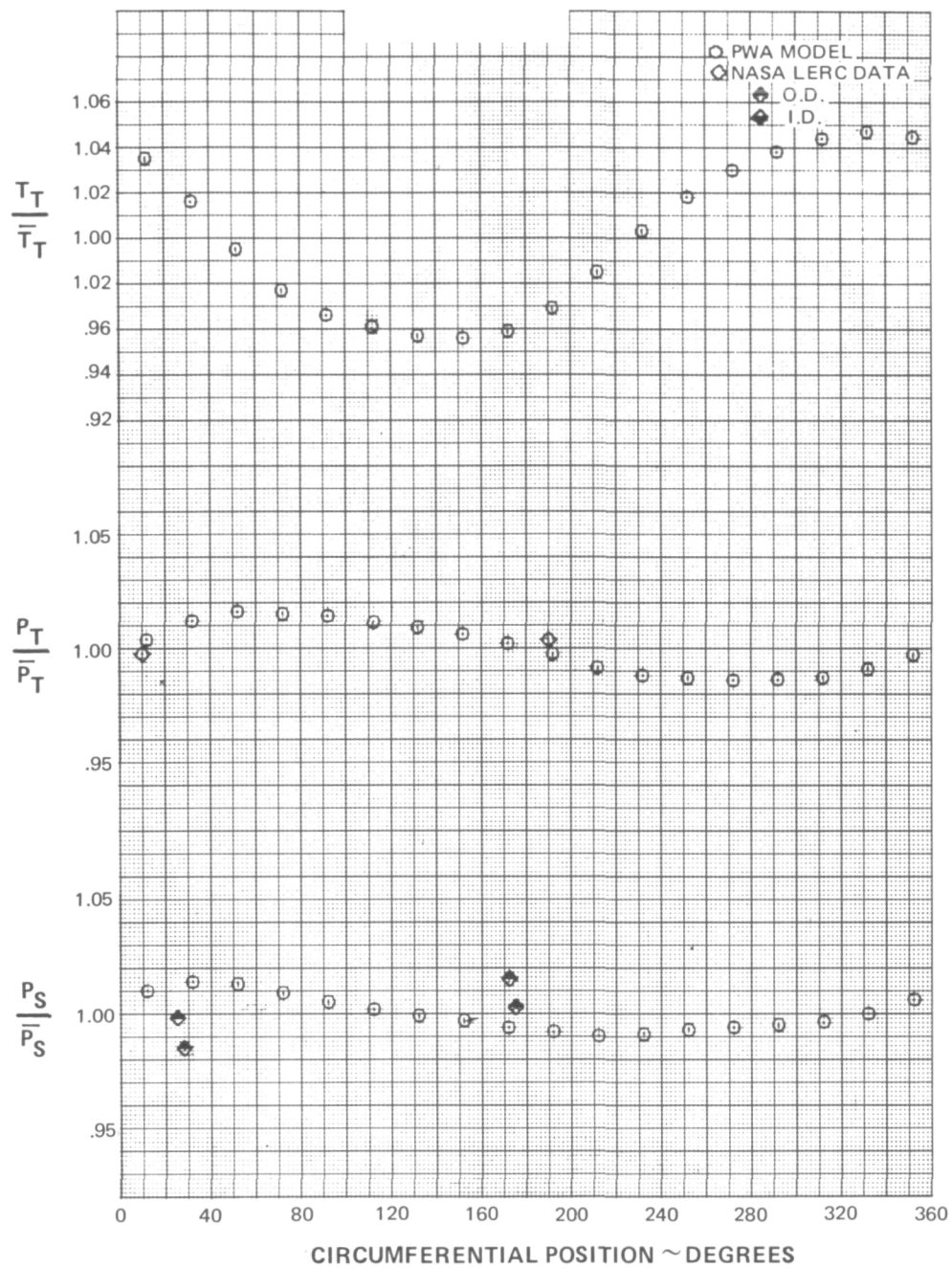


Figure 19h Total Temperature Distortion ($\Delta T/T = 0.11$) – Station 3.12

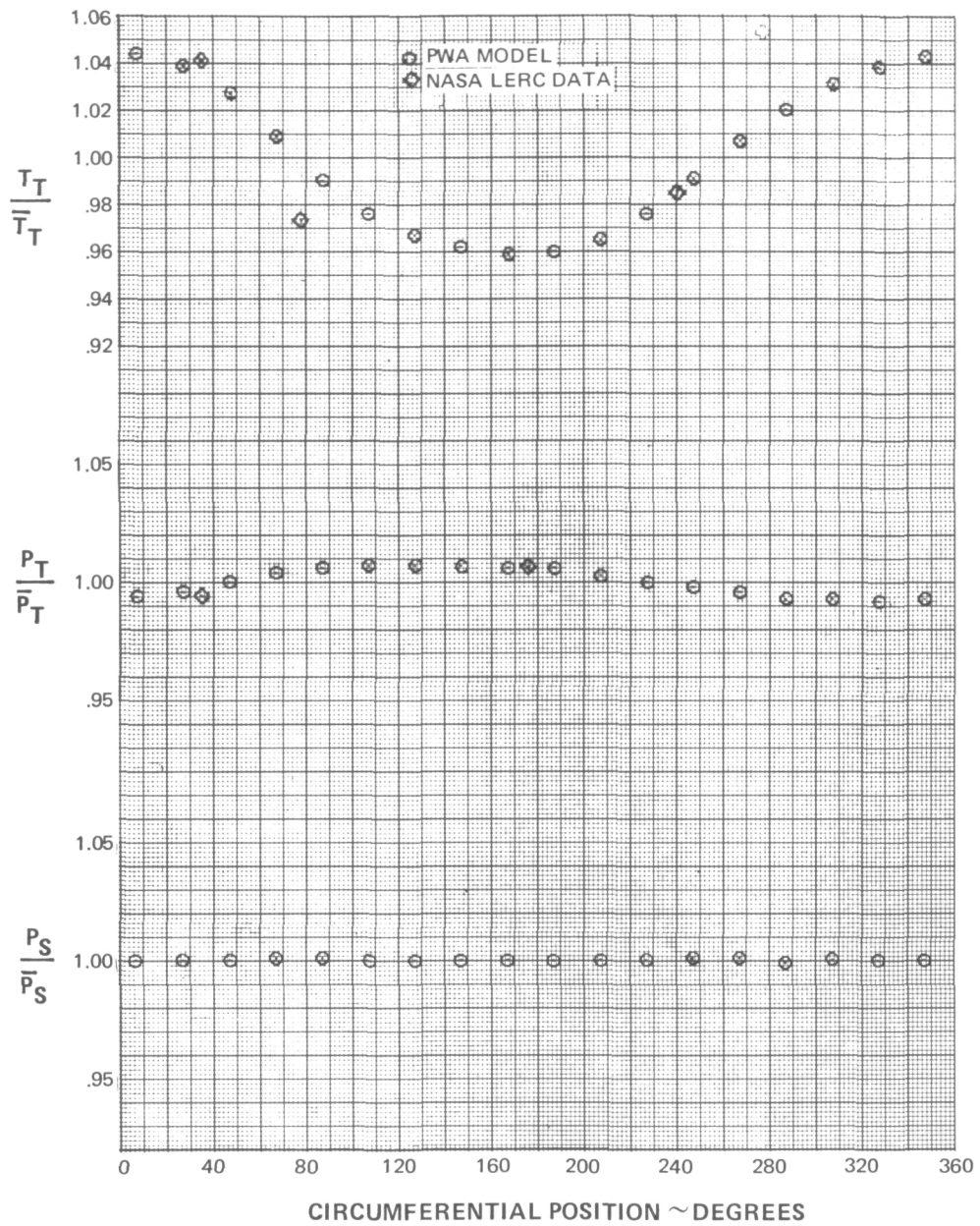


Figure 19i Total Temperature Distortion ($\Delta T/T = 0.11$) – Station 4.0

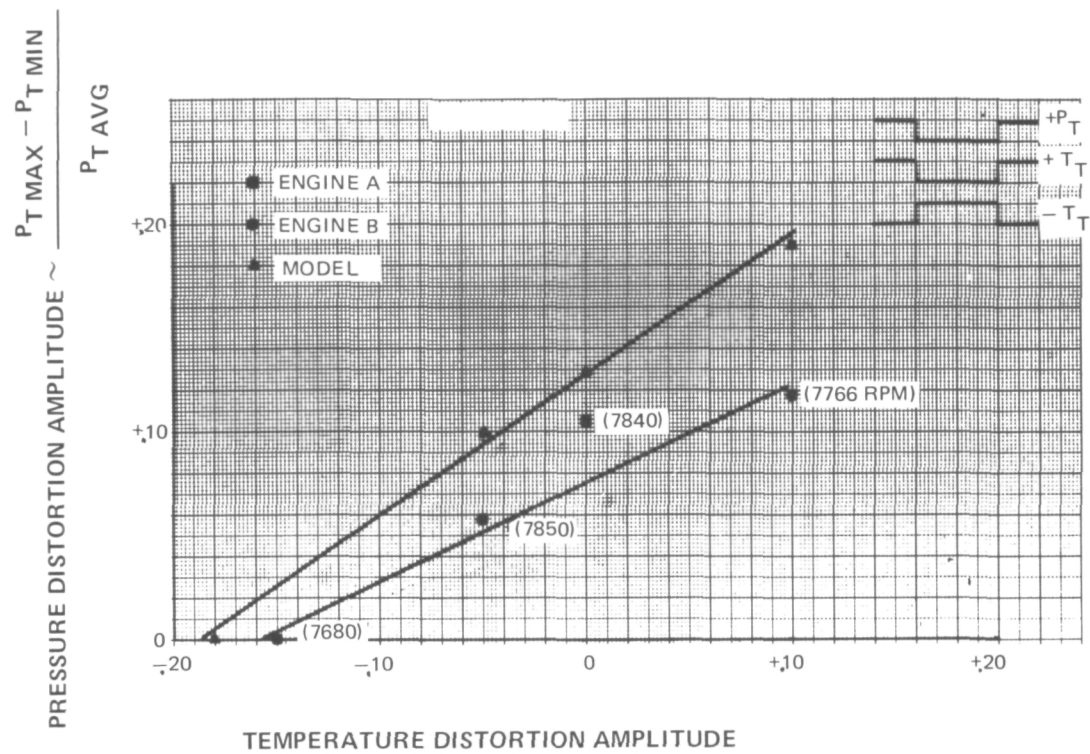


Figure 20 Comparison of Model Prediction and Data for Combinations of 180-degree Pressure and Temperature Distortion, RNI = 0.5 (No RNI Correction Applied to Temperature Distortion Level)

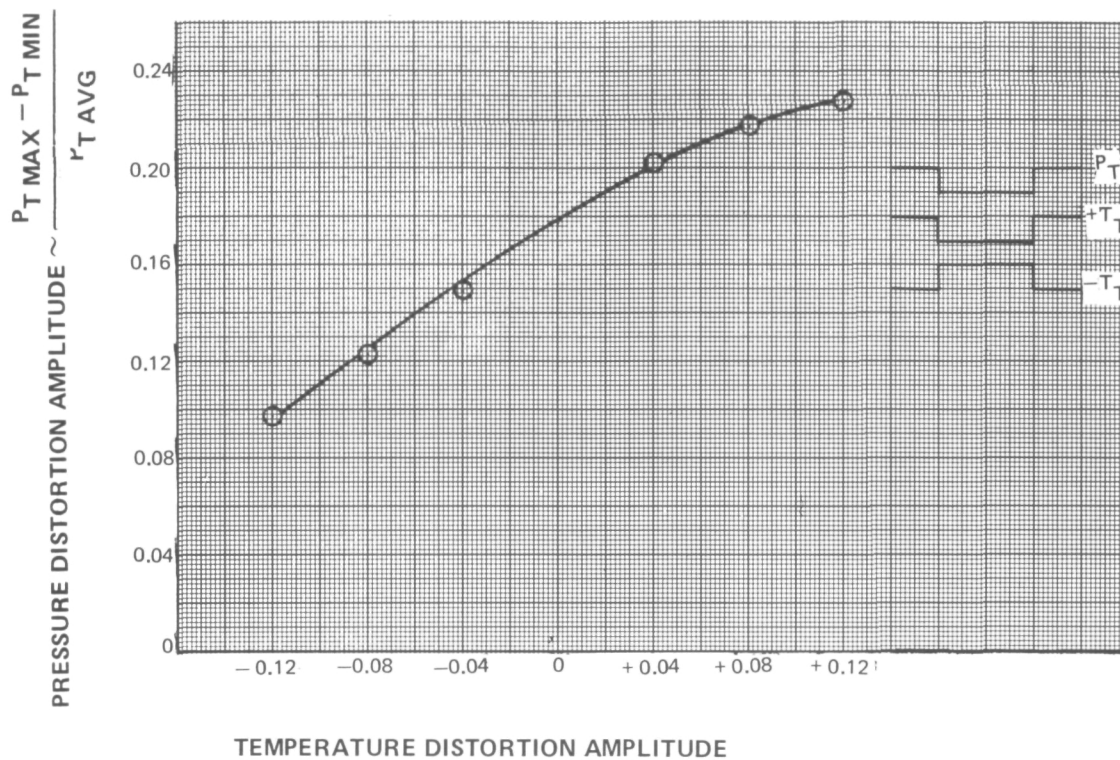


Figure 21 Predicted Distortion Sensitivity for Aligned and Opposed 180-degree Pressure and Temperature Distortion – 8600 RPM, RNI = 0.5 (No RNI Correction Applied to Temperature Distortion Level)

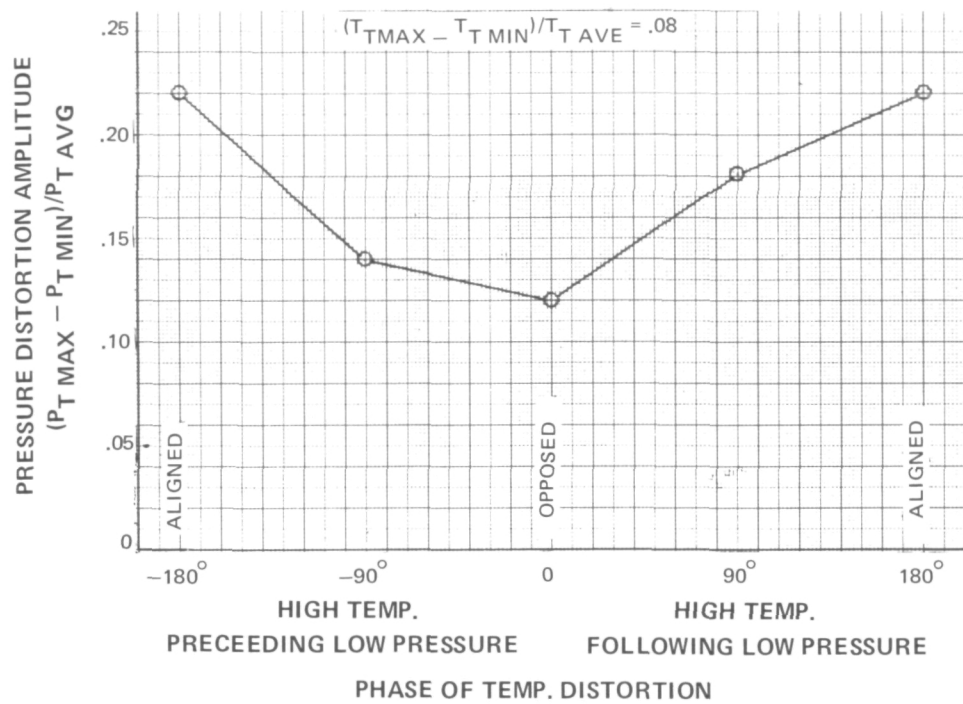


Figure 22 Predicted Influence of Distortion Orientation for 180-degree Pressure and Temperature Distortion – 8600 RPM, RNI = 0.5 (No RNI Correction Applied to Temperature Distortion Level)

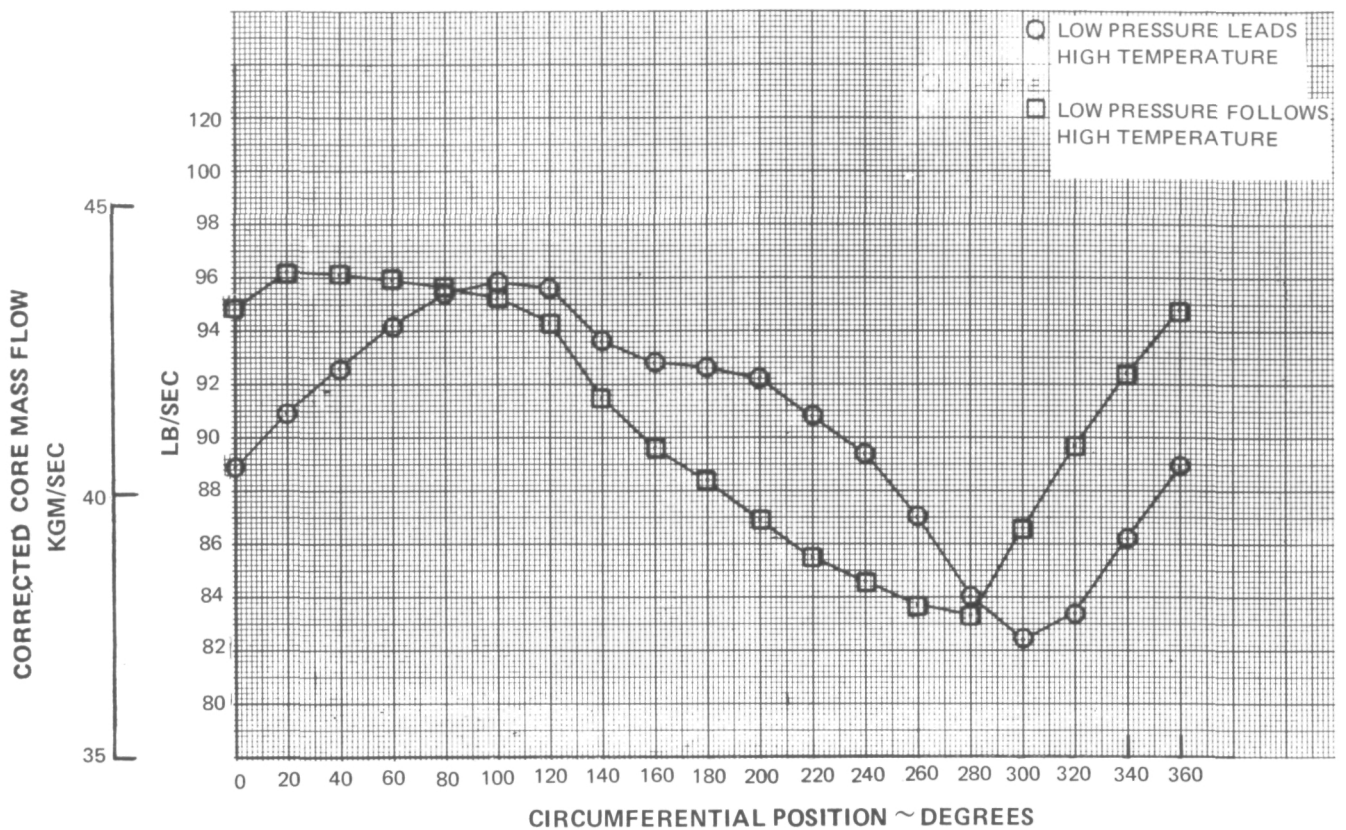


Figure 23 Predicted Inlet Corrected Airflow Distributions for 180-degree Pressure Distortion Leading and Following Temperature Distortion by 90 degrees - 8600 RPM, RNI = 1.0

APPENDIX A – PERFORMANCE MAPS

Performance maps of the TF30-P-3 compression system components are contained in Figures 1A through 9A of this appendix. Figures 1A through 3A present the average distorted operating conditions with 180° total pressure distortion. Figures 4A through 6A include the temperature and the combined pressure and temperature distortions. Figures 7A through 9A show the 120° pressure distortion cases. The operating lines shown on these maps correspond to nominal TF30-P-3 operation. The NASA LeRC was below the fan operating line and above the low pressure compressor operating line because the engine was tested with a choked exit nozzle.

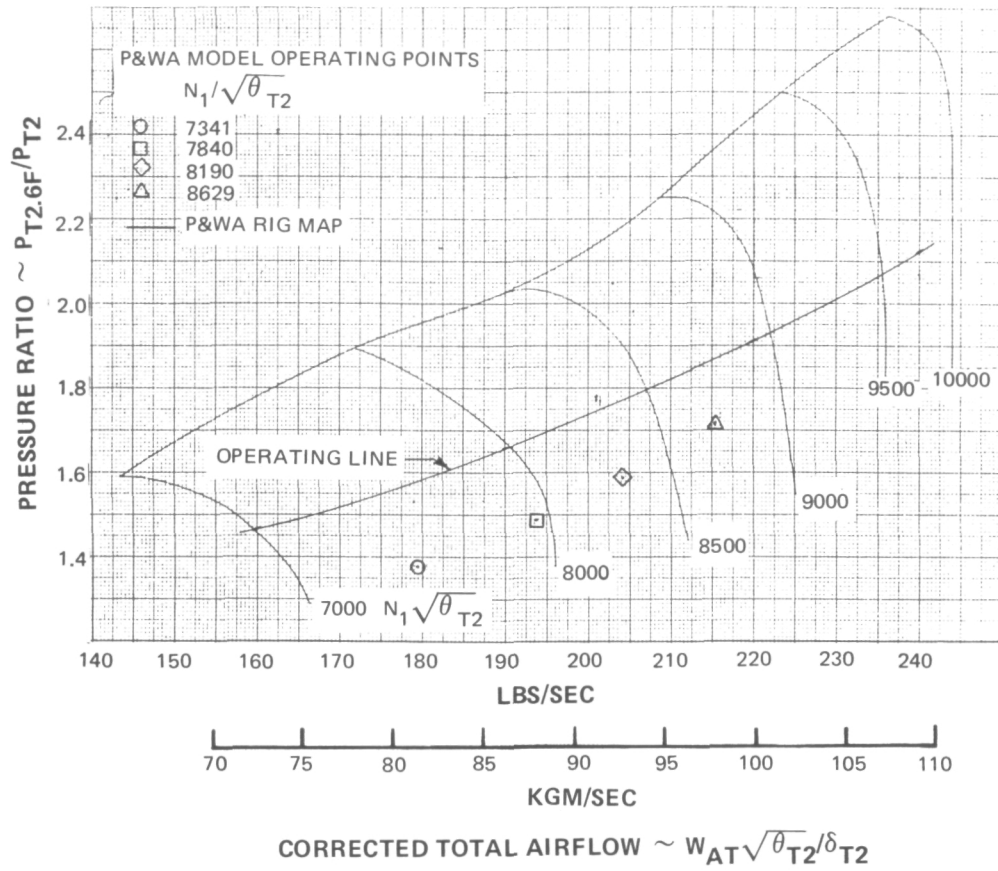


Figure A1 Fan Performance – 180-degree Pressure Distortion

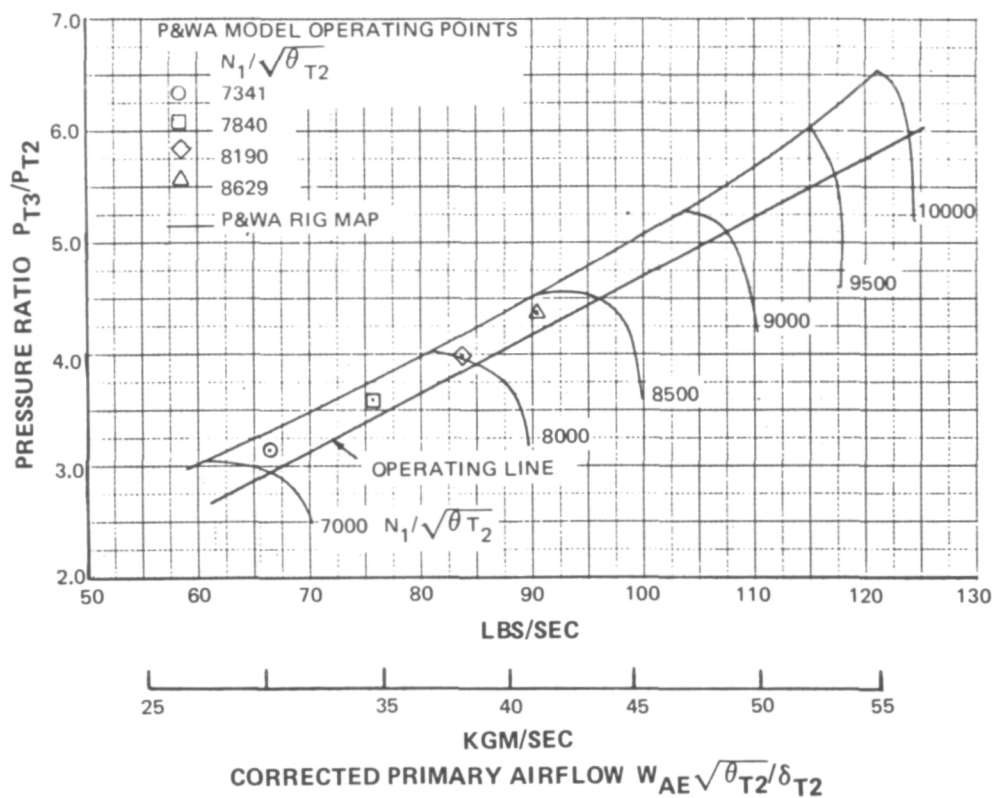


Figure A2 Low-Pressure Compressor Performance – 180-degree Pressure Distortion

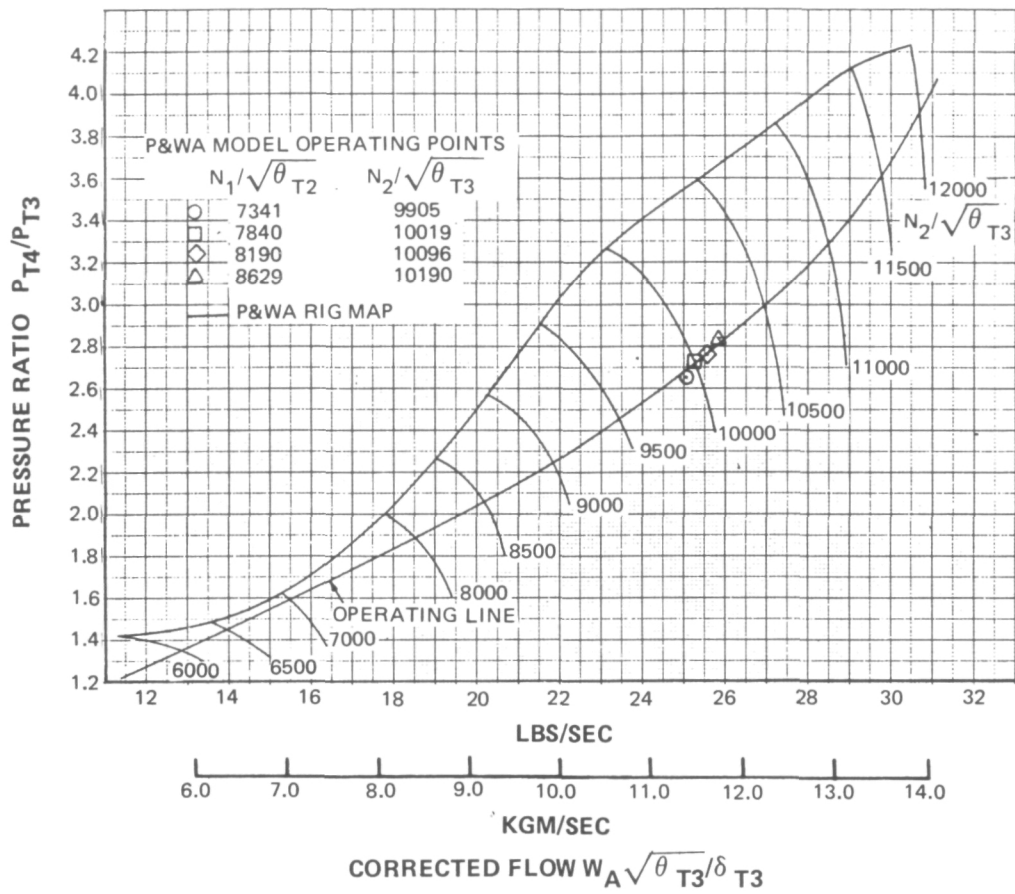


Figure A3 High-Pressure Compressor Performance – 180-degree Pressure Distortion

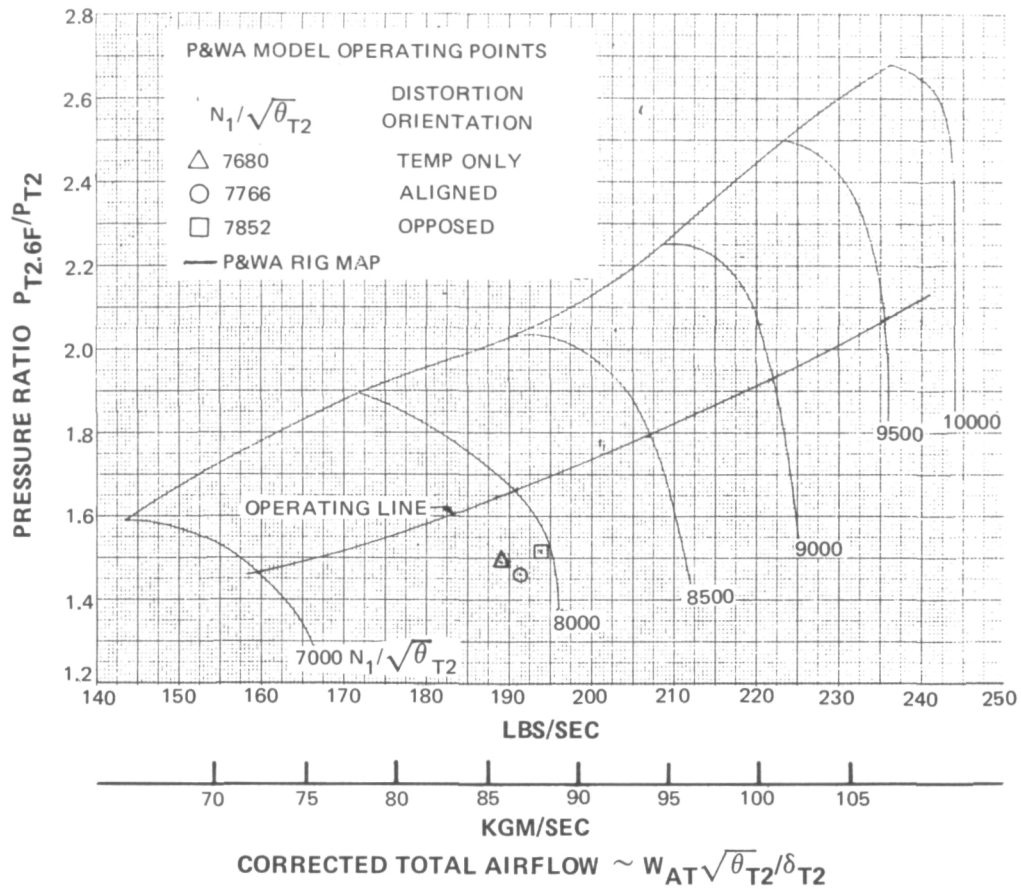


Figure A4 Fan Performance, Temperature and Combined Pressure and Temperature Distortion

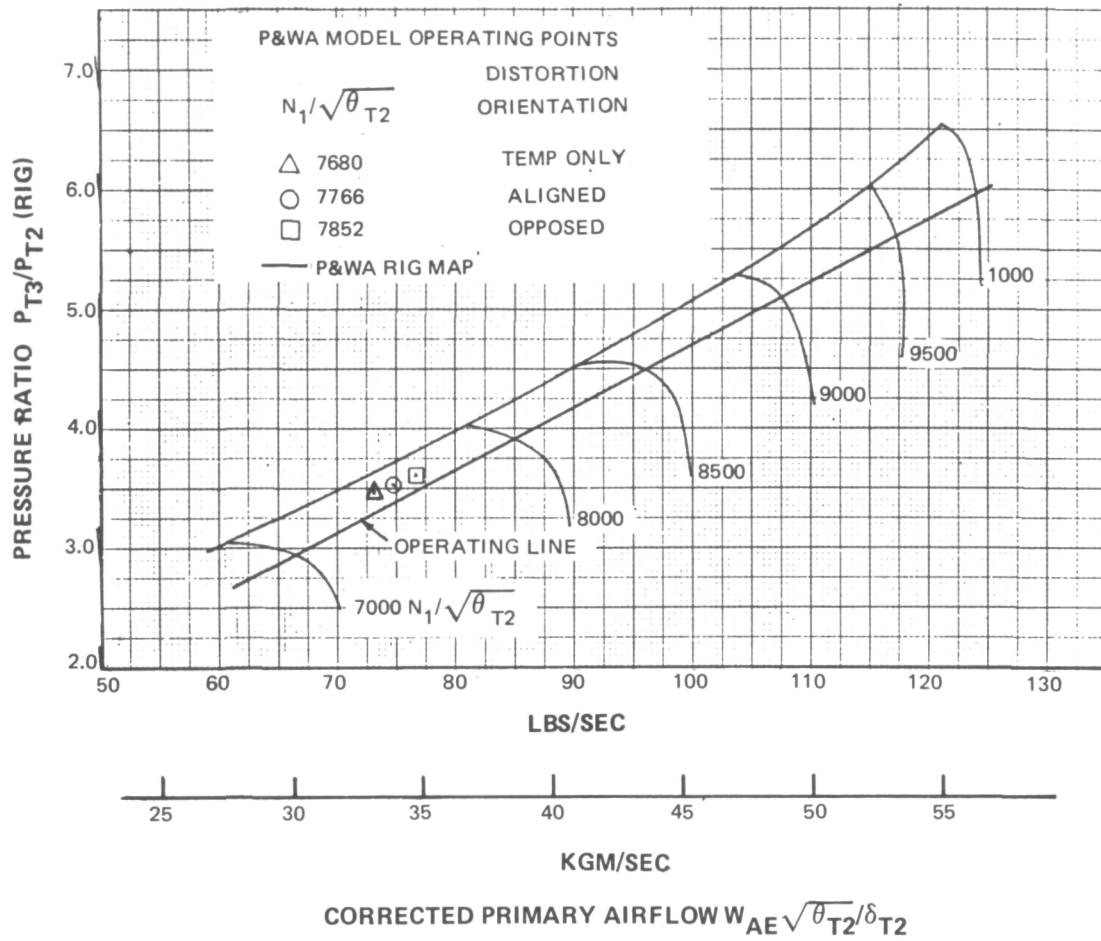


Figure A5 Low-Pressure Compressor Performance, Temperature and Combined Pressure and Temperature Distortion

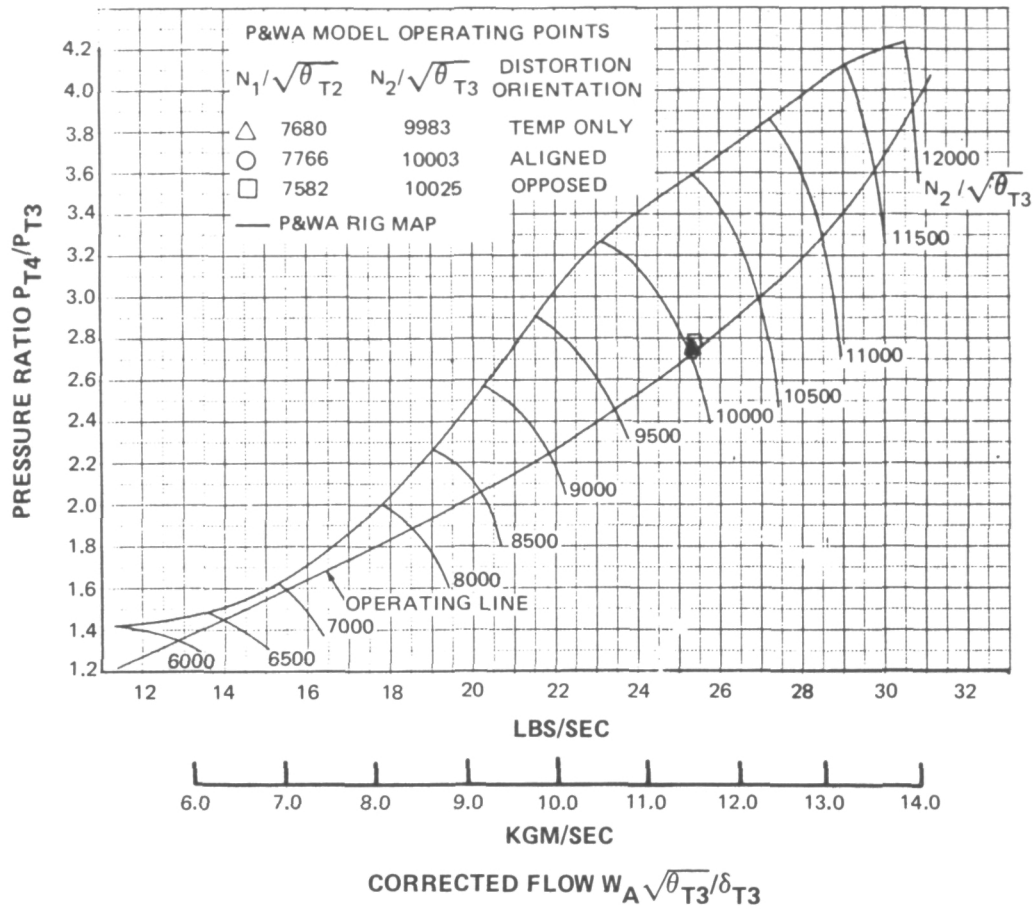


Figure A6 High-Pressure Compressor Performance, Temperature and Combined Pressure and Temperature Distortion

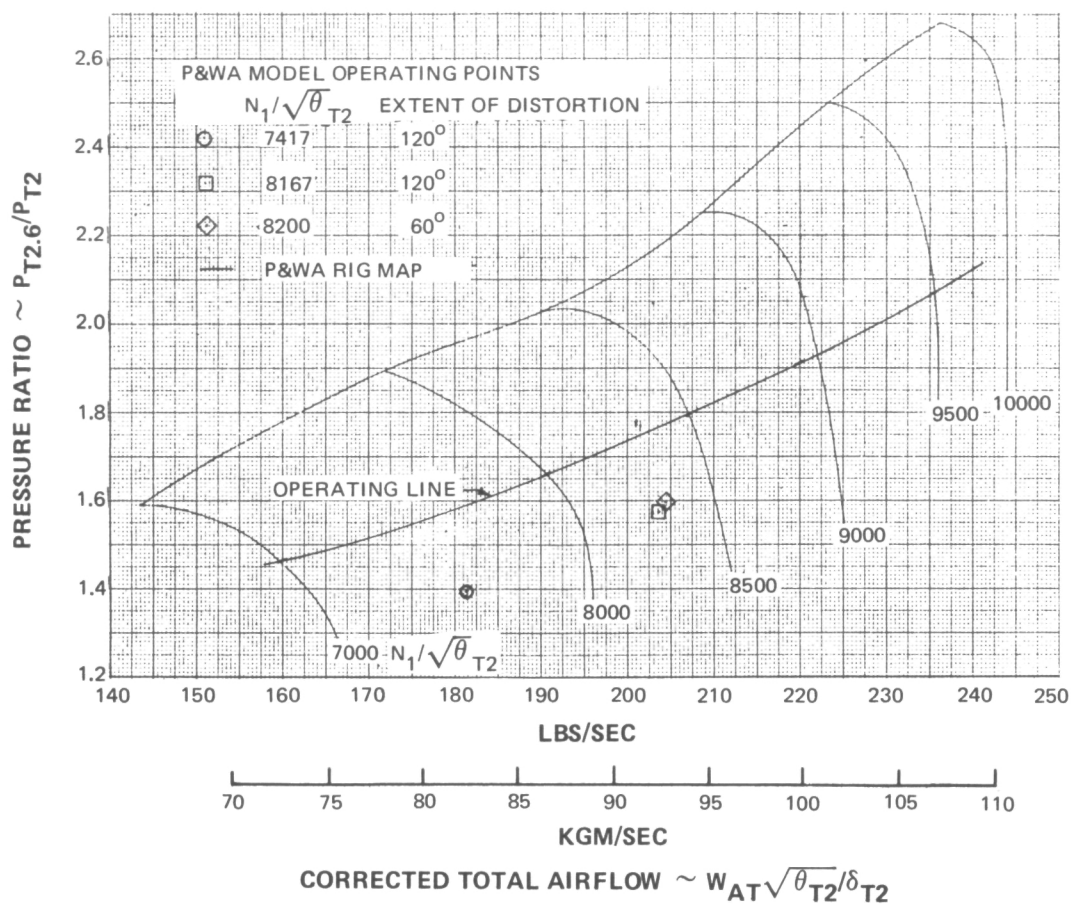


Figure A7 Fan Performance, 60-degree and 120-degree Pressure Distortion

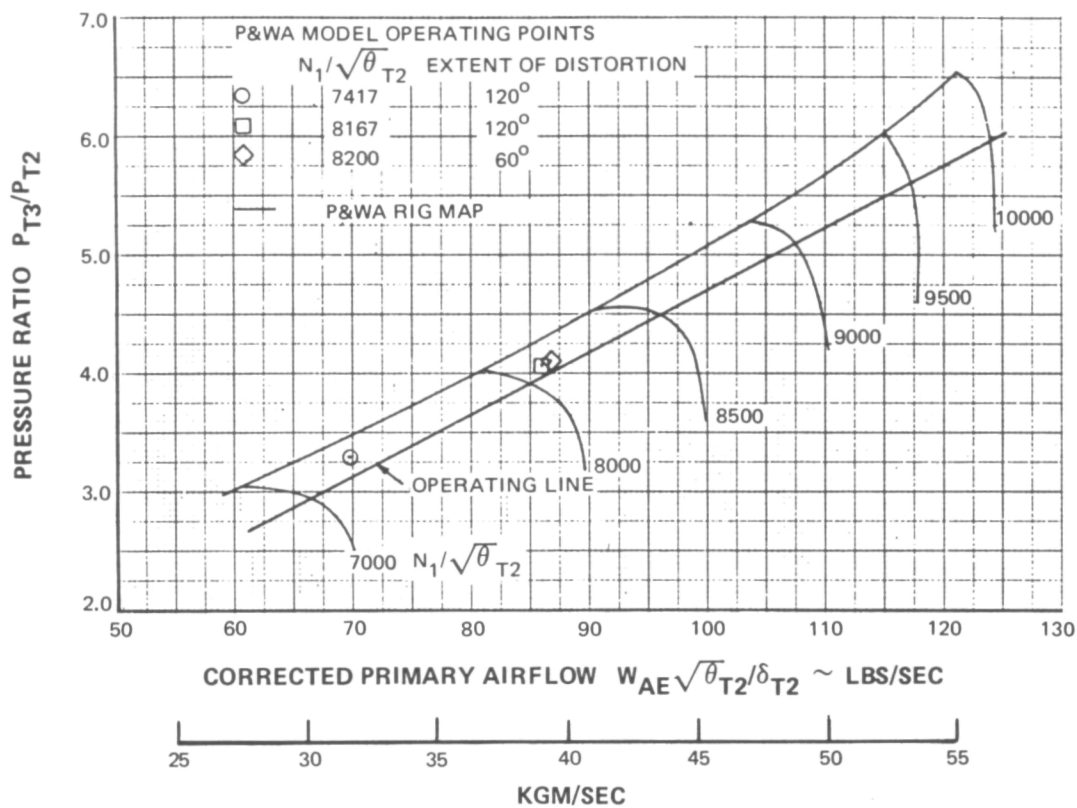


Figure A8 Low-Pressure Compressor Performance – 60-degree and 120-degree Pressure Distortion

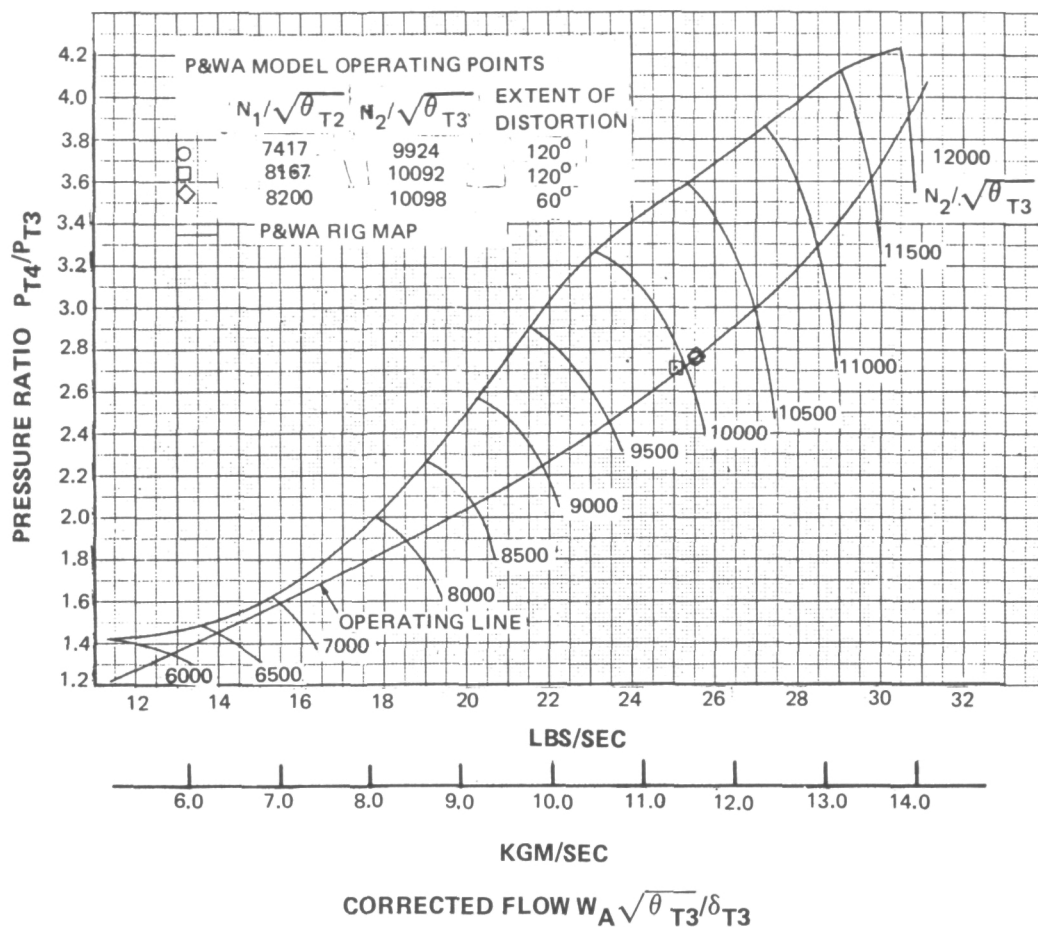


Figure A9 High-Pressure Compressor Performance – 60-degree and 120-degree Pressure Distortion

DISTRIBUTION LIST

PRATT & WHITNEY

Pratt & Whitney Aircraft
400 Main Street
East Hartford, CT 06108

Attn:

Mr. D. S. White
Mr. R. S. Mazzawy
Mr. G. A. Banks
Mr. A. W. Stubner
Mr. J. H. Tringali
Mr. A. A. Mikolajczak
Mr. D. L. Motycka
Mr. A. H. Pfeffer
Mr. J. A. Schuerman

Pratt & Whitney Aircraft
Florida Research & Development Center
P. O. Box 2691
West Palm Beach, FL 33402

Attn:

Mr. S. H. Ellis
Mr. D. J. Stewart (3)

Pratt & Whitney Aircraft
Division of United Aircraft
Attn: Mr. Joseph Chew
20800 Center Ridge Road
Rocky River, OH 44116

United Technologies Research Labs.
400 Main Street
East Hartford, CT 06108

Attn:

Mr. F. O. Carta
Mr. E. M. Greitzer
UTRC Library

Administrative Contracting Officer
Naval Plant Representative Office
Pratt & Whitney Aircraft
East Hartford, Connecticut 06108

GENERAL ELECTRIC

General Electric Company
Aircraft Engine Group
Cincinnati, OH 45215

Attn:

Mr. L. C. Right - E9
Mr. Vernon Reed - E9
Dr. L. H. Smith - H43
Mr. Paul H. Kutchenreuter, Jr. K69
Mr. J. Klapproth K96
Mr. T. Collins E198
Dr. W. Sleenken E198
Mr. W. A. Tesch - E198
Technical Information Center N32

General Electric Company
Attn: Mr. Mike Toth
5300 Riverside Drive
Cleveland, OH 44135

General Electric Company
Attn: Mr. Les King 240 G9
Mr. Tom Foy 240 G4
Mr. A. J. Chamay 240 G4
Technical Information Center
1000 Western Avenue
Lynn, MA 01910

General Electric Company
Attn: Dr. H. K. Lin
Corporate Research & Development
Box 43
Schenectady, NY 12301

DISTRIBUTION LIST (Cont'd)

NASA

National Aeronautics & Space Administration
Attn: RL/H. Johnson
Washington, DC 20546

Langley Research Center
Attn: Mr. W. P. Henderson
Propulsion Aero. Branch, MS: 189
Hampton, VA 23665

Ames Research Center
Attn: Mr. Daniel Benze
MS: 227-8
Moffett Field, CA 94035

Flight Research Center
Attn: Mr. William Schweikhard
P. O. Box 273
Edwards, CA 93523

Lewis Research Center
21000 Brookpark Road
Cleveland, OH 44135

Attn:	copies
Mr. Ross Willoh MS: 60-6~	(1)
Mr. Pete Batterton MS: 60-6	(3)
Mr. Bill Braitwaite MS: 60-6	(3)
Mr. Ed Graber MS: 60-6	(3)
Mr. Dave Evans MS: 60-4	(1)
Dr. Tony Kurkov MS: 60-4	(3)
Mr. Dave Bowditch MS: 86-1	(2)
Mr. Dan Drain MS: 100-1	(2)
Mr. Mel Hartmann MS: 5-9	(2)
Mr. N. Musial MS: 500-113	(1)
Mr. Leonard Schopen MS: 500-206	(1)
Dr. John Adamczyk MS: 5-9	(1)
Report Control Office MS: 5-5	(1)
Library MS: 60-3	(2)
Mr. Lawrence Ludwig MS: 23-2	(1)
Mr. Warner Stewart MS: 3-5	(1)
Mr. Roy Hager, MS: 5-9	(1)

NASA Scientific & Technical Information Facility
Attn: Acquisition Branch
P. O. Box 33
College Park, MD 20740

(10 + all remaining copies, and 6 copies of the Document
Release Authorization Form FF427)

DISTRIBUTION LIST (Cont'd)

MILITARY

Wright-Patterson Air Force Base
Wright-Patterson AFB, OH 45433

Attn:

AFAPL/TBC Mr. Marvin Schmidt
AFAPL/TBC Mr. Marvin Stibich
AFAPL/TBA Mr. J. E. Lueke
AFAPL/TB Mr. Ivan Bush (4 copies)
AFAPL/CCN Dr. Hans J. P. Von Ohain
AFAPL/DOZ Dr. Francis Ostidiek
AFAPL/TBC Mr. Len Obery LeRC
AFFDL/FXM Mr. Dennis Sedlock
AFFDL/FXM Mr. Keith Richey
AFASD/ENFPA Major D. H. Quick

ARO, Inc.

Arnold Air Force Station, TN 37389

Attn:

Mr. Bill Kimsey (2 copies)
AEDC/ARO/ETF
Mr. John Martin &
Mr. Larry Galiger
AEDC/ARO/PWT

Arnold Engineering Development Center

Attn: Dr. Heiser, Chief Scientist
Arnold Air Force Station, TN 37389

ARO, Inc.

Engine Test Facility
Attn: Mr. Jack Tate
Arnold Air Force Station, TN 37389

ARO, Inc.

Arnold Engineering Development Center
Attn: Mr. J. L. Jackocks
Arnold Air Force Station, TN 37389

Naval Postgraduate School
Department of Aeronautics
Attn: Professor Paul Pucci
Monterey, CA 93940

Naval Air Propulsion Test Center
Trenton, NJ 08628

Attn:

Mr. J. F. Boytos PE-52
Mr. Donald Brunda
Mr. Vernon Labosky

Naval Air Systems Command
Attn: Mr. Dan Alexander
AIR53631E
Washington, DC 20360

Naval Air Development Center
Attn: Mr. Thomas J. Brennan
Head, Propulsion Branch
Warminster, PA 18966

INDUSTRY

Northrop Corporation
Aircraft Division
Attn: Mr. R. D. Sutton
3901 West Broadway
Hawthorne, CA 90250

Lockheed-California Co.
Attn: Mr. T. A. Sedgwick
Dept. 74-14, Bldg. 63G
Plant A-1
P. O. Box 551
Burbank, CA 91053

LTV Aerospace Corporation
Attn: Mr. William E. Simpkin
Vought Systems Division
P. O. Box 5907
Dallas, TX 75222

Attn:
Mr. H. C. Melick, Jr.
Aerodynamics Specialist

Grumman Aerospace Corporation
Attn: Mr. Clifford A. Hoelzer
Head, Airbreathing Propulsion
Plant 5
Bethpage, NJ 11714

AVCO Lycoming Division
Attn: Library
550 S. Main Street
Stratford, CT 06497

DISTRIBUTION LIST (Cont'd)

INDUSTRY

Rolls-Royce (1971) Ltd.
Bristol Engine Division
Attn: Mr. Darrell Williams
Installed Aerodynamics Dept.
Box 3, BS127QE
Filton, Bristol, England

Teledyne
Attn: Library
1330 Laskay Road
Toledo, OH 43967

AiResearch Manufacturing Company
of Arizona
402 South 36th Street
Phoenix, AZ 85034

Attn:
Dr. William F. Waterman
Supervisor, Aerodynamics
Dept. 93-350M

Mr. G. A. Burnett
Department 93-353M

Library

Advanced Technology Laboratories, Inc.
Attn: Dr. John Erdos
Merrick & Stewart Avenues
Westbury, NY 11590

The Boeing Company
Attn: Mr. G. Lampard
Mail Stop 8C-27
P. O. Box 3999
Seattle, WA 98124

McDonnell-Douglas Corporation
Attn: Mr. A. P. Farr, III
Bldg. 33, Level 15 North
P. O. Box 516
St. Louis, MO 63166

Attn:
Mr. Hershel Samis
Br. Mgr. Propulsion

Douglas Aircraft
Attn: Mr. Ron Kwai
Mail Code 36-41
3855 Lakewood Blvd.
Long Beach, CA 90846

General Dynamics Corporation
Attn: Mr. P. P. Truax
Convair Aerospace Division
P. O. Box 748, M/Z 2892
Fort Worth, TX 76101

Attn:
Mr. Robert A. Stevens
Mr. L. H. Schreiber

Rockwell International
International Airport
Los Angeles, CA 90009

Attn:
Mr. C. J. MacMiller
B-1 Division, Mail Code AB 70

Mr. Robert H. Johnson
Mail Code AB 71

Rockwell International
Columbus Aircraft Division
Attn: Library
4300 East 5th Avenue
Columbus, OH 43216

Garrett AiResearch Manufacturing Co.
Attn: Library
2525 West 190 Street
Torrance, CA 90509

General Motors Corporation
Detroit-Diesel, Allison Division
P. O. Box 894
Indianapolis, IN 46206

Attn:
Mr. Samy Baghdati

Library

Mr. J. A. Korn
Mail Stop U28

DISTRIBUTION LIST (Cont'd)

SCHOOLS

Massachusetts Institute of Technology
Gas Turbine Laboratory
Attn: Mr. Jack L. Kerrebrock
Cambridge, MA 02139

Virginia Polytechnic Inst. & State University
Attn: Mr. W. F. O'Brien, Jr.
Mechanical Eng. Department
Blacksburg, VA 24061

Penn State
Attn: Dr. Robert Henderson
Associate Prof. of Engr. Research
Ordinance Research Laboratory
P. O. Box 30
State College, PA 16801

The Ohio State University
Attn: Prof. John D. Lee
Dept. of Aeronautical & Astronautical Engr.,
Neil Avenue
Columbus, OH 43210

Iowa State University
Attn: Dr. George Serovy
Department of Mechanical Engineering
Ames, IA 50010

Purdue University
Attn: Prof. Mel R. L'Ecuier
School of Mechanical Engineering
Jet Propulsion Center
Lafayette, IN 47097

Attn:
Prof. S. N. B. Murthy

Pennsylvania State University
Department of Aerospace Engineering
Attn: Dr. N. Litaram
233 Hammond Bldg.
University Park, PA 16802

Daniel and Florence Guggenheim
Jet Propulsion Center
California Institute of Technology
Attn: Prof. W. D. Rannie
Pasadena, CA 91109